



8. The SPACE Analysis

A little learning is a dangerous thing; Drink deep, or taste not the Pierian Spring
~ Alexander Pope

The first chapters in this work served as an introduction to the theoretical physics models that were necessary to explain the signature of the particles under investigation and gave more details on the background contributions. Later chapters were used to explain the general workings of the detector and describe several reconstruction and analysis techniques. In this chapter, we focus on how the analysis was set up and present the results and conclusions that can be drawn. Starting from data that was processed with basic reconstructions and passing general requirements, a workflow was set up to try to discriminate events that are most likely of known physical interactions from the rare events that are sought for in this analysis: hypothetical particles with an anomalous charge (introduced in Chapter 2).

These particles are assumed to have a long lifetime and an isotropic flux close to the detector. Due to their low charge, they will produce less Cherenkov radiation compared to muons when traveling through ice, resulting in dim tracks in the IceCube detector. The most significant background contributions are from muons that originate either from air showers or ν_μ . Most of the events that pass the trigger selections in the detector originate from downgoing muons that were produced in air showers. Therefore, it was chosen to focus on upgoing tracks, which reduces the air shower background with many orders of magnitude. Even though the tracks that are reconstructed as downgoing are removed, most of the tracks that are reconstructed as upgoing still originate from mis-reconstructed downgoing muons from air shower. Only a small fraction of these muons is mis-reconstructed, but is still the largest background due to the enormous amount of air shower events. The other most prominent background consists of muons from atmospheric ν_μ that are capable of traversing Earth and produce upgoing muon tracks. Because the detector consists of sparsely distributed optical modules in the ice, these tracks can appear dim and resemble the signature of particles with a low charge. Additionally, due to the low number of DOMs that will be hit in such a dim event, noise hits have to be accounted for. Therefore, multiple variables in the analysis require a minimal amount of hits and events with a very low number of hits are removed. Also, these events often lead to data-MC disagreement due to the large noise contribution and a lack of information that is necessary in reconstruction algorithms.

The analysis consists of a number of quality cuts (where events that cannot be distinguished

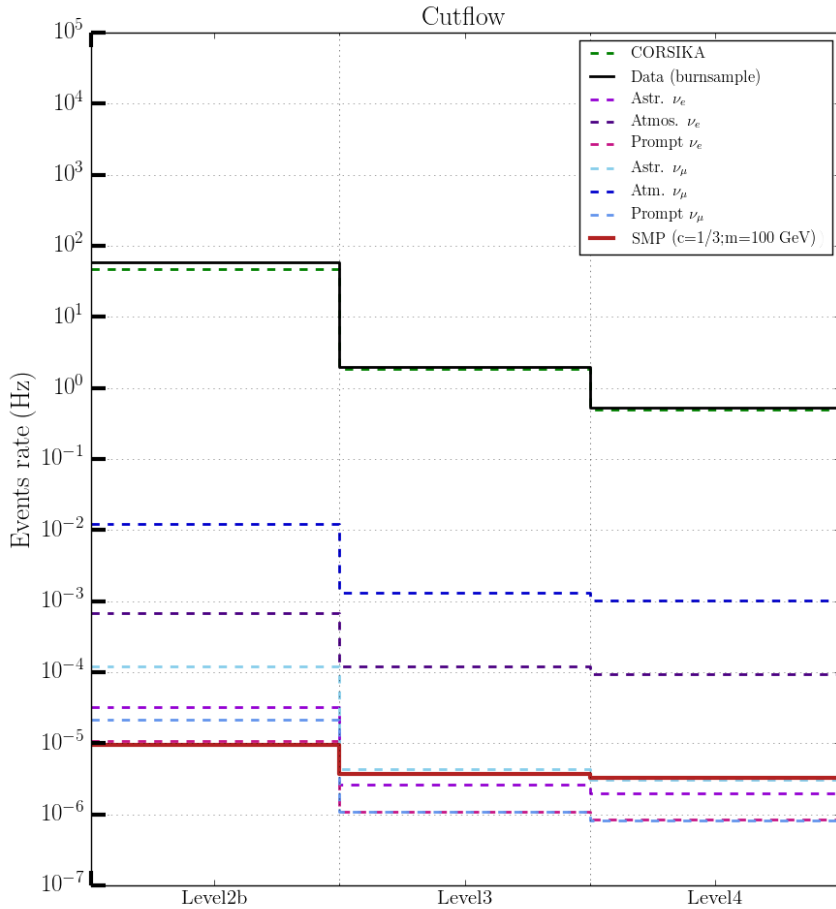


Figure 8.1: Event rate at three steps in the analysis. Data from the burn sample is shown in black, several Monte Carlo background samples are shown with dashed lines and the solid red line corresponds to one signal sample of an SMP with charge 1/3 and mass 100 GeV. “CORSIKA” corresponds to events from air shower simulations.

between signal and background are removed), variable constructions and some additional analysis techniques. The workflow of this analysis is described step-by-step in the contents of this chapter. The analysis is subdivided into several “Levels”. Figure 8.1 shows the rate of several Monte Carlo backgrounds, the burn sample, and a signal sample in function of Levels 2b, Level 3 and Level 4.

The analysis was named the “SPACE” analysis, which stands for a “Search for Particle with Anomalous ChargE”.

8.1 Filter selection

As explained in Section 5.4.2, IceCube data is processed through multiple filters. Since this analysis is the first of its kind in the collaboration, the choice was to start from scratch and not use a processed dataset from another analysis*. Therefore, a combination of filters was chosen that is able to distinguish signal events from background as best as possible at this preliminary stage. An illustration of filter combination efficiency is given in Figure 8.2. The efficiency is defined as the percentage of simulated particles that pass a certain filter. The figure shows many

*Since many searches look for similar signatures or deal with similar backgrounds, processed data sets in the collaboration are often used for multiple analyses.

possible filter combinations and are ranked in function signal efficiency. The efficiency of the filter combination should be as high as possible for the signal, and as low as possible for background events. Therefore, the combination of four filters was chosen. This filter selection will be referred to as *Level 2b* as an addition to filter processing in Level 2 (see Section 6.5). The filters that were included in this stage are the VEF, LowUp, Online Muon L2, and DeepCore filters. They are explained in more detail below.

8.1.1 VEF

The Vertical Event Filter (VEF) is originally designed for oscillation and Earth WIMP analyses and makes use of the string trigger (see Section 5.4.1). An SMP that travels in a direction following a string, or close by, can trigger optical modules even though the total light yield of an event is low (other trigger hits are unlikely in this scenario), making this filter an ideal part of the filters that are selected. The filter ignores HLC hits in the top 5 DOM layers to reduce the muonic component from air shower events and other selection cuts try to further refine the search region, in particular for WIMP events (see Section 5.8.2). For example, the LineFit zenith angle should be higher than 166.2° , focussing on upgoing tracks. More information can be found in Ref. [221].

8.1.2 LowUp

The primary motive for the LowUp filter design is again focussed on WIMP searches, but is also used in atmospheric neutrino analyses. It is set up to capture upgoing muons with an energy below 1 TeV. The majority of the events that are selected by this filter make use of the in-ice Volume Trigger, but also the in-ice SMT8, in-ice String and SMT3-DeepCore triggers are used for completeness (see Table 5.1). The selection cuts are loose selections required to look for upgoing track-like particles. For example, the zenith angle of the reconstructed particle should be 80° or higher and the difference between the maximal z -coordinate and minimal z -coordinate of hit DOMs should be less than or equal to 600 m. More information can be found in Ref. [222].

8.1.3 Online Muon L2

The Online Muon L2 filter is a subset of the Muon Filter (see Ref. [223]) and tries to select the most interesting muon-like events while reducing the rate of the filter from around 30 Hz to 5 Hz, reducing the data stream by a factor of 6. Historically, this subset was data processed offline from the Muon Filter, but after realizing that this could be done online and because many analyses made use of this selection, it was chosen to implement it as a separate filter. The filter tries to select both upgoing and downgoing muons, with different selection cuts depending on the zenith angle of the particle reconstruction. The four selection ranges are defined as:

- $180^\circ \geq \theta_{\text{MPE}} \geq 115^\circ$ (upgoing)
- $115^\circ > \theta_{\text{MPE}} \geq 82^\circ$ (upgoing)
- $82^\circ > \theta_{\text{MPE}} \geq 66^\circ$ (downgoing)
- $66^\circ > \theta_{\text{MPE}} \geq 0^\circ$ (downgoing)

where the particle reconstruction was done with MPE (Section 7.1.3), which was feasible if it only had to be done on the events passing the Muon Filter. The first two regions have an efficiency* higher than 99%. The downgoing region requires additional cuts to remove the less interesting muons from air showers. The main variables used are the number of hit DOMs, likelihood parameters, number of PEs, etc. More information can be found in Ref. [224].

8.1.4 DeepCore

A DeepCore specialized filter was added to account for SMP tracks that traverse the more densely instrumented DC detector. Due to the low amount of light produced by these dim tracks, adding the DeepCore filter (which is optimized for the DC instrumented volume) proved to be of significant importance.

*Here defined as having a reconstruction within 3° of the MC truth.

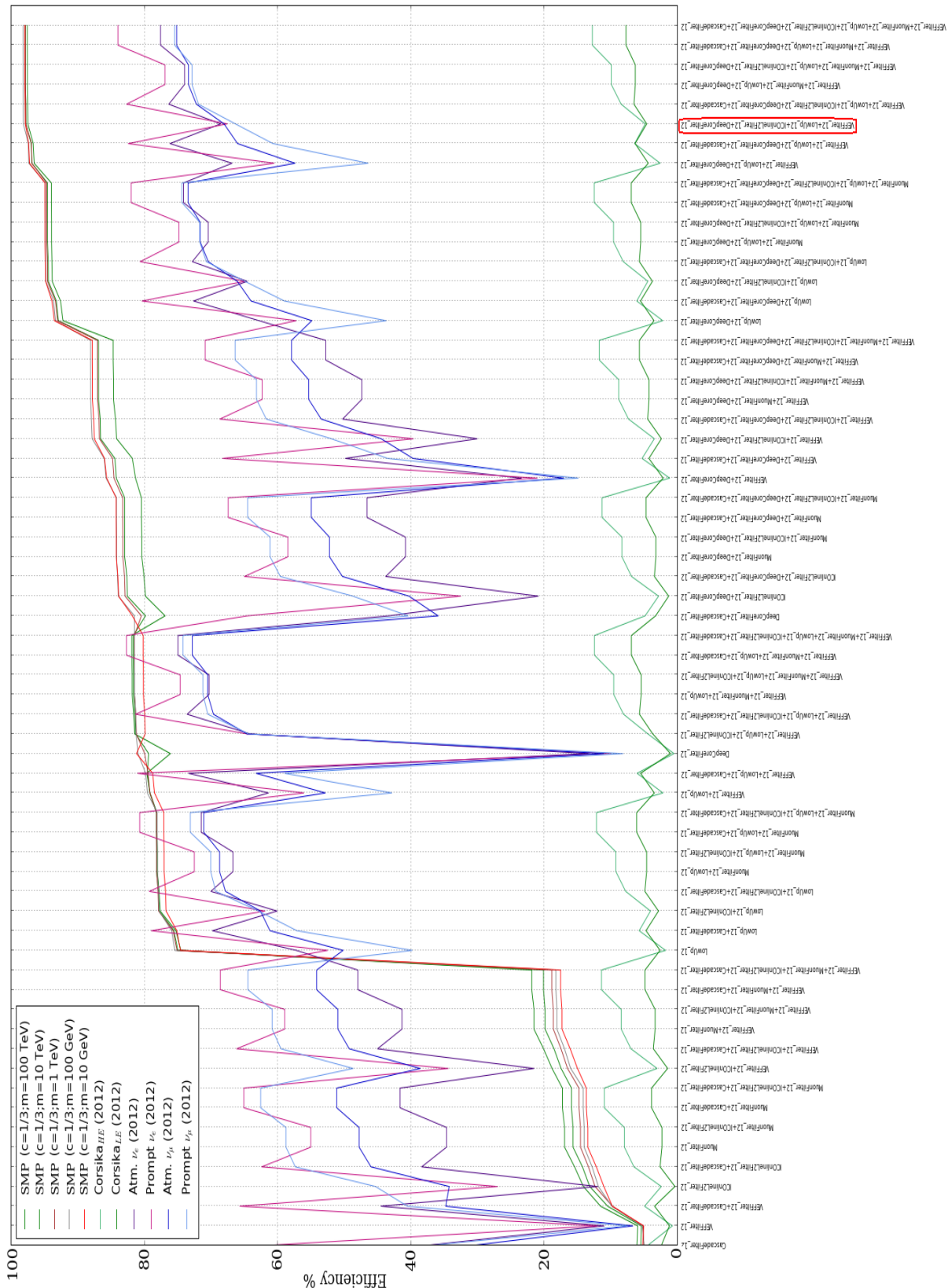


Figure 8.2: Illustration of the efficiencies of several filters and their possible combinations. The x-axis was determined by starting with filter selections that had a low efficiency in signal selection and ranges from low to high signal performance. Five signal points for a fixed charge and different mass show similar results. SMPs with charges 1/2 and 2/3 show similar results but are left out for a better visualization. An upgoing signal sample was used to determine the signal efficiency. The chosen filter combination is shown in red.

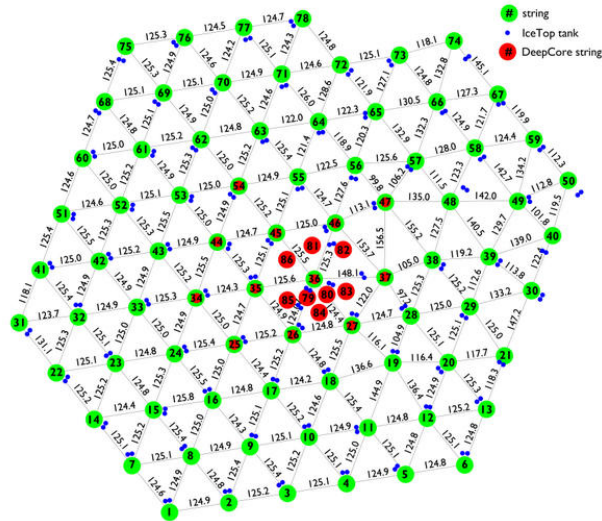


Figure 8.3: Top view of the IceCube strings (and IceTop tanks) where the DeepCore fiducial volume is defined by the DeepCore strings (red) and several surrounding in-ice IceCube strings (green and red).

The DeepCore filter was designed to look for very dim events coming from dark matter, low-energy neutrino oscillations, and for studies that are dedicated to observe atmospheric neutrinos below 100 GeV. The fiducial volume used for this filter consists of

- the bottom 22 DOMs on the IceCube strings 25, 26, 27, 34, 35, 36, 37, 44, 45, 46, 47 and 54;
- the bottom 50 DOMs on the DeepCore strings 79-86.

These strings are indicated in Figure 8.3.

The filter uses the DeepCore SMT3 trigger and additionally, two layers are used as a veto to remove events that probably originate from atmospheric muons. This is done by comparing the position and timing of all hits to the position and timing of several COGs that are constructed from these hits (see footnote pg. 112 for the explanation of a COG). More information can be found in Ref. [225].

8.1.5 Burn sample checks

Before further processing, the burn sample (a subset of the data that is used to check if the Monte Carlo adequately describes the data) is compared over the different years that are used in the analysis. This is shown in Figure 8.4. The sine wave pattern from seasonal variations in the atmosphere (see Section 6.2.1.1) is clearly visible and consistent over the years. The x -axis is more spread out in the first years due to the larger amount of test runs. The shift in data rate in early 2011 runs is caused by a DOM software change that was introduced in the Summer of 2011 [226]. This phenomenon is well understood and since the changes are minimal, these runs are kept. More information on the burn sample can be found in Section 6.6.

8.2 Level 3

The combined filter selection leads to a total rate of ~ 60 Hz, or an expected 1.9 billion events per year of livetime. The average event size at Level 2 is around 15 kB, which would result into around 30 TB of data per year of livetime.

Therefore, five quality cuts are implemented with a goal that is threefold:

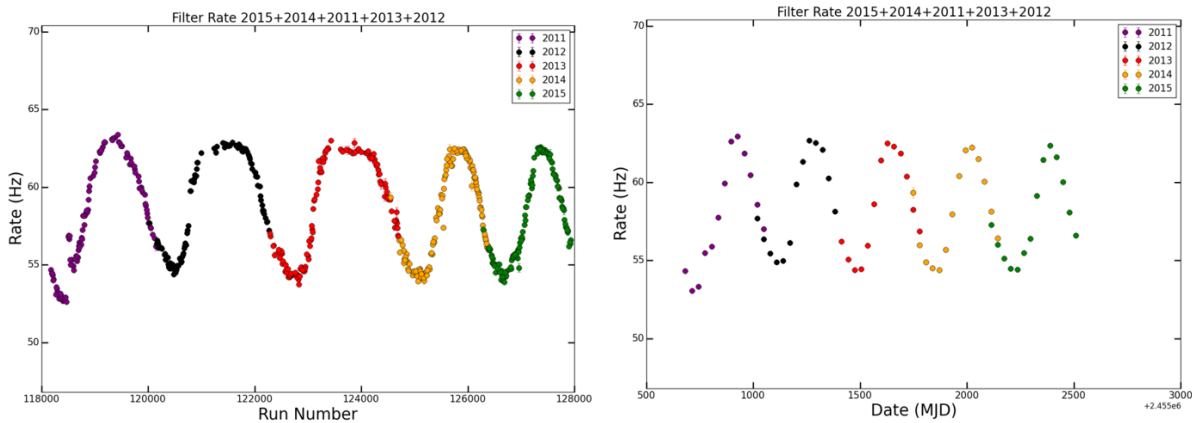


Figure 8.4: *Left:* Total rate of the combined filters as a function of the run number. *Right:* Total filter rate averaged per month. There is an overlap for each year because a new season does not necessarily start at the beginning of a month.

1. Reduce the data rate,
2. Improve the signal to background ratio, increasing the selection purity,
3. Improve the agreement between data and Monte Carlo (as can be seen in Figure 8.1).

These cuts are shown in Figures 8.5 to 8.9 and explained below.

8.2.1 The zenith angle cut

Even though there are no upgoing muons from air showers expected, the vast majority of events that pass the filter selections still originate from muons that are mis-reconstructed. Even though there is only a small chance of these events to have a reconstructed zenith angle with a large offset from the true angle, the expected flux of air showers is so much larger compared to the assumed signal flux that it still dominates by orders of magnitude. Therefore, a zenith angle cut was set at an angle of

$$\theta_{\text{zen}}(\text{MPE}) \geq 85^\circ, \quad (8.1)$$

where the cut is slightly relaxed to include events coming from the horizon. Muons passing through kilometers of air and ice have a much lower chance of reaching the detector.

The zenith angle distribution of the MPE reconstruction can be seen in Figure 8.5. Several background samples are shown in filled histograms. These samples are stacked together, where the largest samples are added last. The total rate of these Monte Carlo data samples corresponds to the top of these stacked histograms. Events from air showers are referred to as Corsika in the figures. The total statistical uncertainty of the background is indicated with a hatched grey color band. The burn sample is shown with black data points. The error bars correspond to the statistical uncertainty. The simulated signal samples are illustrated with a solid line.

Signal and background Monte Carlo samples are normalized to the livetime of the burn sample.

The upwards trend to higher zenith angles of several samples is due to the filter selections that depend on the angle.

8.2.2 The rlogL cut

The reduced log-likelihood, rlogL, of the track reconstruction fit is used as a goodness-of-fit variable. The term “reduced” is used because the logarithm of the likelihood is normalized by the number of degrees of freedom (NDOF) in the track fit

$$\text{rlogL} = \frac{\log \mathcal{L}}{\text{NDOF}} = \frac{\log \mathcal{L}}{\text{NCh} - \text{NPara}}, \quad (8.2)$$

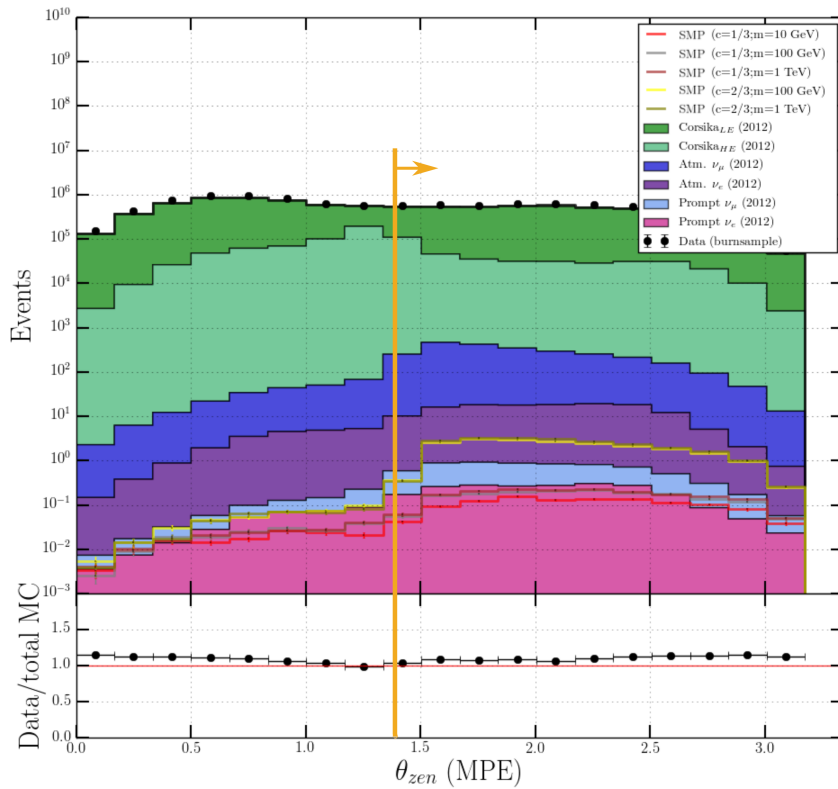


Figure 8.5: Number of events as a function of the MPE reconstructed zenith angle and normalized to the burn sample. The cut is illustrated with an orange line, the arrow points towards the events that are kept.

where NCh is the number of channels/DOMs and NPara the number of fitted parameters (3 for the position and 2 for the track direction). For Gaussian probability distributions this expression corresponds to the reduced chi-square. Lower values indicate better reconstructions*, therefore the rlogL cut was set at a value of

$$\text{rlogL} < 15. \quad (8.3)$$

The rlogL distribution can be seen in Figure 8.6. Data and Monte Carlo disagree at larger values due to non-perfect simulations. Events that lead to bad reconstructions are not, or not well, simulated and are removed with this cut.

8.2.3 The NPE cut

The total number of photoelectrons seen in the detector for an event is correlated to the number of photons that were emitted from the track. The Frank-Tamm formula in Eq. 4.7 shows that particles with a charge < 1 will produce less Cherenkov light. Therefore a cut on the total number of photoelectrons was set at a value of

$$\text{NPE} < 50. \quad (8.4)$$

The NPE distribution can be seen in Figure 8.7. Signal samples with a lower charge clearly show NPE distributions that peak at lower values, as expected.

8.2.4 The starting rlogL cut

The relative probability for tracks to be starting and/or stopping can be estimated with the `FiniteReco` module (see Section 7.1.6). Because many low-energetic muons would be starting and/or stopping in the detector, these likelihoods prove to be a powerful tool in removing these

*Often minimizers are used in likelihood computations, which actually use $-\log \mathcal{L}$.

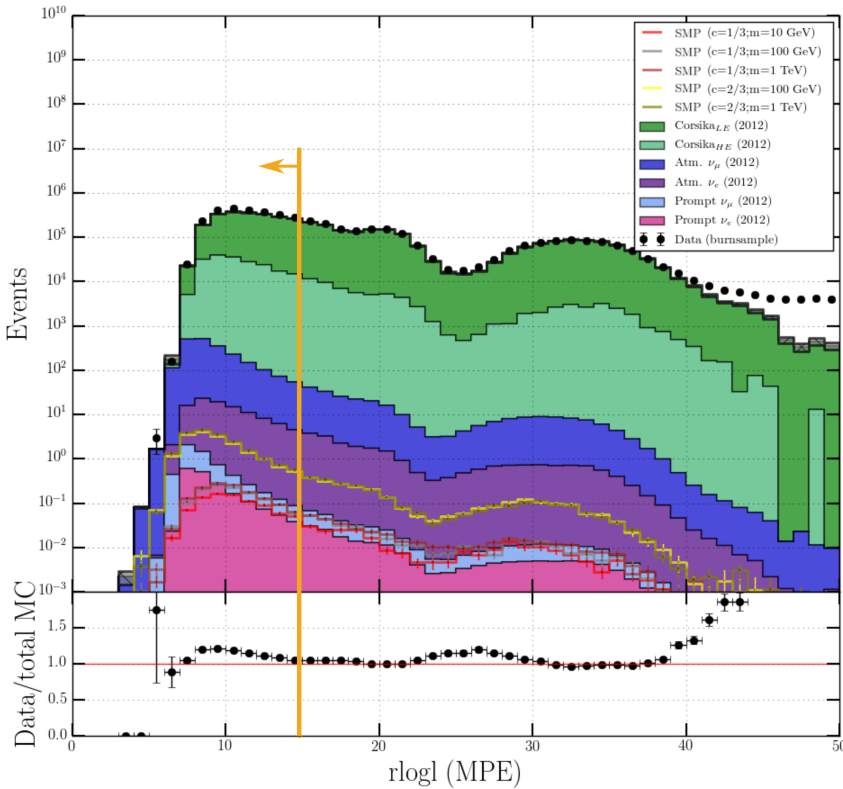


Figure 8.6: Number of events as a function of $r\log L$ normalized to the burn sample. The cut is illustrated with an orange line, the arrow points towards the events that are kept.

events. High-energetic muons will have a higher chance of being throughgoing, but would produce much more light than the dim tracks that are expected for the SMPs. These are mostly removed with the NPE cut.

The likelihood is always compared to the likelihood of throughgoing tracks, hence the “relative probability”. It was chosen to place the starting relative $\log L$ at a value of

$$\text{rel_logL(starting)} = \log L(\text{starting}) - \log L(\text{throughgoing}) > 0. \quad (8.5)$$

The starting $r\log L$ distribution can be seen in Figure 8.8. Because the log-likelihoods are negative, positive numbers indicate larger probabilities for throughgoing tracks. We can see that there is a large contribution of starting tracks in the background due to the filter requirements and previous cuts that focus on dim tracks.

8.2.5 The stopping rlogL cut

Analogous to the previous cut, it was chosen to place the stopping relative $\log L$ at a value of

$$\text{rel_logL(stopping)} = \log L(\text{stopping}) - \log L(\text{throughgoing}) > 10. \quad (8.6)$$

The stopping $r\log L$ distribution can be seen in Figure 8.9. Because the log-likelihoods are negative, positive numbers indicate larger probabilities for throughgoing tracks. We can see that there is a large contribution of stopping tracks in the background due to the filter requirements and previous cuts that focus on dim tracks.

8.3 Level 4

As can be seen in Figure 8.9, most of the background at this point in the analysis still originates from air showers. However, due to the Level 3 quality cuts, the total rate was reduced from around ~ 60 Hz to ~ 2 Hz (as can be seen in Figure 8.1), low enough for more elaborate variables to be computed and more aggressive cleaning. In Level 4, the IceHive splitting and cleaning

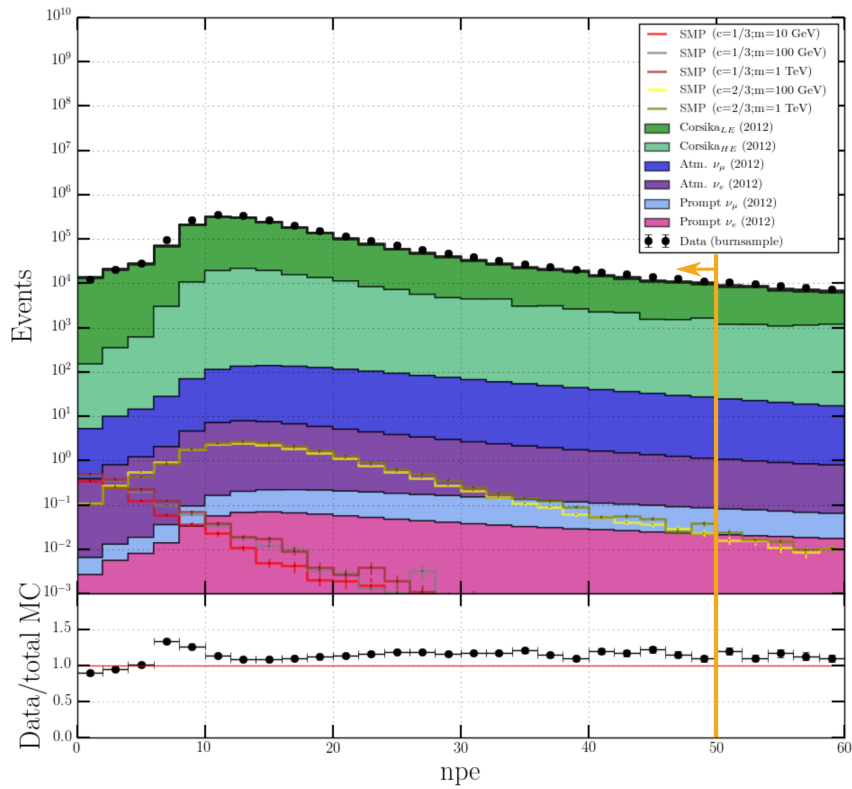


Figure 8.7: Number of events as a function of number of photoelectrons (NPE) seen in the detector. The cut is illustrated with an orange line, the arrow points towards the events that are kept.

Table 8.1: Overview of quality cuts in Level 4.

Variable	Definition	Cut	Motivation
nCh	Number of hit DOMs	≥ 5	Allows for better reconstructions
nStr	Number of hit strings	≥ 2	Allows for better reconstructions
nStr_in	The number of hit inner strings. An inner string is not located at the edge of the detector	≥ 1	Reduce leak-in events
Fitstatus MPE	Status of MPE reconstruction	Status == 'OK'	Remove bad reconstructions
θ_{HC} (MPE)	Zenith angle cut on HiveCleaned pulses	$\geq 85^\circ$	Similar to cut explained in Section 8.2.1: focus on upgoing tracks
Innerstring domination	See text inline	== True	See text inline

tools (see Section 7.3) were implemented and particle reconstructions on these “new” events were run again. Additional quality cuts were added to this level to ensure higher quality events. An overview is given in Table 8.1. Finally, new variables were constructed that will be used in Level 5.

8.3.1 Cleaning and quality cuts

IceHive provides a thorough cleaning method, sometimes resulting into events with a very low amount of hit DOMs. However, a minimal amount of hits is required to have reasonable and trustworthy particle reconstructions. Similarly, more than one string should have a hit to allow for better reconstructions due to the sparse distribution of the strings in the detector. Therefore, there are requirements on the minimum amount of DOMs and strings that should be hit as can be seen in Table 8.1. Because light is able to reach the edge of the detector even if the closest approach of very bright events is tens or hundreds of meters away, it would be near impossible to distinguish bright events far from the detector from dim tracks passing closeby. Therefore, it was required that at least one string that is not on the edge of the detector should have hit DOMs to reduce these *leak-in events*. The zenith angle cut is re-introduced on the new event that should have better reconstructions due to cleaning and finally, there is a requirement for “innerstring domination”.

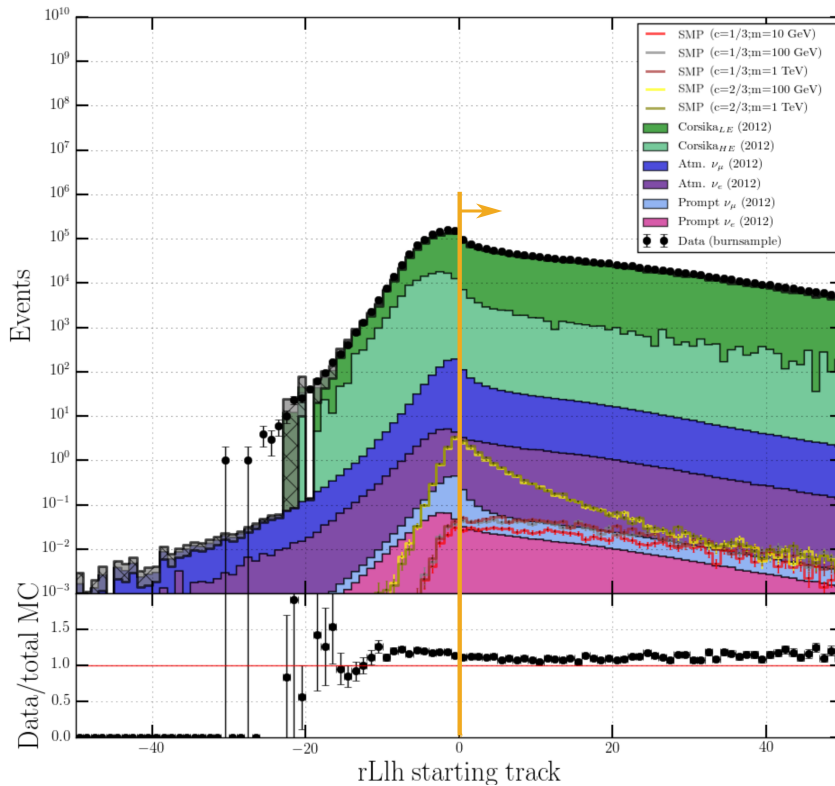


Figure 8.8: Number of events as a function of the starting likelihood. The cut is illustrated with an orange line, the arrow points towards the events that are kept.

Innerstring domination

Several types of events at the boundary of the detector can be a problem for an upgoing track analysis. This includes event classes such as:

- (Leak-in) Events from particles that are heading towards the instrumented volume, but stop right before they reach it or pass close by the detector. These “leak” light to the detector boundaries.
- (Boundary) Events from particles that partially penetrate the detector on the boundary lines and possibly have a cascade at the endpoint. These events have rather cascade-like characteristics.
- (Corner-clippers) Events from particles that are throughgoing on the corners of the detector and therefore have a COG at a corner of the detector*.
- (Leak-out) Events originating from a neutrino that passes through almost the entire length of the detector and only has an interaction vertex right before leaving the detector. Depending on position and angle, the reverse direction of reconstruction can be of similar probability and thus a nuisance.

All these event classes have a high uncertainty in the reconstruction or even fail the reconstruction completely. Most of these events are removed with the requirement of an “innerstring domination”.

DOMs are defined as outer DOMs if they are one of the following:

- part of a string on the edge of the detector,
- on the bottom of strings 1-78,
- on the top of strings 1-78.

The innerstring domination is set to `True` when

$$\frac{\#\text{outer DOMs}}{\#\text{inner DOMs}} < 0.5, \quad (8.7)$$

*Two coincident corner-clippers could be a large nuisance in this analysis.

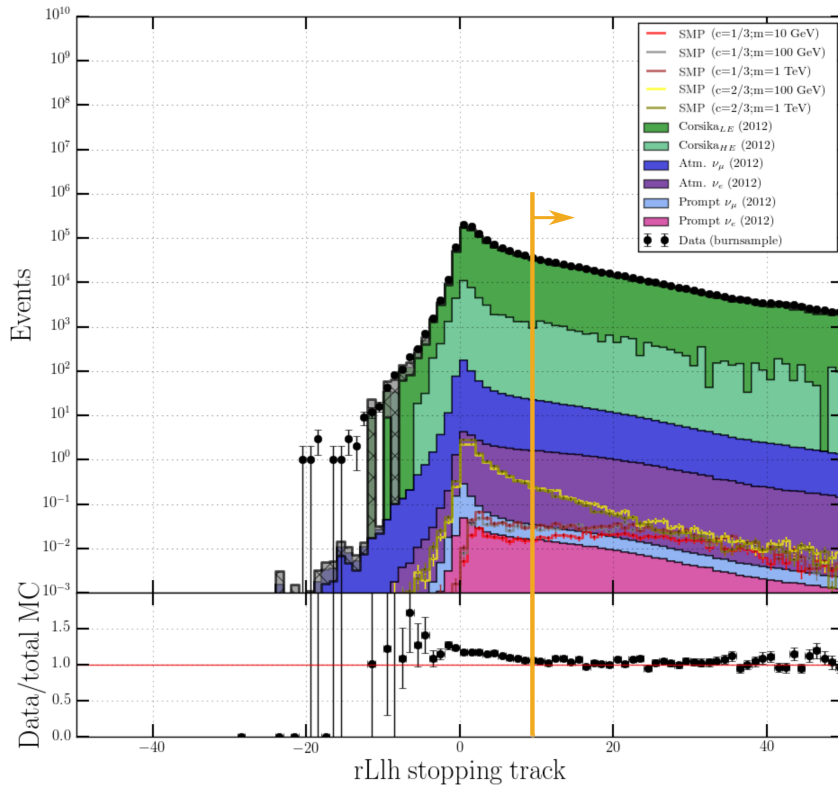


Figure 8.9: Number of events as a function of the stopping likelihood. The cut is illustrated with an orange line, the arrow points towards the events that are kept.

and set to `False` otherwise.

8.3.2 Variable construction

To distinguish signal from background events, variables that show a clear difference in their distribution have the most discriminative power. Therefore, in this part of the analysis, several new variables are introduced with this goal. Some variables used in Level 5 are already explained in Chapter 7 and are briefly mentioned in Section 8.3.2.4. A summary of all the variables that are constructed in Level 4 is given in Table 8.4.

8.3.2.1 Commonvariables

Many analyses in the collaboration characterize certain parameters of an event in a similar fashion. However, some of these parameters were constructed slightly different, making them a cause of errors*. Multiple variables were therefore combined into one project, called “Commonvariables”. The variables used here can be subdivided into three categories: track characteristics, hit statistics, and time characteristics and are summarized and explained in Table 8.2. Their distributions are shown in Figures. 8.10 to 8.17.

Because DeepCore (DC) and IceCube (IC) DOMs have different quantum efficiencies (see Section 5.1.2), the pulses from DC and IC DOMs should not be mixed for an unambiguous definition. Therefore either only DC or IC pulses are used to compute these variables depending if an event is *IC dominated* or *DC dominated*, where the former is set at $\frac{\#DOMs_{IC}}{\#DOMs_{DC}} \geq 0.5$ and the latter otherwise.

The variables used in this analysis are listed below.

*For example: how is the length of a track defined? Is it the distance between the two furthest hits? Or the length between the first and the last hit? Or is it the distance between two COGs?

Table 8.2: List of Commonvariables used in this analysis.

Category	Variable	Description
Track Characteristics [†]	AvgDistToDom	The average distance of the DOMs to the reconstructed track, weighted by the total charge of each DOM.
	EmptyHits	The maximal track length along the reconstructed track that got no hits within a cylinder around the track.
	TrackSeparation/COG Separation	Distance how far the COG positions of the first and the last quartile of the hits are separated from each other.
	TrackDistribution	The track hits distribution smoothness value [-1;1] shows how smooth the hits of the given pulse series within the specified track cylinder radius are distributed along the track.
Hit Statistics	ZTravel	ZTravel is the average difference of the z value of all hit DOMs with the first (in time) quartile z value.
	ZMax	The maximum z coordinate of all hit DOMs.
Time Characteristics	ZPattern	All first pulses per DOM are ordered in time. If a DOM position of a pulse is higher than the previous pulse's DOM position, ZPattern is increased with +1. If the DOM position is located lower in the detector, ZPattern decreases with -1. In general, this variable gives a tendency of the direction of a track.

[†] Whenever one of the track characteristics variables is shown/mentioned, the suffix (e.g. “_50”) refers to the track cylinder that was used around the track.

AvgDistToDom

Large values indicate bright tracks or events with many noise hits far away from the reconstructed track (seed track). Therefore, signal events peak at lower values than the backgrounds. This is shown in Figure 8.10.

EmptyHits

Large values indicate that the track is sparse, with two or more clusters of hits that are far away from each other. Background events are not expected to produce long tracks with large parts of missing hits and therefore have much larger contribution at lower values. This is shown in Figure 8.11.

COG Separation

The distance between the COG of the first and last quartile of hits is expected to be large for throughgoing tracks. Therefore, signal events should have a larger contribution at higher values. Background events are not expected to have large COG separations. This is shown in Figures 8.12 and 8.13.

TrackDistribution

The smoothness of a track is rather difficult to be parameterized. The *TrackDistribution* variable was developed and first used by P. Nießen in his PhD thesis [227]. Signal events peak more at values close to zero. This is shown in Figure 8.14.

ZTravel

The average distance between the z -position of all DOMs and the z -position of the first quartile (in time) of all DOMs should be positive for upgoing tracks. Mis-reconstruction in air shower events therefore have a much larger contribution at lower values compared to signal events. This is shown in Figure 8.15.

ZMax

Upgoing tracks should have large *ZMax* variables. Low values for signal events mostly consist of corner-clippers, corridor events, and events that did not trigger DOMs in the upper layer of the detector due to the low light yield. Muons from air shower events often stop in the top of the detector. This explains the large contribution at high values for air showers. The dip just below the origin is due to the dust layer (see Section 5.6). This is shown in Figure 8.16.

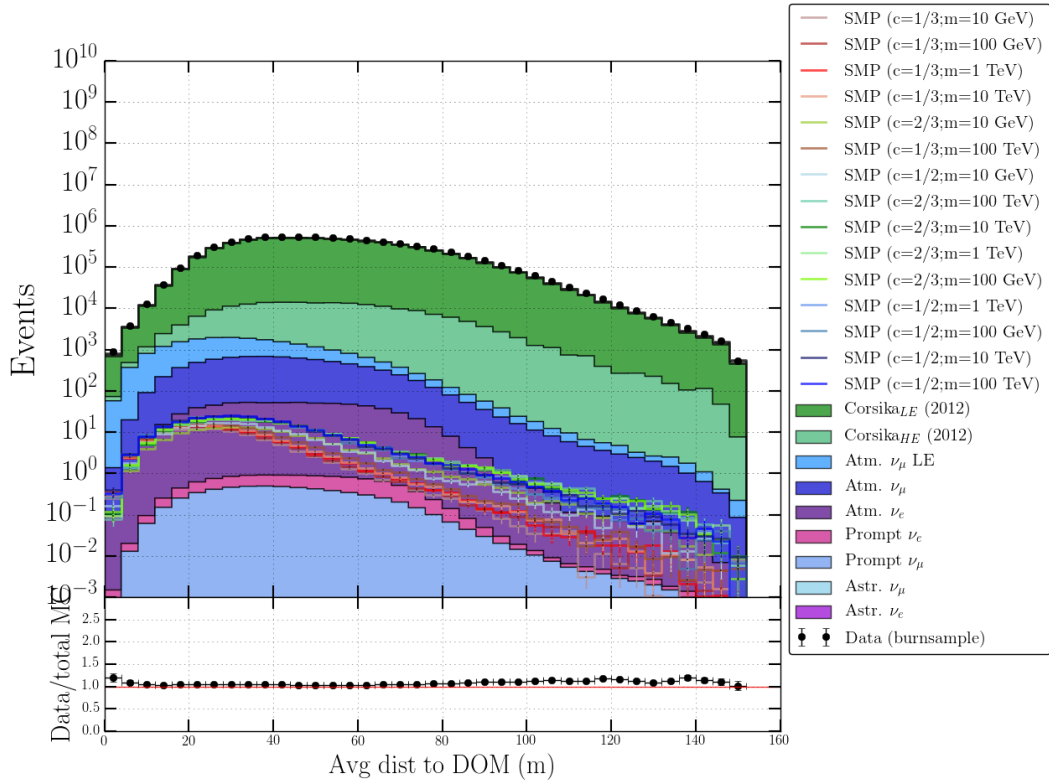


Figure 8.10: Distribution of the average distance of a hit DOM to the seed track. Signal events produce less light, making it less probable for DOMs far away from the track to record light pulses.

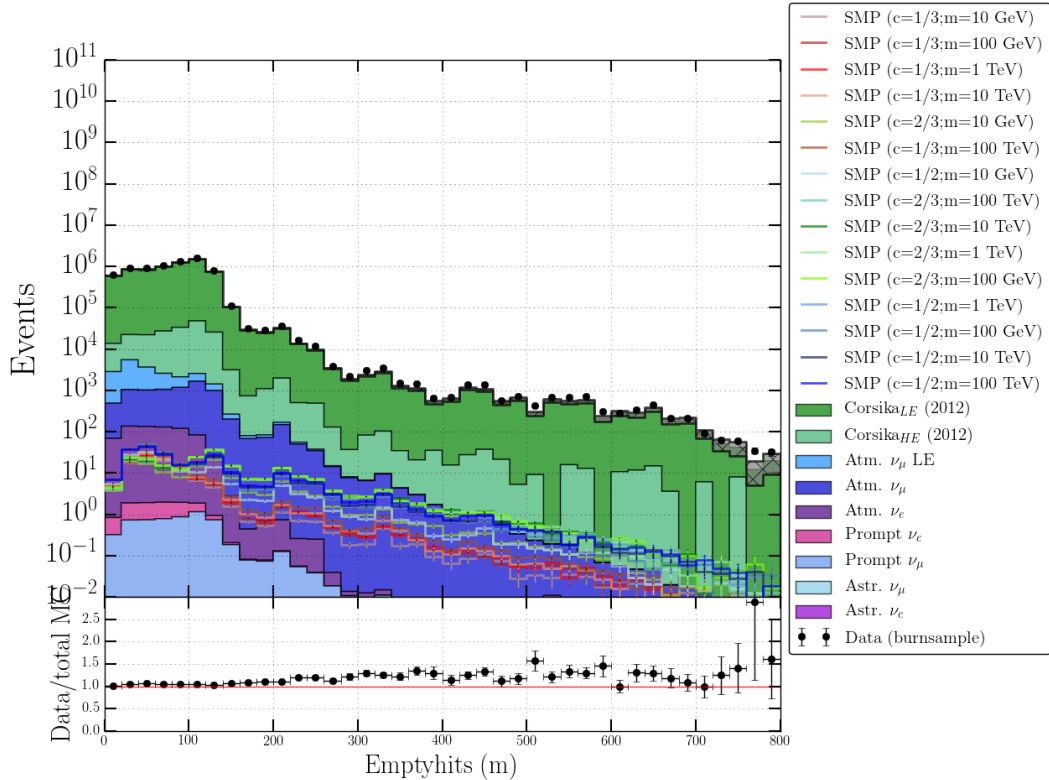


Figure 8.11: Distribution of the length of empty hits along a track. Dim signal events show longer tails in the distribution than the backgrounds.

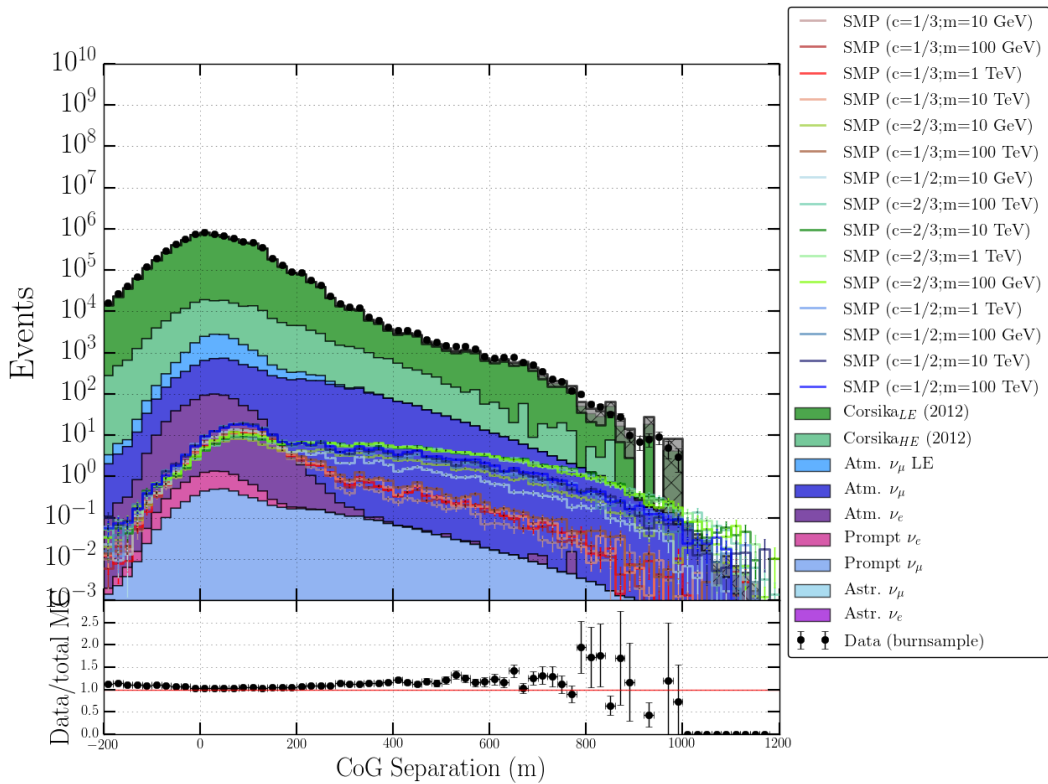


Figure 8.12: Distribution of the TrackSeparation, or COG separation, signal events show longer tails in the distribution compared to muons from air showers, as expected. A cylinder radius of 150 m was used.

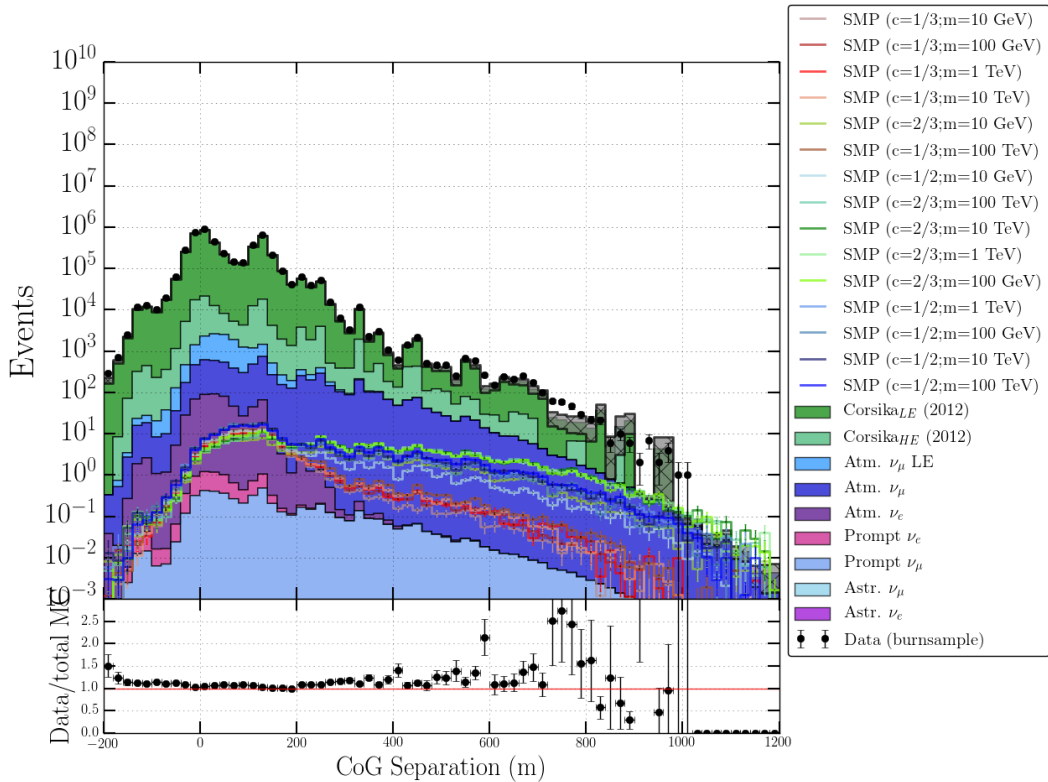


Figure 8.13: Distribution of the TrackSeparation, or COG separation, with a cylinder radius of 50 m.

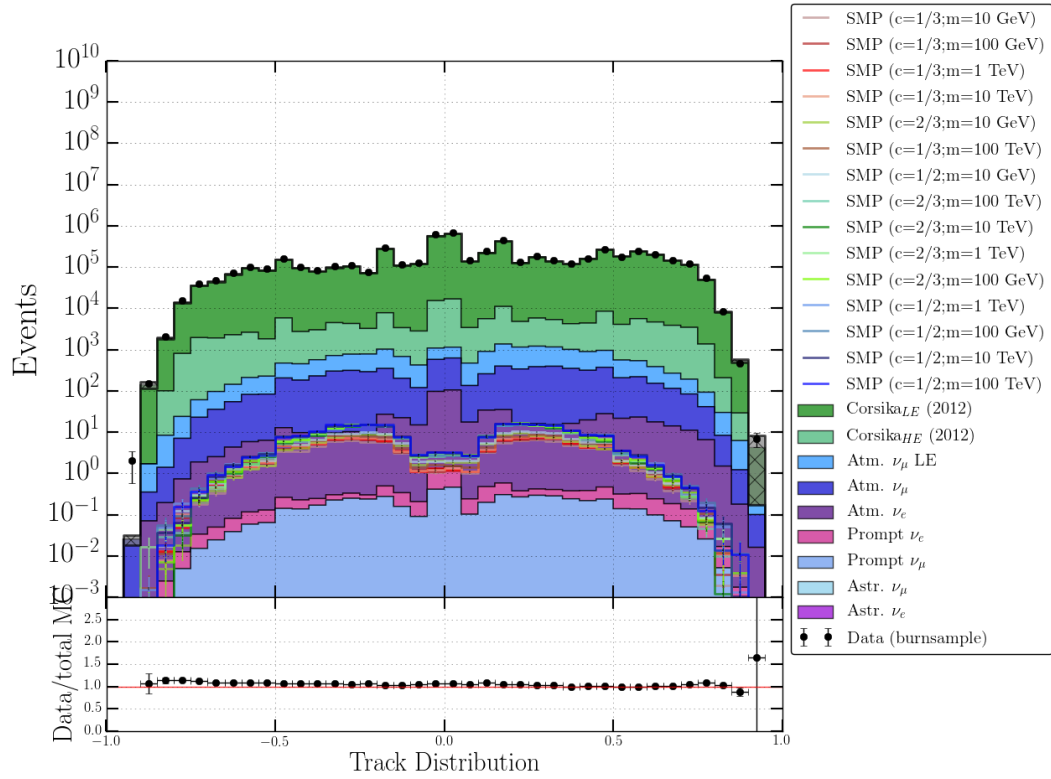


Figure 8.14: Distribution of the smoothness of the track.

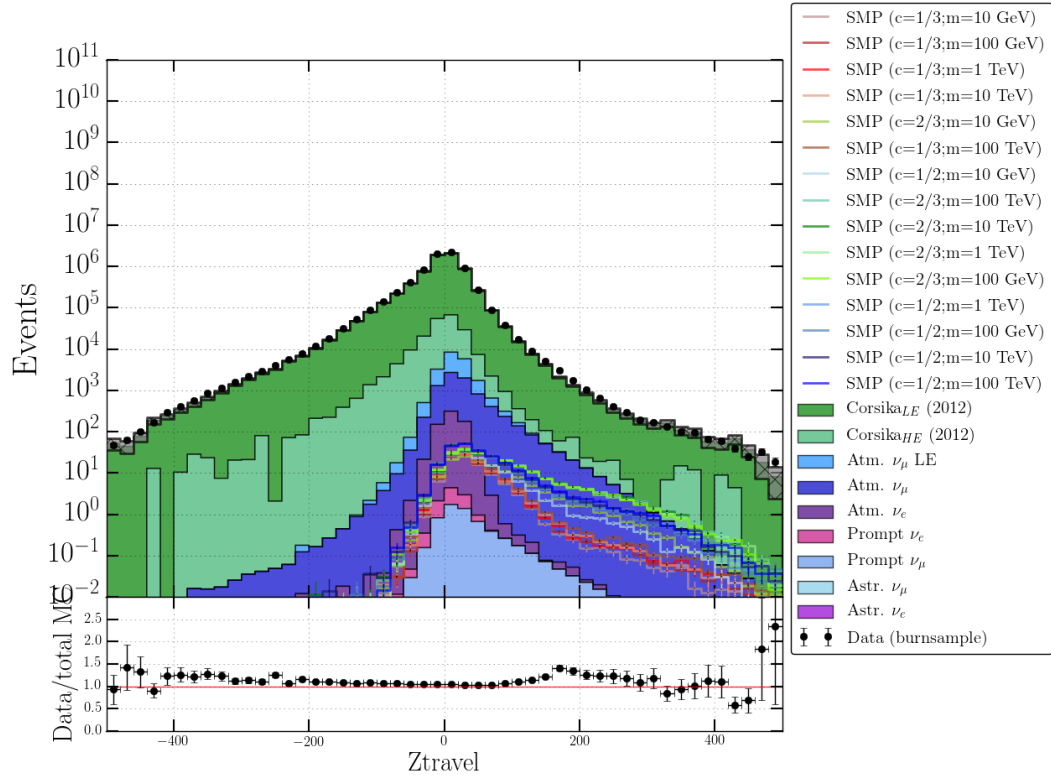


Figure 8.15: Distribution of ZTravel. Negative values indicate downgoing tracks, explaining the differences in signal and muons from air showers.

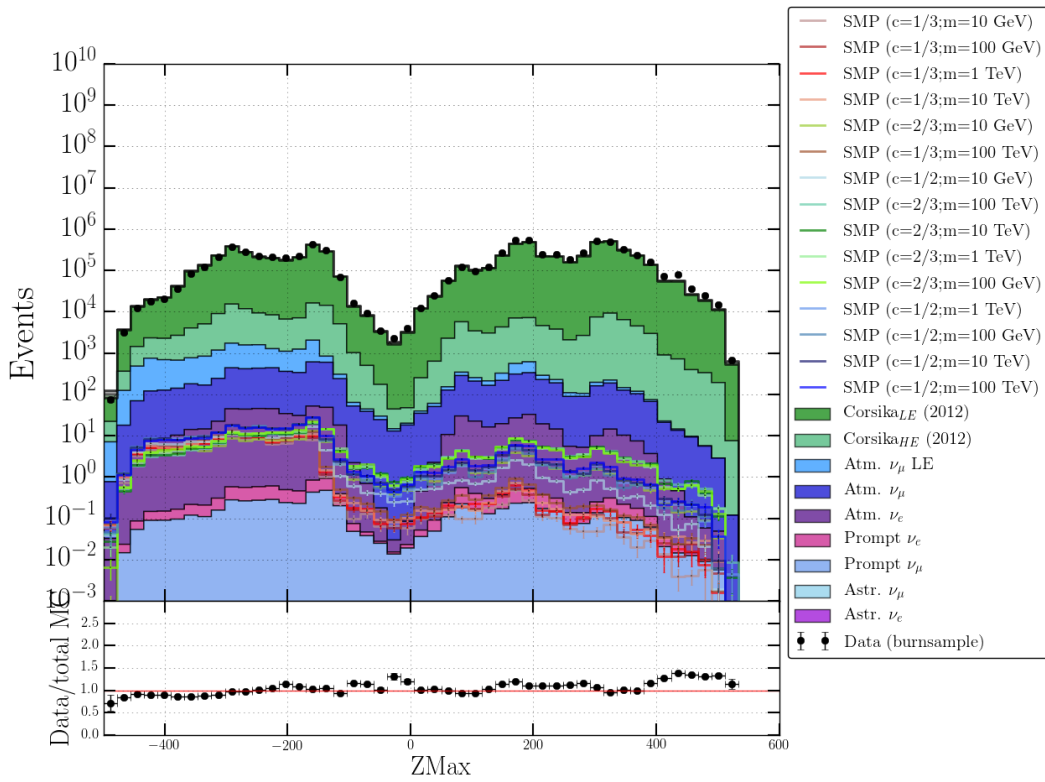


Figure 8.16: Distribution of ZMax. The dip slightly below the origin is due to the dust layer.

ZPattern

This variable is described in more detail in Table 8.2. Upgoing tracks result in positive values, making the variable a tool to discriminate from mis-reconstructed muons from air showers. This is shown in Figure 8.15.

8.3.2.2 Millipede variables

The **Millipede** toolkit was introduced in Section 7.1.5, where it was explained how energy depositions could be estimated from the light seen by the individual DOMs. Constructing multiple variables from this toolkit was the master thesis subject of Stef Verpoest. See Ref. [228] for an elaborate explanation. The variables that were used in this analysis are explained below. Figure 8.18 shows how one fit was performed and can be helpful to explain the variables. The **Millipede** algorithm tries to estimate the energy that is deposited along a track from secondary interactions. The track is subdivided in segments of 15 m long. These deposits can be very small (most of the light originates from the primary particle at low energies), but still hold some information. In the example, we see that an SMP particle had several energy deposits along the track (green lines). The algorithm estimated that more energy deposits occurred close to the true deposits (that are known from the Monte Carlo samples). From this **Millipede** fit, several variables are constructed.

Mean loss

The most straightforward use of the estimated energy loss rate is by taking the mean value and is referred to as *Mean_dEdX*. As can be seen from Figure 8.19, the distribution of SMPs peaks at lower values than known backgrounds, as expected. Energy losses that are reconstructed to come from outside the detector are removed.

Due to the squared charge dependencies, an SMP of charge 1/3 is expected to have a relative energy loss difference to muons with a factor of 9, which is the case when comparing to muons from neutrino interactions. We don't really see an exact factor of 9 difference as the algorithms still *assumes* that a muon is passing through. Still, a significant shift is visible. Atmospheric

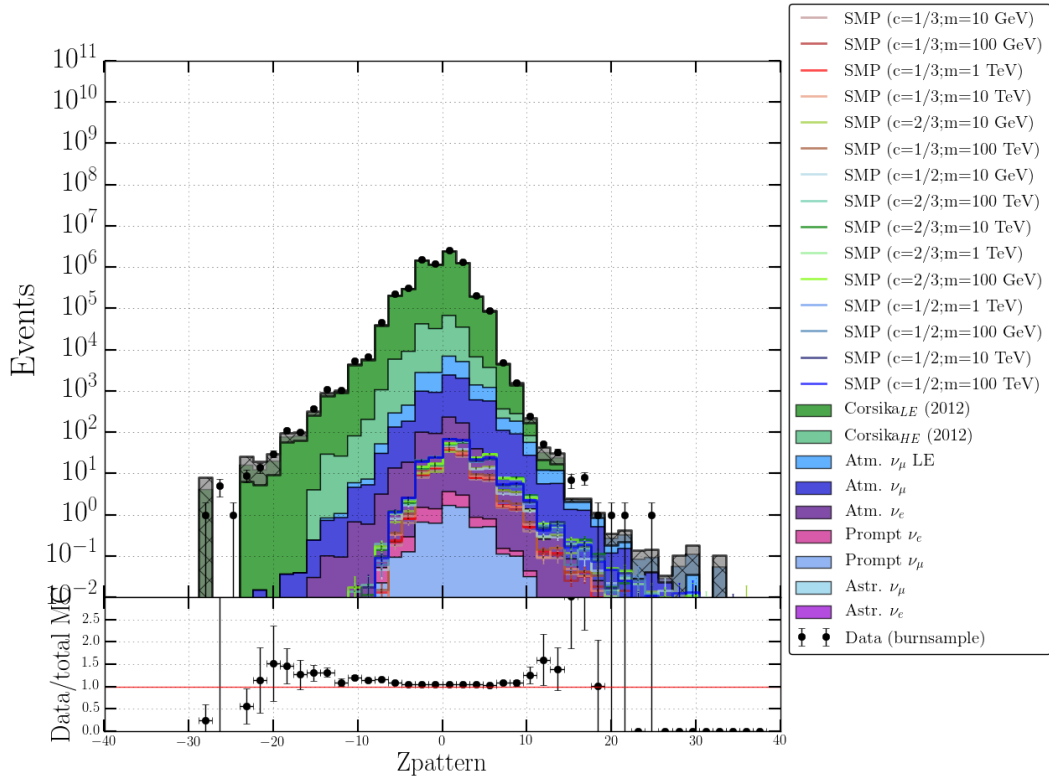


Figure 8.17: Distribution of the ZPattern of a track. Negative values indicate downgoing tracks, explaining the different behavior in signal and background.

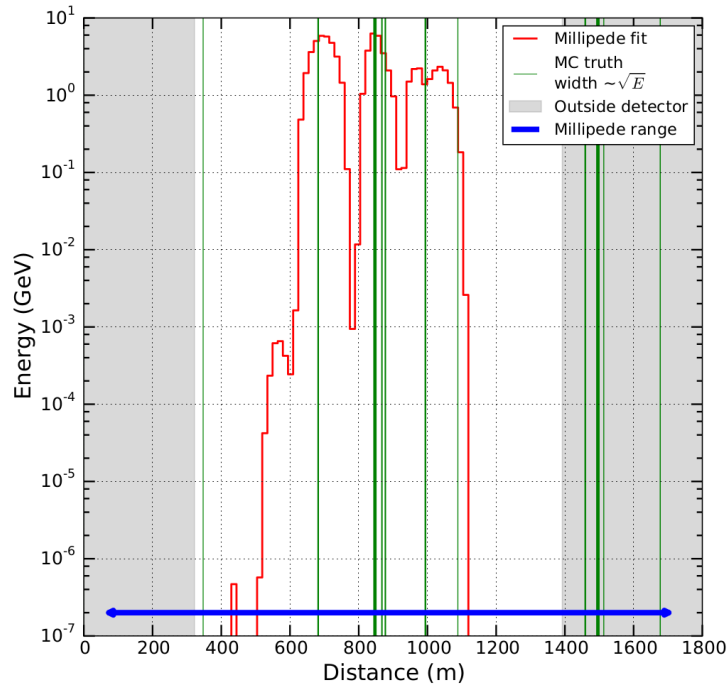


Figure 8.18: Output of a **Millipede** fit for a simulated SMP with charge $\frac{1}{3}$ and mass 10 GeV. The x-axis shows the distance the particle traveled and starts after the first energy loss event. The fit tries to estimate the energy deposited in 15 m track segments. As a comparison, the true positions of energy deposits from the MC simulation are shown in green. Locations outside the detector are shaded in grey.

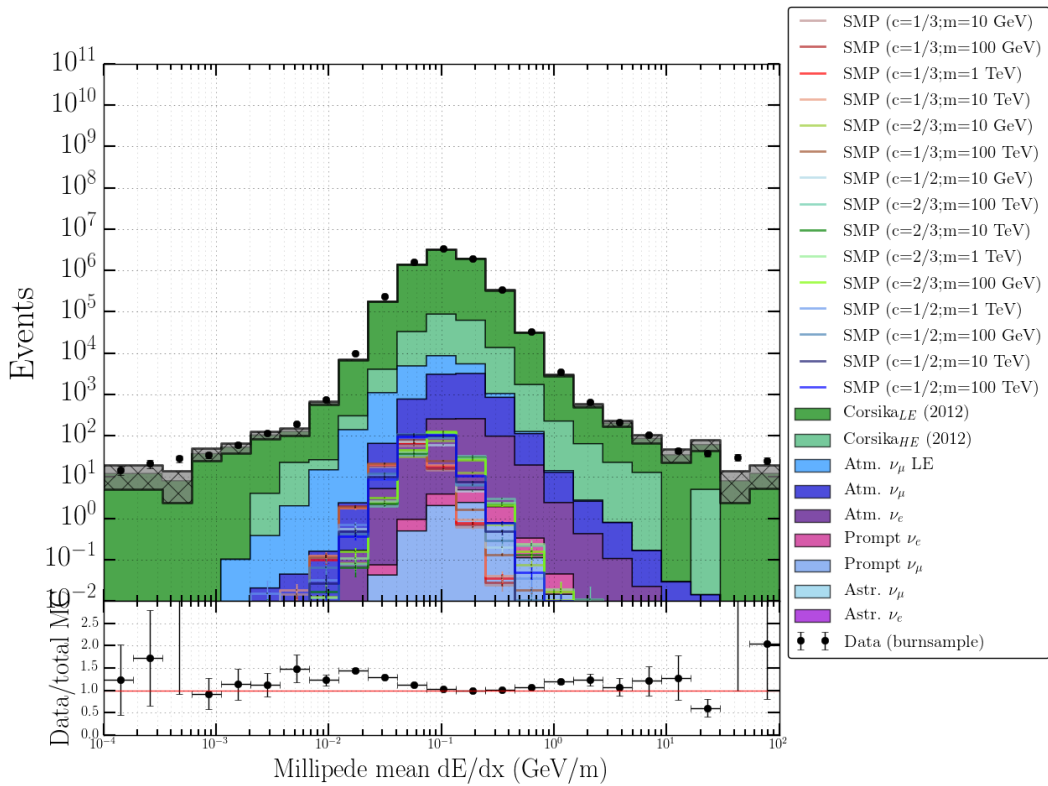


Figure 8.19: Distributions for the estimated mean energy loss from the `Millipede` toolkit.

muons in this level are almost entirely the result of mis-reconstructions, corner clippers, etc. making a comparison not valid.

Uniformity

Once the mean is computed, it is possible to count the number of times the energy distribution curve (red curve in Figure 8.18) crosses the mean value. This variable therefore parameterizes the uniformity of the track. The reasoning behind discriminating signal events from background is that most SMPs will induce triggered hits that are distributed less uniformly due to the low amount of light that is produced. Particles therefore need to travel closer to a DOM to trigger a hit. In Figure 8.20, we can see that the background distributions peak at lower values than the signal, which also has a slower dropoff.

Track length

Because of the lower energy loss, the SMP particles are also expected to travel larger distances than muons, supporting the idea to construct a variable that is sensitive to the distance traveled in the detector: a track length.

Since the tracks at this level induce very dim events, many segments from the `Millipede` output are reconstructed with zero energy. Therefore, it was chosen to use a certain part of the segments. The variable used here, `TrackLength_60`, returns the length where 60% of the energy was deposited. It is the distance between the track segments where 20% and 80% of the energy was deposited. We expected to see larger tails in the distribution of Figure 8.21 in the signal compared to the background. However, sub-optimal reconstructions result in bad millipede fits, giving a low and almost constant energy loss along the track. Additionally, coincident events that are not well separated also contribute to these events in the tail. Nonetheless, most of the background events result into low values, still making it a useful discriminative tool.

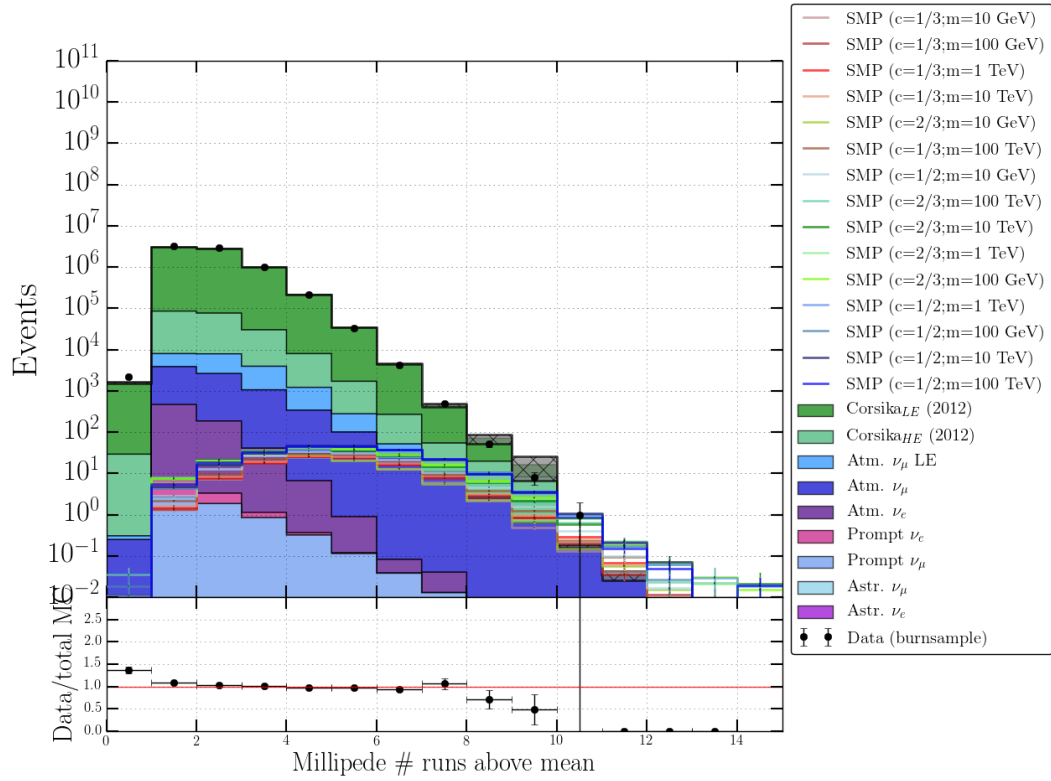


Figure 8.20: Distributions for the uniformity of the contained track.

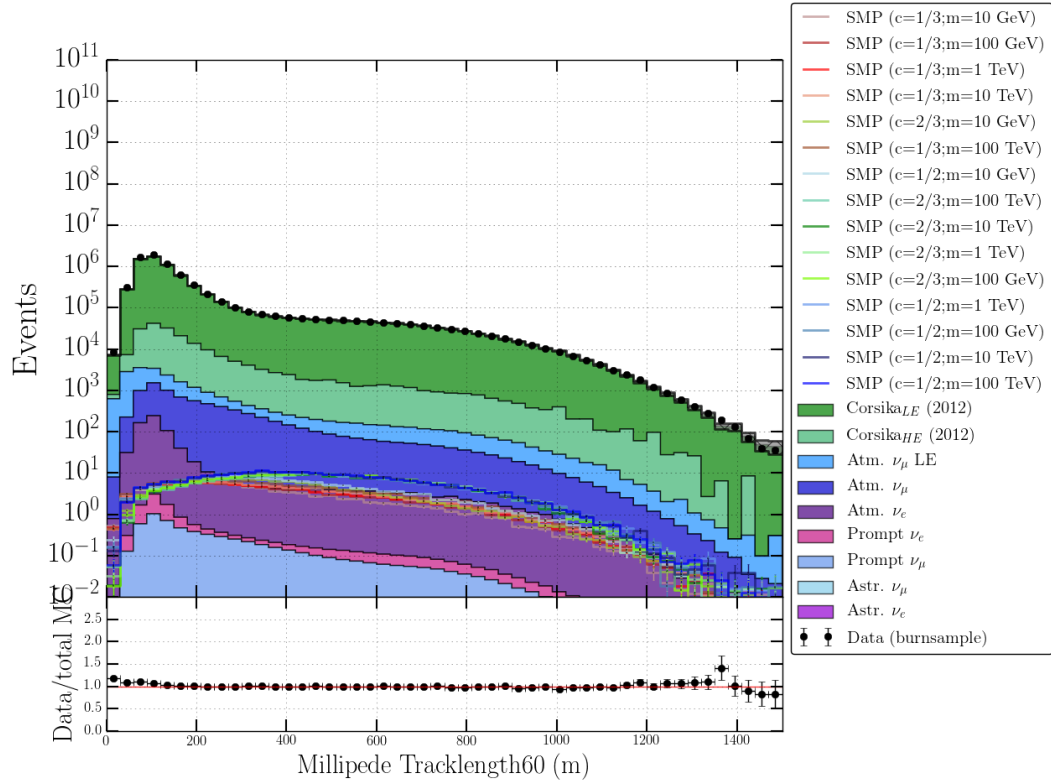


Figure 8.21: Distributions for the track length of the particle where now the **Millipede** segments are used instead of the DOM pulses.

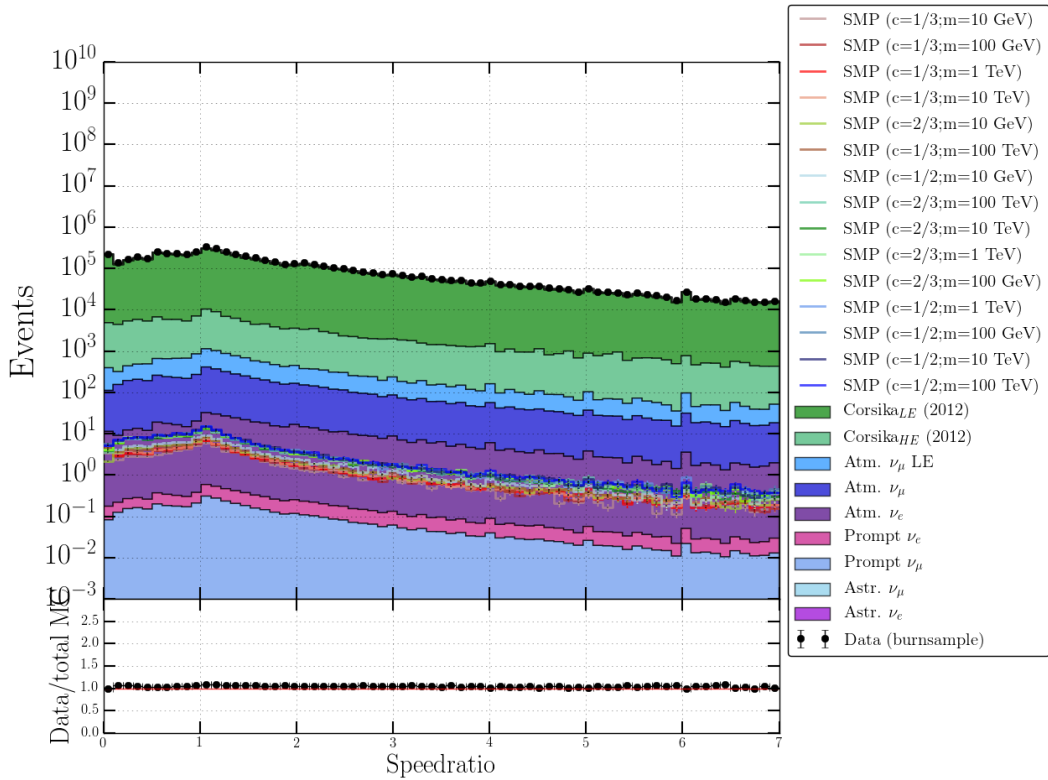


Figure 8.22: Distribution of the Speedratio variable.

8.3.2.3 New variables

Speedratio

In addition, new variables were constructed. One was adopted from Jan Künnen’s Earth WIMP analysis [229]. By looking at the “speed ratio” of the first to second and first to third HLC hits, it was possible to remove erroneous simulated detector noise, helping in data/MC agreement. In this analysis, it showed a modest addition to discriminating variables* (as can be seen in Table 8.4). The *Speedratio* is defined as

$$\frac{v_{12}}{v_{13}} = \frac{d(\text{HLC}_1, \text{HLC}_2) / \Delta t(\text{HLC}_1, \text{HLC}_2)}{d(\text{HLC}_1, \text{HLC}_3) / \Delta t(\text{HLC}_1, \text{HLC}_3)}, \quad (8.8)$$

where $d(\text{HLC}_i, \text{HLC}_j)$ is the distance between the DOMs that recorded the i th and j th HLC hits. $\Delta t(\text{HLC}_1, \text{HLC}_2)$ is the difference in time of the i th and j th HLC hits. This distribution is expected to peak at a value of 1, which is the expected result if one assumes that the photons originate from a particle traversing in a straight line passing close to the DOMs. This is illustrated in Figure 8.22.

NewLength

Because DC and IC pulses should not be mixed, essential information is lost regarding the length of a track. Many signal events are DC dominated (see Section 8.3.2.1), making those track length variables not optimal. This is especially the case for events that have both IC and DC hits and where clusters of hits are far away from each other (which is not expected from low-energetic muons). Low-energetic muons should, on average, not travel very far. High-energetic muons can have large tracks, but are almost completely removed with previous cuts that focus on dim tracks. In this analysis, new variables were constructed that use the MPE track reconstruction as a seed (*seed track*). First, the event is required to have

*In this analysis, data and MC seem to agree well, which is probably due to the newer and better simulations compared to a couple of years ago when the Earth WIMP analysis was done.

Table 8.3: Selection procedure which COGs should be used to compute a track length. f, l, h and q stand for first, last, half and quarter respectively. The left column shows possible timing conditions between IC and DC COGs. The right column indicates which COG is chosen as the first and which one as the last in the four different timing scenarios.

Timing	COG ₁
DC _{f,q} < IC _{f,h}	DC _{f,q}
DC _{f,q} ≥ IC _{f,h}	IC _{f,h}
	COG ₂
DC _{l,q} > IC _{l,h}	DC _{l,q}
DC _{l,q} ≤ IC _{l,h}	IC _{l,h}

- #DC pulses ≥ 4 ,
- #IC pulses ≥ 2 ,

since otherwise the hits would mainly consist of noise hits. Additionally, pulses that lie within a cylinder (with the seed track as the center) are selected. The radius can be chosen, but is of the order of 50-150 meters. This radius is shown with a suffix after the variable (e.g. “_100”), if the radius is infinite (all pulses are used), the suffix is “_all”.

Then the first/last quartile in DC hits and the first/last half of the IC hits are determined. For each quartile/half, one can easily calculate a COG. To determine the length of a track between four COGs, two have to be selected. The selection is based on the timing information on these COGs and given in the Table 8.3. An illustration how the NewLength variable is constructed is shown in Figure 8.23

Summarizing, the NewLength variable is another attempt in defining the length of the track in the detector. The suffix “_z” is used for the variable that only uses the z -coordinate. Negative values occur when the timing of the two selected COGs is inverted when compared to the seed track (e.g. if the seed track is downgoing but the first COG in time is located below the second) and are present when the reconstruction was not optimal.

The distributions of this variable are shown in Figures 8.24 and 8.25. Signal samples show larger contributions at higher values, showing that the variable is capable of extracting information about the length of a track for dim events. Muons from air shower events show many more low and negative values, as expected. Upgoing signal tracks can clearly be more easily distinguished from mis-reconstructed downgoing muons when only the z -coordinate is used.

8.3.2.4 Other variables

Additional to the 14 variables that were discussed in the previous sections, three extra variables were used in Level 5. These variables are constructed from the reconstruction techniques as discussed in Chapter 7. They are briefly discussed below.

LineFit velocity

The LineFit algorithm was explained in Section 7.1.2. There, we discussed how the velocity of a particle that produces a track in the detector can be estimated. The velocity for a relativistic particle is equal to ≈ 0.3 m/ns. However, because of the simplistic assumptions in the module, we expect the distribution to peak at the velocity of light in vacuum, but have a broad distribution. This can be seen in Figure 8.26. Muons from muon-neutrinos and signal events indeed peak at the velocity of light in vacuum, as expected.

Paraboloid sigma

The Paraboloid module was explained in Section 7.1.4. The *Paraboloid* σ has low values for tracks that have a small uncertainty on the reconstructed direction. Longer tracks from SMPs should have lower uncertainties than the short tracks that are mostly expected from backgrounds. This can be seen in Figure 8.27.

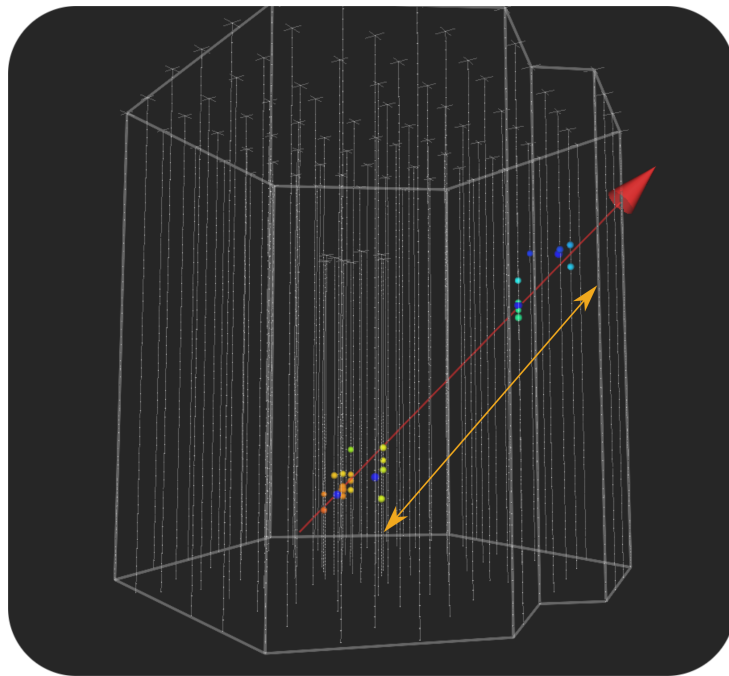


Figure 8.23: The NewLength variable is constructed by selecting the first quartile/half of the COGs of DC/IC and computing the distance from the last quartile/half of the COGs of DC/IC. Out of the four, the first and last in pulse time are chosen to compute the distance.

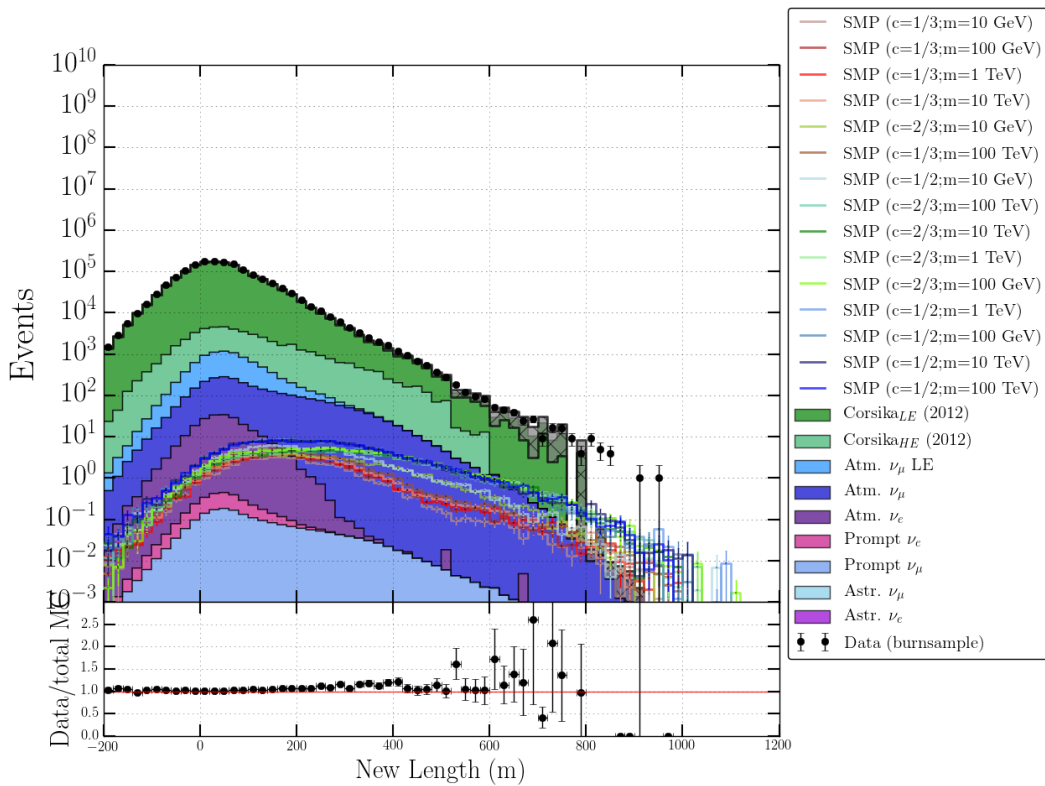


Figure 8.24: Distribution of the New Length_150 variable.

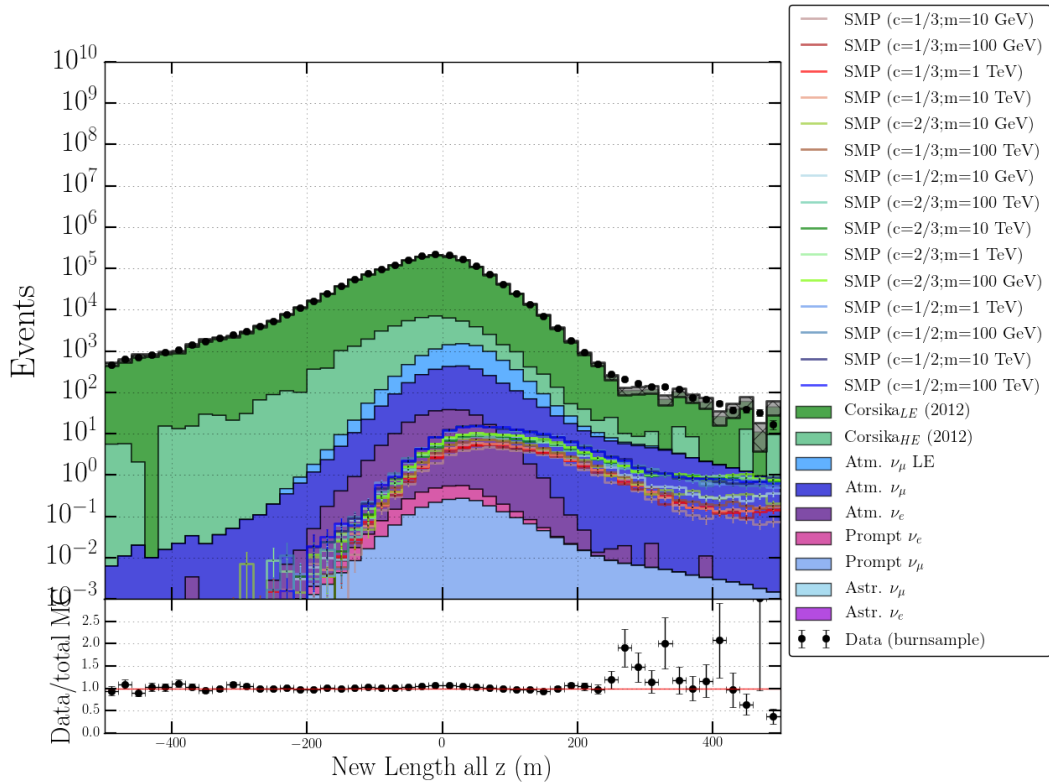


Figure 8.25: Distribution of the New Length where we only focus on the z -coordinate.

SPE zenith

After cleaning with the `IceHive` module, the SPE and MPE reconstructions were re-applied. Negative values of $\cos(\theta)$ indicate upgoing tracks. There is only a small fraction of SMP tracks that are reconstructed as downgoing after cleaning with the `IceHive` module, whereas a much larger fraction of the air shower background is now (correctly) reconstructed as downgoing. This can be seen in Figure 8.28.

8.3.3 Variable selection

The variables that are used in the BDT at Level 5 were selected by using the mRMR technique that was explained in Section 7.6. The 17 most important variables were used in the BDT. Less variables meant a lower performance while more variables did not show to add additional power in the BDT performance and meant more computational resources were necessary. In a BDT, one variable will be more important than another. Some variables have a much larger discrimination power than others. Therefore, an overview of all the variables used in Level 5 is shown in Table 8.4. One BDT was used to show the relative importance (number from 0 to 1) of the variables. The importance is computed by counting the amount of split nodes using each variable and weighing each count by the separation gain and by the overall weight of the tree in the forest. More information can be found in Ref. [230].

DIRK ZEGGEN

8.4 Level 5

The last part of the analysis makes use of the variables that were constructed and the 17 that were determined from the mRMR technique as the most powerful. First, the result from a single BDT is shown. Due to the lack of statistics in the final selection, the pull-validation method was used for a limit computation.

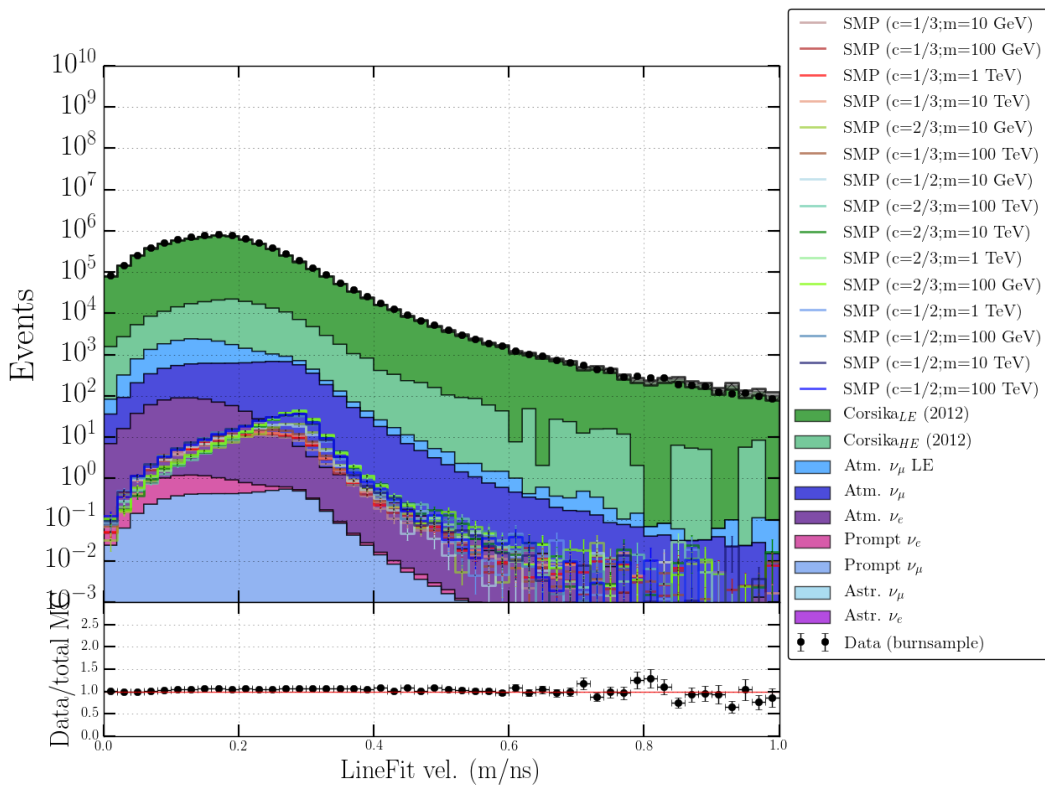


Figure 8.26: Velocity distribution of the LineFit.

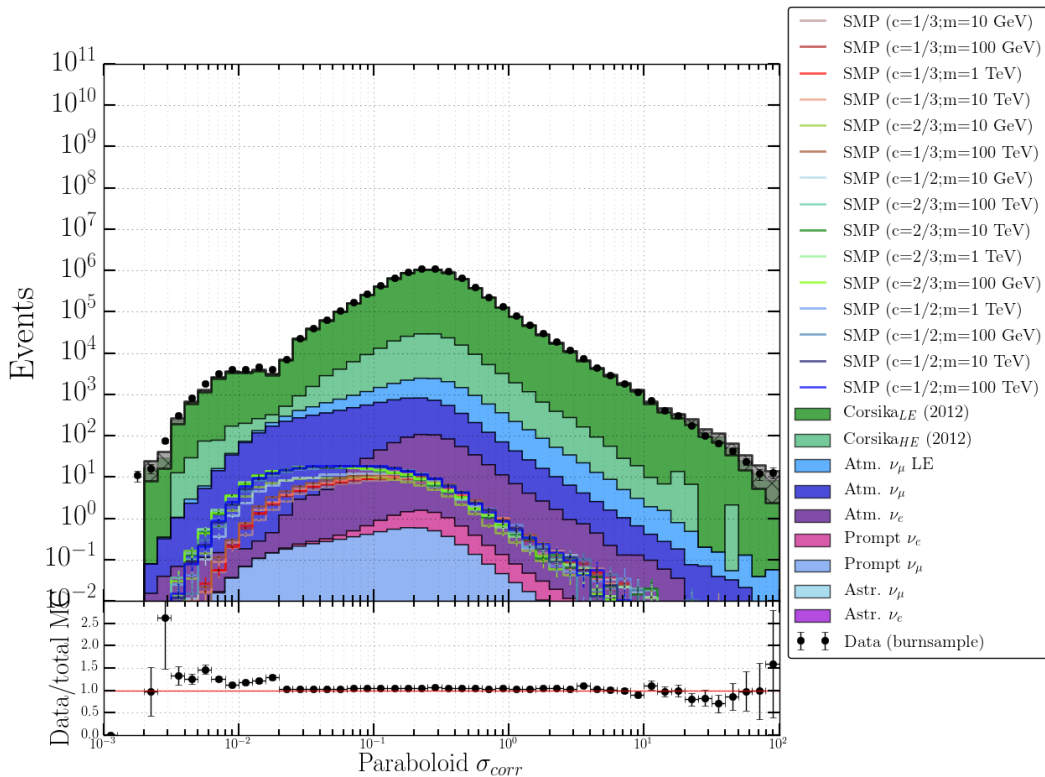


Figure 8.27: Distributions for the Paraboloid sigma.

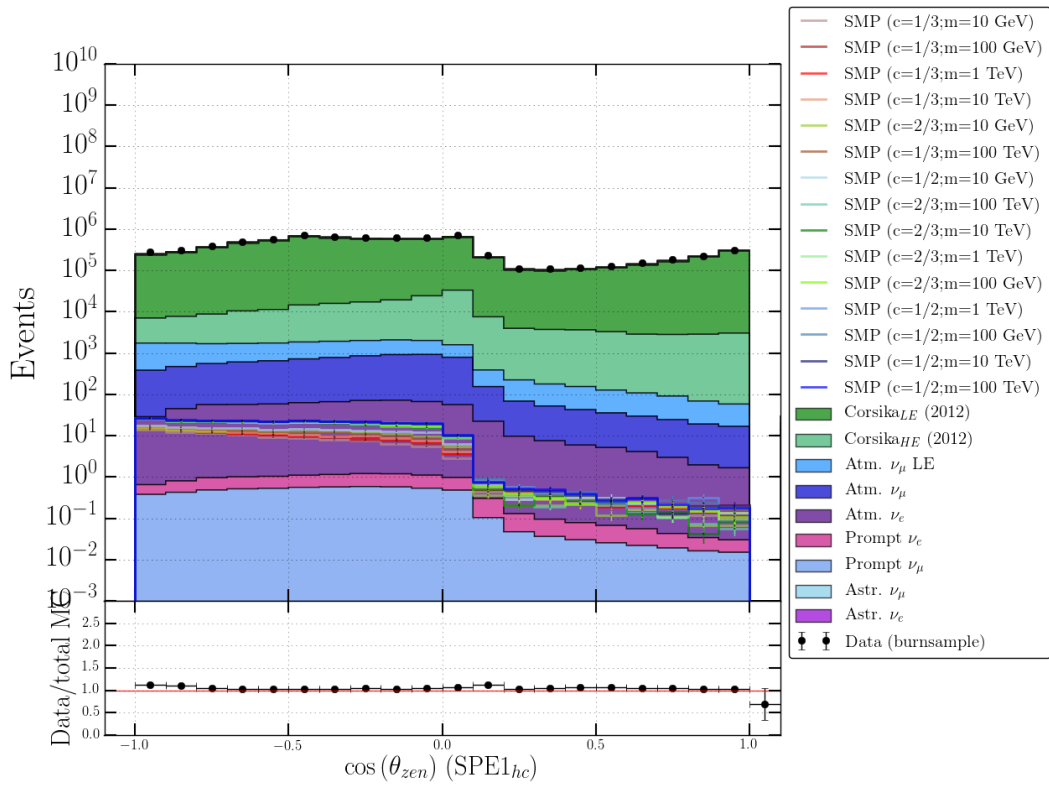


Figure 8.28: Zenith distribution of the SPE reconstruction.

Table 8.4: *Left:* The 17 variables that are used in Level 5 are grouped per class. One BDT was used to show the relative importance (number from 0 to 1) of each variable. The order indicates the rank of which variable is most useful. *Right:* The same variables shown in function of their rank.

Class	Variable	Order	Rel. importance	Order	Variable
Commonvariables	ZMax	2	0.109	1	NewLength_150
	ZTravel	3	0.106	2	ZMax
	AvgDistToDom_150	9	0.048	3	ZTravel
	TrackSeparation_150	10	0.043	4	RunsAboveMean
	TrackDistribution_50	12	0.035	5	Mean_dEdX
	TrackSeparation_50	13	0.034	6	NewLength_all_z
	EmptyHits_100	16	0.027	7	LineFit_Velocity
	ZPattern	17	0.016	8	σ_{para}
Millipede	RunsAboveMean	4	0.105	9	AvgDistToDom_150
	Mean_dEdX	5	0.074	10	TrackSeparation_150
	TrackLength_60	11	0.039	11	TrackLength_60
New variables	NewLength_150	1	0.132	12	TrackDistribution_50
	NewLength_all_z	6	0.059	13	TrackSeparation_50
	SpeedRatio	14	0.033	14	SpeedRatio
Other variables	LineFit_Velocity	7	0.055	15	$\cos(\theta)^{\text{SPE}}$
	σ_{para}	8	0.051	16	EmptyHits_100
	$\cos(\theta)^{\text{SPE}}$	15	0.033	17	ZPattern

8.4.1 BDT result

The parameters that were used for BDT training (see Section 7.7) are:

- Maximal depth: 2 (Figure 7.10)
- Boosting β : 0.8 (Eq. 7.25)
- Number of trees: 400 (Section 7.7.3)
- Pruning factor: 35 (Section 7.7.4.1)

Training is done on 10% of the available burn sample as it showed to have a better performance as opposed to training on background simulation. Training on the background samples showed a systematic disagreement between data and MC testing sets at the high BDT scores, probably due to limited statistics from the simulations at these high scores. The other 90% of the burn sample is used for testing and is shown in the following plots. Testing on the MC data sets is also shown for the sake of completeness. Contribution of possible signal events, if they exist, in the data are minimal. Together with the very good data/MC agreement that is seen in the variables used, the training on data is a valid choice.

Also, it was chosen to select a (large) subsample of the Monte Carlo signal set instead of the complete set to train the BDT to give the best possible results. Some events in the signal MC will produce corner-clippers or leak-in events, which will often be mis-reconstructed. These events should not be used to train the BDT and are therefore removed in the training set. One can see in the variable distributions of Figures. 8.15 and 8.24 that there are minimal contributions of events with negative ZTravel and/or negative NewLength values. Upgoing tracks should give positive values for both and are therefore removed from the signal sample that is used to train the BDT*.

The result of one BDT can be seen in Figure 8.29 and we can draw several conclusions:

- Data and MC show a very good agreement.
- The rate in background events is reduced by 4 to 5 orders of magnitude at a BDT score around 0.25.
- At higher BDT scores, muons from low-energetic ν_μ become a much more significant part of the total background than muons from air showers. This is mainly because the data used to train the decision tree mainly consists of atmospheric muons.
- The signal used for training is more concentrated at higher scores, as expected. The total signal sample and the subset used for training overlap at scores higher than 0.1.
- At the highest scores, where the signal dominates, it is clear that there is a lack of statistics in both CORSIKA simulations and the burn sample to draw sensible conclusions.

Additional checks can be found in Appendix D.

The limited amount of statistics in the tail of the CORSIKA data sets proves challenging. There is a need for an order of magnitude more events, which is not feasible with the available resources. Other techniques, such as defining off-source or off-time regions [231], are not available for this search as we have assumed an isotropic flux that is not time-dependent.

8.4.2 Pull-validation

Another way of dealing with limited statistics is by using re-sampling techniques. The method used here is called *Pull-Validation*[†] (PV) and was used several times before in the IceCube collaboration [184, 232, 233]. It is comparable to bootstrapping and cross-validation (see Appendix C), but uses much smaller training samples. Smaller subsamples means more can be constructed uniquely and more subsamples lead to a larger variability that can be used as an estimator for the variability of the whole sample. As opposed to most bootstrapping and cross-validation methods,

*The final signal rate is computed from the full signal sample.

[†]The term *pull* refers to the “pulling” of subsamples from a larger set, while *validation* refers to the method being used to estimate uncertainties.

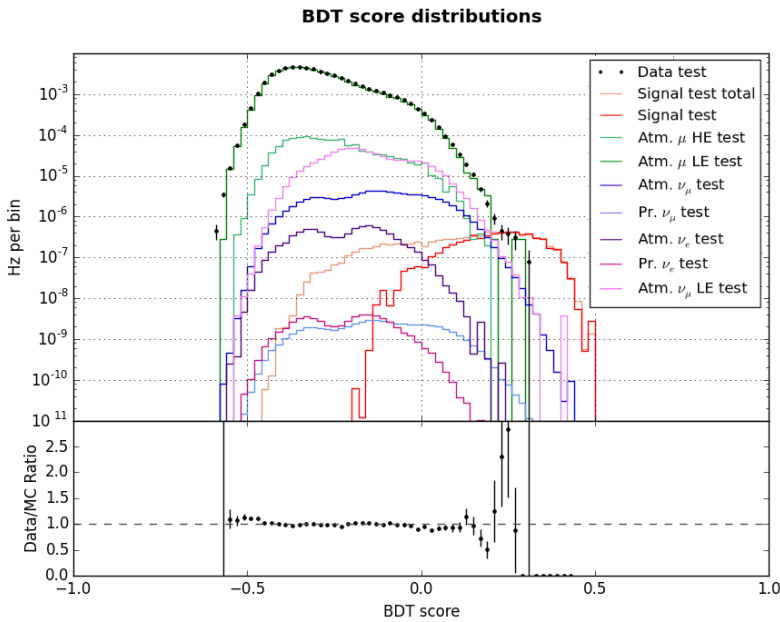


Figure 8.29: Rates of the various testing sample sets in function of the BDT score. Positive scores are more signal-like, whereas negative scores imply events that resemble the background the BDT was trained to recognize. The red curve corresponds to the subset of the signal that was used for training, while the gold curve corresponds to the total signal sample.

the resampling can be done without replacement* because the samples are much smaller.

As can be seen in Figure 8.29, there is a lack of statistics in the region of interest (at high BDT scores), mainly for the data burn sample and atmospheric muon simulations. Because we want to compute an upper limit from this distribution or set a discovery significance, a cut on the BDT score at a value that is higher than for example 0.30 does not result in a trustworthy background estimation. We cannot know from the distribution how the tail evolves into higher BDT scores. A cut on a single BDT implies a binary addition of an event to the final sensitivity: surviving the cut or not, and training the BDT on a slightly different training sample could result into a similar, but different BDT result. By using slightly different training samples, one is able to give an estimate about the tail of the background distributions in function of the BDT score.

Let us assume we have N events making up a sample S . One BDT takes a subset S_1 and uses it as a training sample and using the remaining set for testing, S_2 .

$$k \cdot |S_1| = |S_2| \text{ with } S = S_1 \cup S_2 \text{ and } S_1 \cap S_2 = \emptyset, \quad (8.9)$$

where k refers to the order of missing events that is to be compensated. This factor cannot be made too small as the variability would diminish but cannot be made too large due to the limited size of S . Therefore, k is set at 10. Because S_2 is sizeably larger, the testing sample will extend further than the training sample S_1 as can be seen in Figure D.1.

Pull-validation consists of repeating this procedure a number of times, N_p . For each iteration, the samples S_1 and S_2 are constructed from the sample S and therefore, they consist of different events at each step. By combining the N_p distributions, we can gain additional information from an event by obtaining the Probability Density Function (PDF) of an event in function of the BDT score.

A single event will have one BDT score attributed per iteration and by reprocessing this N_p times, while changing the training sample at each iteration, the variation of an event in function of the BDT score becomes visible and can be used as an estimation of the rate in the tails.

*Selecting without replacement means that when an object is selected from a set, it is removed from the set so that it cannot be chosen twice or more.

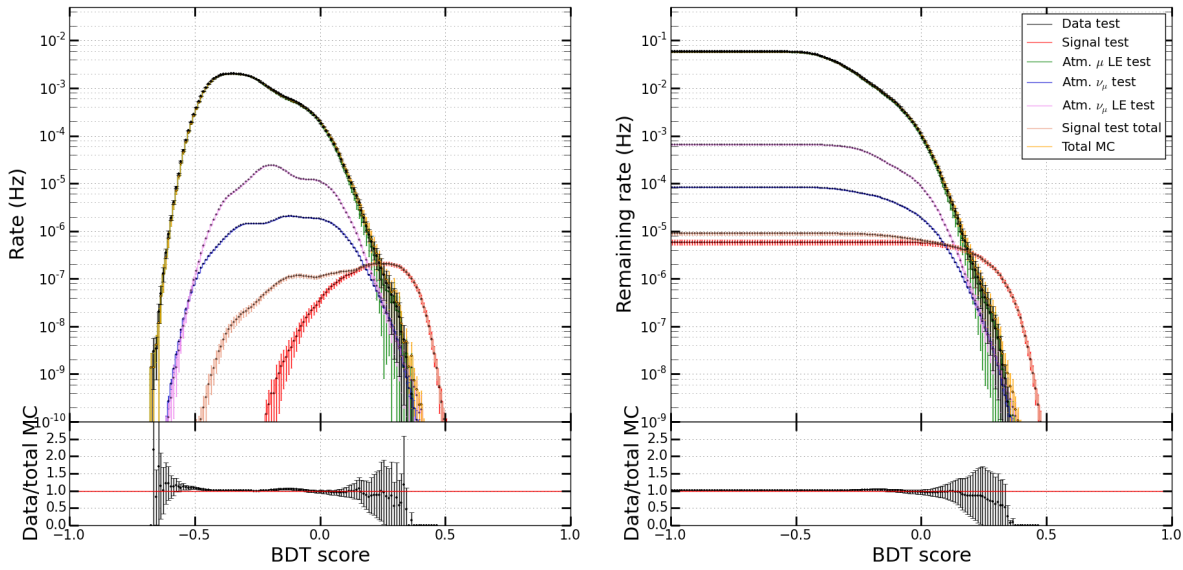


Figure 8.30: Result of the pull-validation method for an SMP with charge 1/2 and mass 100 GeV. Only the most prominent backgrounds are shown. *Left:* rate in function of the BDT score. *Right:* Cumulative rate to the right in function of the BDT score. The y-axis shows the remaining rate of a dataset when placing a cut at a certain BDT score. The weight of an event is given by Eq. 8.10.

Each event gets an appropriate weight, the *PV-weight* equal to

$$w_{PV} = \frac{\#\text{scores above cut threshold}}{N_p}. \quad (8.10)$$

The number of pull-validation iterations, N_p , should be high enough to extract as much information as possible, but low enough so that the subsamples, which are 10% of the total set chosen ad random each time, are still adding information in the variability of the BDT performance. Too many iterations would introduce correlation effects in the subsamples. Previous analyses indicated that $N_p = 200$ is good enough to fulfill these requirements [184, 232]. It is also used in this analysis. The result for an SMP with charge 1/2 and mass 100 GeV is shown in Figure 8.30 and shows the power of PV. Figure 8.31 illustrates how one bin in this histogram is constructed. For a certain BDT score range, a sample will have a rate that changes slightly when the BDT is trained with a different training sample. For example, one BDT estimates a rate of x Hz for the signal between a BDT score if 0.30 and 0.31, whereas another BDT estimates a rate of y Hz for the signal between these BDT scores. These rates, for all N_p BDTS (divided by the average rate), are shown as a histogram in the figure. We can see that lower BDT scores imply more statistics and have a Gaussian-like distribution (left plot). For higher scores, the distribution resembles that of a log-normal or Poisson (right plot). The average rate is computed and used in the pull-validation histogram.

8.4.3 Model Rejection Factor

The question remains where we should place a cut in the BDT score for a significant signal discovery potential or upper limit computation. Since we do not know beforehand if the result will be a discovery or upper limit, the Feldman and Cousins method is used [234]. In this analysis, we want to compute the 90% confidence interval $\mu_{90} = (\mu_1, \mu_2)$, which is a function of the number of observed events, n_{obs} , and of the number of expected background events, n_b

$$\mu_{90} (n_{\text{obs}}, n_b). \quad (8.11)$$

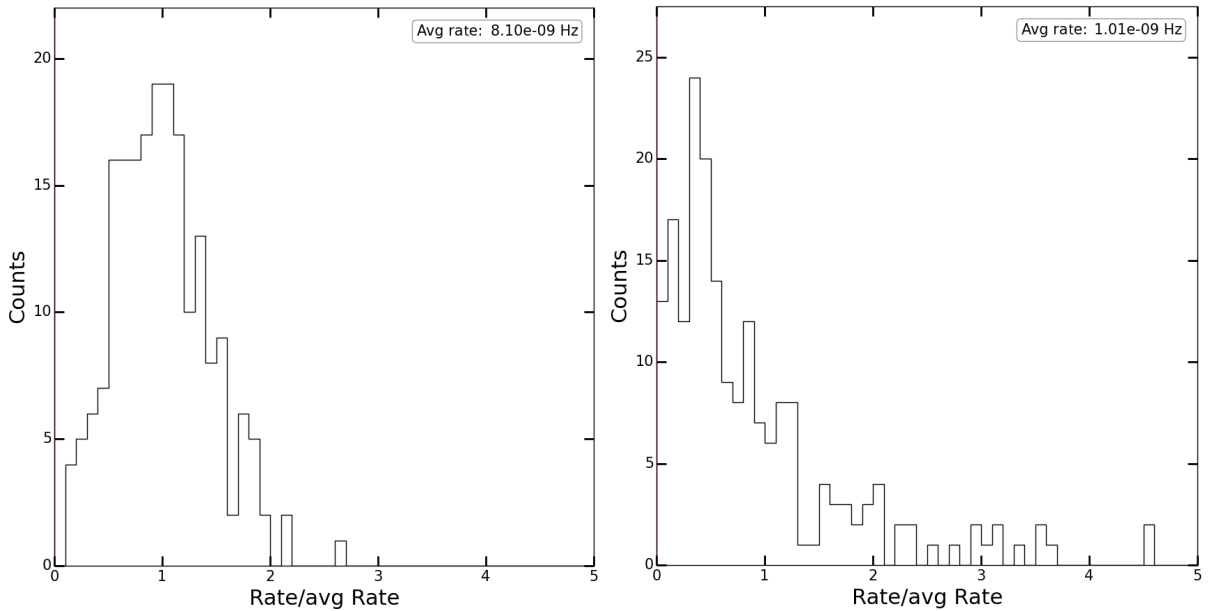


Figure 8.31: Example of an uncertainty distribution of the atmospheric ν_μ background with a BDT score between 0.29 and 0.3 (*left*) and with a BDT score between 0.34 and 0.35 (*right*).

If we assume that the expected number of signal events is n_s , then the 90% confidence upper limit on the signal flux is

$$\Phi_{90\%}(n_{\text{obs}}, n_b, n_s) = \Phi \cdot \frac{\mu_{90}(n_{\text{obs}}, n_b)}{n_s}, \quad (8.12)$$

where Φ is the assumed signal flux of $10^{-14} \text{ cm}^{-2} \text{ sr}^{-1} \text{ s}^{-1}$. It is important to mention that n_s and Φ scale linearly, making the UL *independent* of the assumed absolute flux. Unfortunately, an UL can only be computed once the number of observed events is known. The best *expected* UL could be computed by assuming that the number of observed events is equal to the expected number of events from the MC background. Setting n_{obs} equal to n_b is, however, not a good approach for analyses that have small sample sets at the final level. For example, say one expects 2.5 background events with a 1σ error of 2.1. If, after unblinding, one finds 0, 1, 2, 3, 4, or 5 events in data, this would be considered as consistent with the expected background. The 90% Feldman-Cousins UL are, however, drastically different: $\mu_{90}(0, 2.5) = 1.18$, $\mu_{90}(5, 2.5) = 7.49$. Which is more than a factor of 6 difference! Do we simply take the mean of these two numbers?.

A better way is to assume that the number of observed events is the mean of a Poissonian distribution and we compute the *average upper limit* by summing over all the expected upper limits, weighted by their Poisson probability of occurring [235]

$$\begin{aligned} \bar{\mu}_{90}(n_b) &= \sum_{n_{\text{obs}}=0}^{\infty} \mu_{90}(n_{\text{obs}}, n_b) \cdot \text{Poiss}(n_{\text{obs}}, n_b) \\ &= \sum_{n_{\text{obs}}=0}^{\infty} \mu_{90}(n_{\text{obs}}, n_b) \cdot \frac{(n_b)^{n_{\text{obs}}}}{(n_{\text{obs}})!} \exp(-n_b) \end{aligned} \quad (8.13)$$

The *Model Rejection Factor* (MRF) is defined as

$$\text{MRF}(n_b, n_s) = \frac{\bar{\mu}_{90}(n_b)}{n_s}. \quad (8.14)$$

Comparing this with Eq. 8.12, we can see that minimizing this factor corresponds to the strongest possible constraint on the expected signal flux. Because in each bin in Figure 8.30 both the number of expected signal events and background events are known, the MRF can be computed in function of the BDT score. This is shown in Figure 8.32 for an SMP with charge 1/2 and

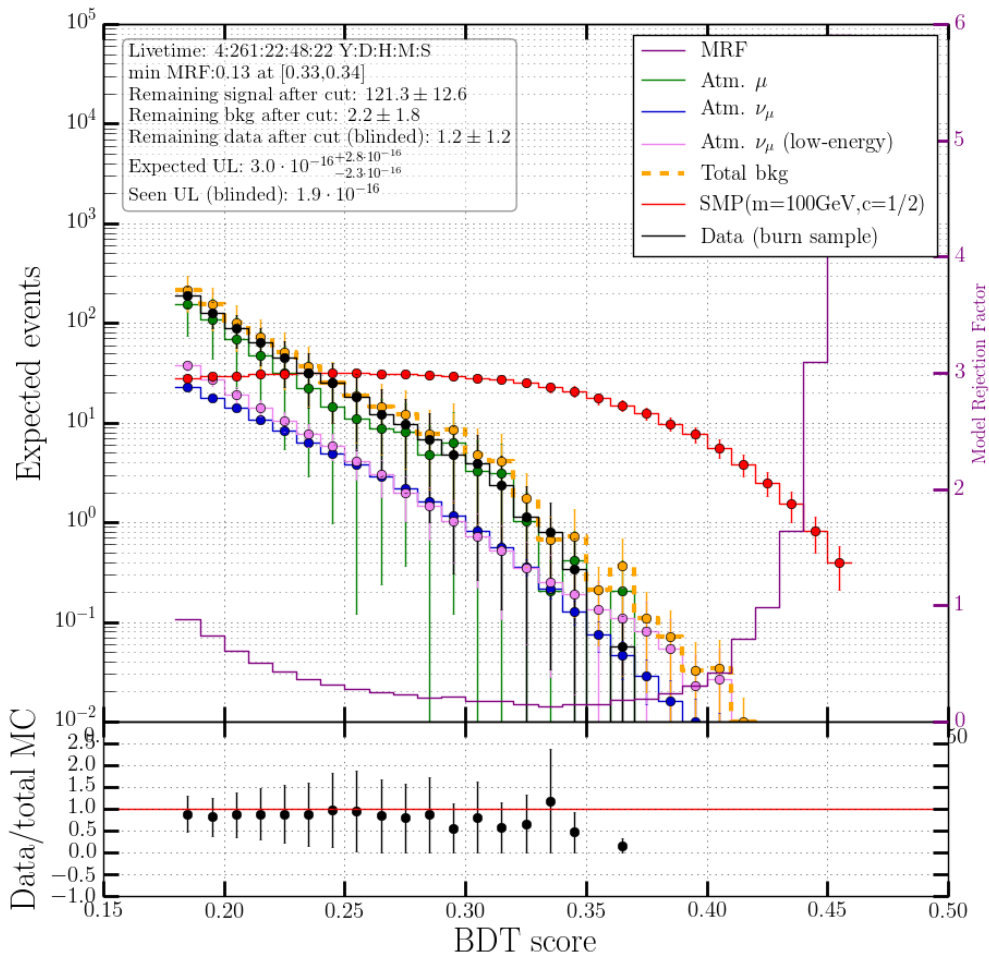


Figure 8.32: Zoomed in version of Figure 8.30, focused on higher BDT scores, again for an SMP with charge 1/2 and mass 100 GeV. Only the most prominent backgrounds are shown. The expected rate is shown on the left vertical axis, while the MRF score can be obtained from the right vertical axis. Only statistical uncertainties are shown as error bars.

mass 100 GeV. In the figure, all samples are normalized to a livetime of 1723 days (≈ 4 years and 262 days). The value of the minimal MRF is shown, together with the corresponding BDT bin. The lowest value of the bin was chosen as the BDT cut for each signal sample. Also, we present the number of expected MC signal events, MC backgrounds, and data (where the burn sample is scaled to the total live time). The uncertainties correspond to statistical uncertainties only. A fake unblinding is presented where we show the expected UL, together with the UL if we would use the burn sample that has more statistics due to the PV method.

After pull-validation, there are enough statistics for a proper MRF computation (purple). The offset of data from MC is a common feature in PV and is accounted for in the systematic uncertainties.

The MRF gives a numerical indication of where we find an optimal trade-off of expected signal and background events. At very high scores, there are less background events expected, but also less of the signal while at lower scores both have higher expectancies.

The BDT score where the MRF is minimized was chosen as the final cut; this is the cut that will probably give the most stringent upper limit or best value for an observation. It's possible that another cut yields more stringent upper limits, but this cannot be known before unblinding the

Table 8.5: Expected number of signal and background events for 5 years of data (see Section 8.5), errors are statistical only. The signal is normalized to a flux of $10^{-14} \text{ cm}^{-2}\text{s}^{-1}\text{sr}^{-1}$. The optimal BDT cut value from the MRF minimization is shown together with the expected upper limit and the statistical error.

Mass	Charge	Remaining MC signal events per 1723 days	Remaining MC background events per 1723 days	$\bar{\mu}_{90} (\text{cm}^{-2}\text{s}^{-1}\text{sr}^{-1})$ $\times 10^{-16}$	BDT cut value
10 GeV	1/2	73.2 ± 7.7	2.2 ± 1.6	$5.0^{+2.9}_{-3.8}$	0.32
100 GeV		121.3 ± 12.6	2.2 ± 1.8	$3.0^{+2.8}_{-2.3}$	0.33
1 TeV		90.7 ± 9.6	0.8 ± 0.6	$1.9^{+2.5}_{-0.18}$	0.35
10 TeV		127.8 ± 11.0	1.8 ± 1.1	$2.1^{+1.4}_{-1.2}$	0.34
100 TeV		107.7 ± 9.7	2.2 ± 1.3	$3.4^{+1.9}_{-2.6}$	0.34
10 GeV	1/3	45.3 ± 5.2	2.2 ± 1.9	$8.2^{+7.7}_{-6.2}$	0.32
100 GeV		60.5 ± 4.1	2.4 ± 1.9	$5.9^{+5.1}_{-4.5}$	0.35
1 TeV		64.0 ± 5.6	3.1 ± 2.7	$6.7^{+5.0}_{-5.4}$	0.32
10 TeV		57.6 ± 4.9	1.2 ± 1.0	$5.5^{+3.4}_{-3.1}$	0.34
100 TeV		79.7 ± 5.9	2.2 ± 1.5	$4.6^{+2.4}_{-3.5}$	0.34
10 GeV	2/3	40.4 ± 4.5	9.6 ± 3.7	$14.2^{+15.1}_{-10.4}$	0.29
100 GeV		71.5 ± 7.5	5.0 ± 1.4	$5.1^{+5.1}_{-1.5}$	0.30
1 TeV		79.3 ± 7.7	7.2 ± 2.1	$6.7^{+4.6}_{-3.1}$	0.30
10 TeV		74.4 ± 7.9	7.9 ± 2.2	$6.3^{+6.7}_{-3.1}$	0.29
100 TeV		59.0 ± 6.0	5.7 ± 1.6	$7.4^{+5.6}_{-2.7}$	0.30

total data set. This should not be done to leave the analyzer unbiased. Therefore, the MRF method uses a Poissonian weighting, which yields us the most probable stringent upper limit. The results can be found in Table 8.5.

8.4.4 Systematic uncertainties

There are four types of uncertainties that are assumed in the result of this analysis, which are listed below

1. **Statistical:** Limited statistics in the final event sample in both the expected signal and background events lead to uncertainties. We assume that the variance of this number follows a Poisson distribution where the statistical uncertainty on a rate is defined as the square root of the rate. The statistical uncertainties can be seen in Table 8.5.
2. **Detector:** Detector simulations assume certain properties of the optical modules and the ice (see Chapter 5), which can differ from true values or are oversimplistic. Therefore, the following detector uncertainties are assumed:
 - DOM efficiency +10%
 - DOM efficiency -10%
 - Ice absorption +10%
 - Ice scattering +10%
 - Ice absorption and scattering -7.1%

The DOM efficiencies originate from uncertainties in the DOM calibrations, whereas the ice absorption and scattering uncertainties are conservative estimates, determined by the collaboration. Therefore, specialized simulation data sets that include these uncertainties were developed and are shown in Table 8.6. Because of the limited statistics in the systematic background sample sets, these detector uncertainties are investigated before the BDT training at Level 4. The effects on the signal were investigated after BDT cuts of 0.30 for charge 2/3 particles and 0.32 for charge 1/3 and 1/2 particles. There were no significant differences found for different masses and these are therefore not specified. Results are

Table 8.6: Overview of the data sets used for systematic uncertainties. Polyg(onato) follows from Ref. [238], GaisserH4a from Ref. [236] and Bartol from Ref. [237].

Generator	Type	Range [GeV]	Sim. γ	Weighted γ	Ice	Dataset	Syst. Eff.
CORS.	Hoerandel	$600 - 10^5$	Polyg.	GaisserH3a	SpiceLea	11527	DOM eff. -10%
CORS.	Hoerandel	$600 - 10^{11}$	Polyg.	GaisserH3a	SpiceLea	11526	DOM eff. +10%
CORS.	5-comp.	$600 - 10^{11}$	2.6	GaisserH3a	SpiceLea	12388	Abs. +10%
							Scat. +10%
							Abs./Scat. -7.1%
CORS.	All data sets from Table 6.2			GaisserH4a	SpiceLea	Table 6.2	GaisserH4a
NuGen	ν_μ	$100 - 10^8$	2	Bartol (syst.)	SpiceLea	11029	Bartol flux
NuGen	ν_μ	$100 - 10^7$	2	Honda2006 + Bartol (syst.)	SpiceLea	11883	DOM eff. +10%
							DOM eff. -10% Abs. +10% Scat. +10% Abs./Scat. -7.1% Bartol flux
NuGen	ν_μ	$100 - 10^8$	2	Honda2006 + Bartol (syst.)	SpiceLea	12346	DOM eff. +10% DOM eff. -10% Abs./Scat. -7.1% Bartol flux

shown in Table 8.7.

3. **Flux:** The models that were used in flux normalizations are not set in stone. Therefore, variations to the flux were assumed to determine the possible discrepancies.

- *SMP flux:* As there is no clear production model or clear possible origin of these anomalous charged particles, the signal flux is assumed to range between E^{-1} and E^{-3} .
- *Atmospheric μ flux:* We look at the difference between the GaisserH3a [102] and GaisserH4a [236] models.
- *Atmospheric ν_μ flux:* We look at the difference between the Bartol [237] and Honda2006 [135] models.

Similar to the detector uncertainties, the effects were computed at Level 4 for background data sets and at BDT cuts of 0.32, 0.32 and 0.30 for particles with charges 1/2, 1/3 and 2/3 respectively. The data sets used for detector and flux uncertainties are shown in Table 8.6. Results are shown in Table 8.7. Because these numbers were computed from relatively small sample sets*, there are uncertainties on these numbers as well. For example, the scattering +10 % uncertainties have an error of around (19.3 ± 14) %, $(3 \pm 10)\%$, and $(3.4 \pm 15)\%$.

4. **Pull-validation:** As will be explained in Section 8.5, only one BDT is used for the final event rate. Pull-validation offers us a way to get more statistics but choosing one BDT for the full data sample and comparing the data rate to the mean of a fluctuating pool of expected background events gives rise to a large uncertainty. It was found that this uncertainty is highly dominant.

For each mass point I have looked at the minimal and maximal offsets between the 200 BDT outputs. As the signal distributions again had enough statistics at higher BDT scores, cuts at values of 0.32, 0.32 and 0.30 for particles with charges 1/2, 1/3 and 2/3 were chosen respectively. Background distributions showed unrealistic large fluctuations in the tails due to very low statistics and single events with high or low weights. Therefore, the BDT cuts were lowered to 0.25 for the backgrounds. The largest discrepancy between the average and the minimum and maximum is set as the uncertainty as a conservative choice. An example is shown in Figure 8.33. The results can be found in Table 8.8.

The final systematic uncertainty is obtained by summing the individual uncertainties in quadrature.

*Data sets that were constructed for systematic uncertainty have much less statistics than the nominal ones.

Table 8.7: Results for the absolute numbers of the detector and flux uncertainties.

Effect	Atm. μ	Atm. ν_μ	SMP (charge 1/3)	SMP (charge 1/2)	SMP (charge 2/3)
DOM eff. +10%	30.9%	2.9%	7.6%	5.2%	3.6%
DOM eff. -10%	26.7%	29.4%	3.5%	16.7%	0.8%
Absorption +10%	23.9%	2.2%	22.7%	18.5%	38.3%
Scattering +10%	3.6%	2.9%	19.3%	3%	3.4%
Abs./Scat -7.1%	17.7%	5.8%	18.7%	6.4%	12.1%
Flux	0.35%	15.28%	1.7%	3%	11.8%
Total	50.7%	33.9%	36.2%	26.6%	42.5%

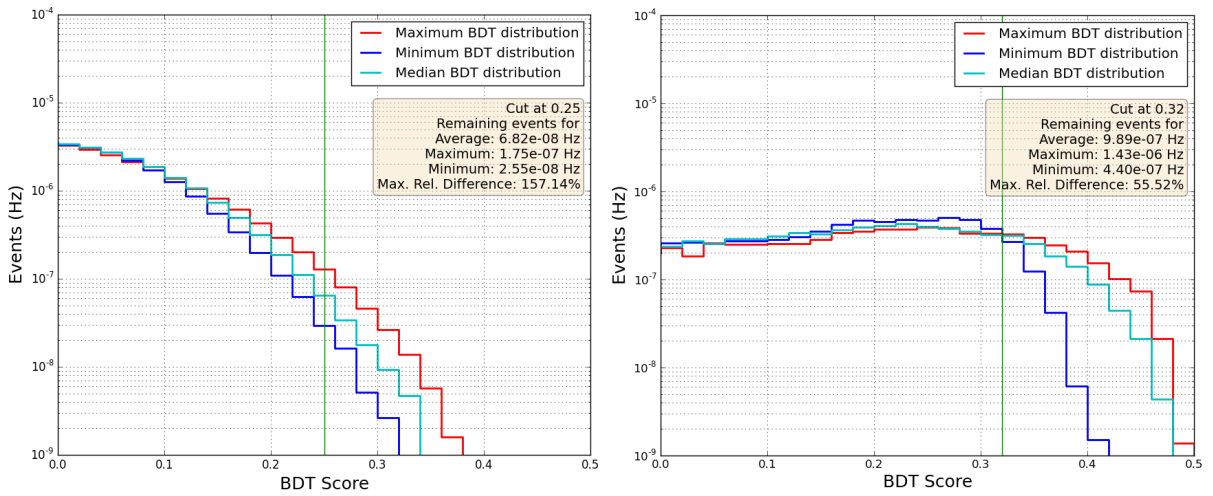


Figure 8.33: *Left:* Illustration how the pull-validation systematic error is computed. Here, the maximum rate, the median and minimum rates from 200 BDT score distributions are shown. *Right:* Similar comparison of BDT score distributions for an SMP with a charge 1/2 and mass 100 GeV.

Table 8.8: Results for the pull-validation uncertainties

Mass	Charge	Atm. μ	Atm. ν_μ	SMP
10 GeV	1/2	66.4%	216.1%	59.8%
		136.3%	157.1%	55.5%
		159.8%	136.3%	42.1%
		211.6%	73.7%	36.7%
		218.4%	135.4%	52.5%
100 GeV	1/3	142%	176.7	39.6%
		174.8%	225.6%	32.9%
		108.3%	167%	40.9%
		190.3%	150%	40.8%
		223.6%	96.8%	35.6%
1 TeV	2/3	63.8%	103.6%	54.8%
		58.7%	88.9%	52.5%
		65.4%	72.5%	61.9%
		10%	104.2%	72.1%
		51.5%	83.4%	43.6%

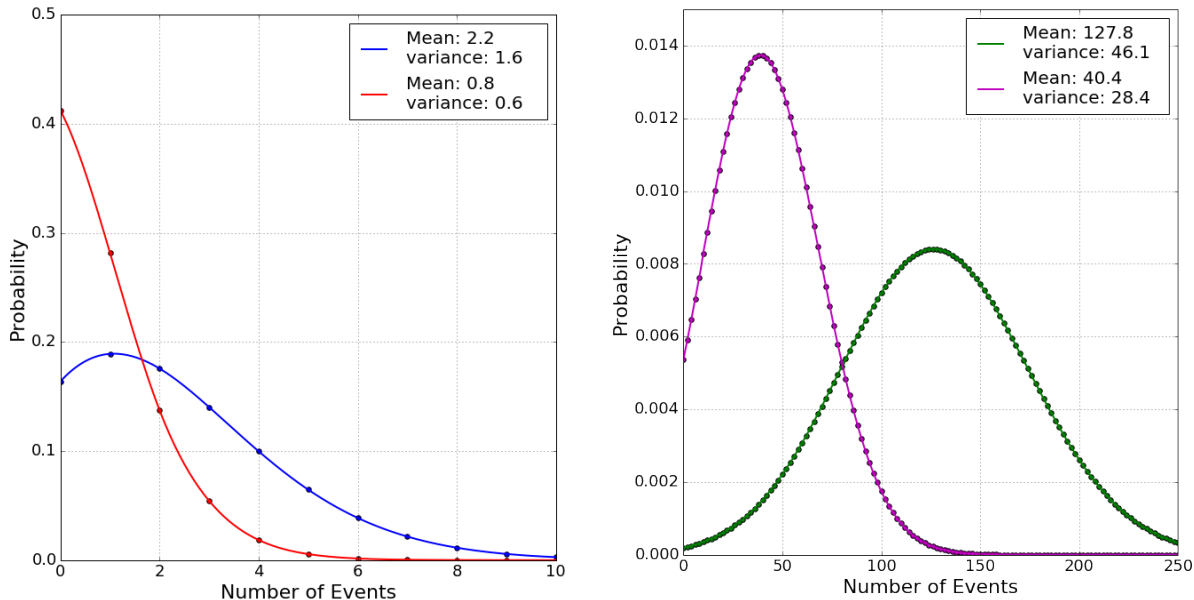


Figure 8.34: *Left:* Illustration of probability density function using Eq. 8.16 of two expected background rates with their variance. *Right:* Similar PDFs for two expected signal rates.

Implementing the uncertainties in the upper limit

Using Eq. 8.12, we are able to determine an upper limit in the scenario where we cannot claim detection. Because there are large uncertainties in both the background and signal rates, these uncertainties are included in the computation of the limit. The *observed* limit will be weighted with an uncertainty probability. Additionally, we will also show systematic uncertainty bands as can be seen in Figures 8.35 to 8.38.

Gaussian distributions with large uncertainties overlap with negative rates, which are not physical (i.e. expected rate of 2 events with a 150% uncertainty would yield a range of $[-1, +5]$. A rate of -1 is unphysical.), therefore we assume that the uncertainties follow a truncated normal distribution

$$\Phi(n_{\text{obs}}, n_{\text{bkg}}, \sigma_{\text{bkg}}, n_s, \sigma_s)_{90\%} = \Phi \cdot \frac{\sum_{n'_{\text{bkg}}=0}^{\infty} \left[\mu_{90}(n_{\text{obs}}, n'_{\text{bkg}}) \cdot P_{\text{unc}}(n'_{\text{bkg}} | n_{\text{bkg}}, \sigma_{\text{bkg}}) \right]}{\sum_{n'_s=0}^{\infty} n'_s \cdot P_{\text{unc}}(n'_s | n_s, \sigma_s)}, \quad (8.15)$$

where

$$P_{\text{unc}}(n | \lambda, \sigma) = \int_{-\lambda}^{\infty} \frac{(\lambda + x)^n e^{-\lambda - x}}{n!} \cdot w(x, \sigma) dx, \quad (8.16)$$

with $w(x, \sigma)$ a normal distribution with mean 0 and variance σ^2 . An example of two distributions for both the signal and background are shown in Figure 8.34. We can see that large rates with large uncertainties lead to Gaussian distributions (right figure). If a part of the distribution extends to negative rates, the formula (Eq. 8.16) removes these negative rates and scales the probabilities accordingly. Therefore, the total integrated probability is always one. Very low rates with relatively large uncertainties give much larger probabilities to very low number of events (left figure). Negative numbers are again removed.

8.5 Results

8.5.1 Unblinding

This analysis was presented to the collaboration after internal review and accepted for *data unblinding**. As explained in Section 6.6, only 10% of the data was used in setting up the analysis. Expected rates, e.g. in Table 8.5, are normalized to the total livetime of the full dataset. The total livetime for the different years is equal to

- 333.1 days of livetime for IC86-1,
- 324.5 days of livetime for IC86-2,
- 345.5 days of livetime for IC86-3,
- 357.3 days of livetime for IC86-4,
- 362.6 days of livetime for IC86-5,

resulting in a total livetime of 1723 days.

The cuts in the BDT score for each signal point were fixed by computing the most stringent upper limit with the model rejection factor using pull-validation. The full dataset is run through one BDT since an average of multiple BDTs could result in a systematic offset that is non-physical and would result in data events that contribute with a factor < 1 which is prone to lead to confusion. Therefore, one BDT out of 200 was chosen ad random for each signal point.

Before unblinding, a procedure was set for the following steps depending on the outcome

- If the number of seen data events are consistent with the expected background rate, an upper limit on the SMP flux is set as described in Section 8.4.3.
- If there is a consistent overfluctuation of the data compared to the expected background, a more in-depth analysis on these events should be performed before signal discovery can be claimed.

8.5.2 Limits

After unblinding, the number of data events for all signal points were consistent with the expected background, as can be seen in Table 8.9. The upper limits were computed with Eq. 8.15.

Event views of the types of these events can be found in Appendix E.

The resulting upper limits are shown in Figures 8.35 to 8.38 and compared to the experiments that were discussed in Chapter 2. The limits from this analysis were computed with Eq. 8.15 and are more stringent than any other experiment that was done up to now. Also shown are the upper limits for the individual charges with the large systematical error bands. Previous experiments did not present any uncertainties and could therefore not be shown in the figure.

There is an apparent optimum for discriminating SMPs from backgrounds in the IceCube experiment at a charge of 1/2. Particles with a higher charge (such as 2/3) resemble physical muons a lot more, while particles with a lower charge have a lot lower probability in producing enough light to trigger the detector.

In these figures, the obtained limits are compared to older experiments that used simplistic models for possible signatures of particles with an anomalous charge and assumed near 100% detector efficiencies. Even though the trigger and filter efficiencies (which were never optimized for these particles) are very low, the instrumented volume of the IceCube detector is orders of magnitude larger than those experiments. Therefore, it was possible to significantly improve the limits.

*By only looking at part of the data, the analyzer “blinds” himself to not (sub-)consciously tweak the analysis [239]. After approval, the analyzer can “unblind” and look at the full data, which serves as an objective way to look at the data and provides for consistency check with the expected and seen rates.

Table 8.9: Final results of the upper limit computations. For the signal, we show the expected rate from a $10^{-14} \text{ cm}^{-2} \text{s}^{-1} \text{sr}^{-1}$ flux and both background and signal are normalized to the total livetime of the full dataset.

Mass	Charge	Remaining MC signal events per 1723 days	Remaining MC background events per 1723 days	Seen events in data	$\bar{\mu}_{90} (\text{cm}^{-2} \text{s}^{-1} \text{sr}^{-1}) \times 10^{-16}$	$\mu_{90} (\text{cm}^{-2} \text{s}^{-1} \text{sr}^{-1})$
10 GeV	1/2	73.2 ± 48.5	$2.2^{+3.5}_{-2.2}$	0	$5.0^{+41.5}_{-4.4}$	$1.4 \cdot 10^{-16}$
100 GeV		121.3 ± 75.7	$2.2^{+4.4}_{-2.2}$	0	$3.0^{+24.5}_{-2.6}$	$8.1 \cdot 10^{-17}$
1 TeV		90.7 ± 46.1	$0.8^{+1.3}_{-0.8}$	0	$1.9^{+11.4}_{-1.1}$	$1.6 \cdot 10^{-16}$
10 TeV		127.8 ± 59.0	$1.8^{+3.0}_{-1.8}$	2	$2.1^{+12.4}_{-1.8}$	$2.5 \cdot 10^{-16}$
100 TeV		107.7 ± 64.2	$2.2^{+4.4}_{-2.2}$	0	$3.4^{+25.4}_{-2.96}$	$9.1 \cdot 10^{-17}$
10 GeV	1/3	45.3 ± 24.9	$2.2^{+4.6}_{-2.2}$	6	$8.2^{+53.1}_{-7.2}$	$1.5 \cdot 10^{-15}$
100 GeV		60.5 ± 29.9	$2.4^{+4.7}_{-2.4}$	5	$5.9^{+35.0}_{-5.2}$	$9.2 \cdot 10^{-16}$
1 TeV		64.0 ± 35.4	$3.1^{+6.5}_{-3.1}$	4	$6.7^{+50.7}_{-6.0}$	$5.8 \cdot 10^{-16}$
10 TeV		57.6 ± 31.8	$1.2^{+2.4}_{-1.2}$	5	$5.5^{+27.8}_{-4.8}$	$1.3 \cdot 10^{-15}$
100 TeV		79.7 ± 40.9	$2.2^{+4.3}_{-2.2}$	6	$4.6^{+27.7}_{-3.9}$	$8.9 \cdot 10^{-16}$
10 GeV	2/3	40.4 ± 28.4	$9.6^{+14.4}_{-9.6}$	9	$14.2^{+240}_{-1.3}$	$1.2 \cdot 10^{-15}$
100 GeV		71.5 ± 48.8	$5.0^{+6.4}_{-5.0}$	2	$5.1^{+71.7}_{-4.40}$	$2.7 \cdot 10^{-16}$
1 TeV		79.3 ± 60.0	$7.2^{+9.4}_{-7.2}$	9	$6.7^{+118}_{-6.1}$	$7.7 \cdot 10^{-16}$
10 TeV		74.4 ± 62.7	$7.9^{+10.3}_{-7.9}$	5	$6.3^{+210}_{-5.8}$	$3.9 \cdot 10^{-16}$
100 TeV		59.0 ± 36.4	$5.7^{+7.3}_{-5.7}$	1	$7.4^{+79.1}_{-6.7}$	$2.2 \cdot 10^{-16}$

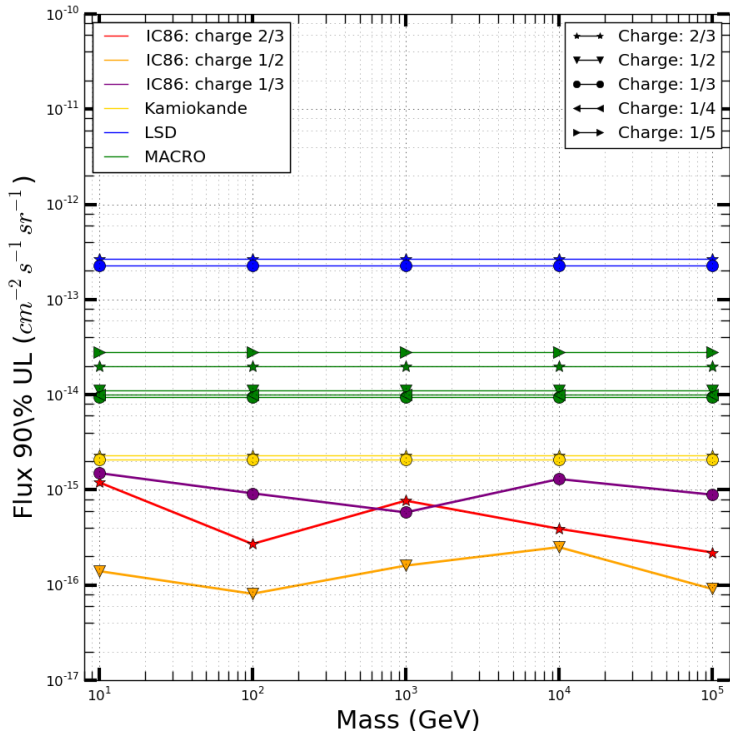


Figure 8.35: Final upper limits for SMPs with three different charges as a function of the mass. Previous experiments did not include a mass dependence and are therefore shown as straight lines.

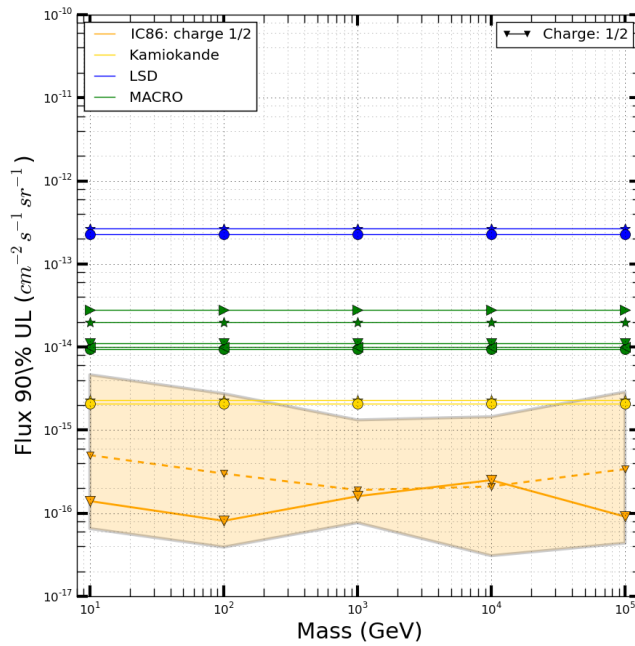


Figure 8.36: Comparison of other experiments to the upper limit obtained for SMPs with a charge 1/2 including the systematic error bands. The observed limit is shown with a solid line and the expected limit is shown with a dashed line. Other experiments did not have a mass dependence in the analysis and are therefore shown as straight lines.

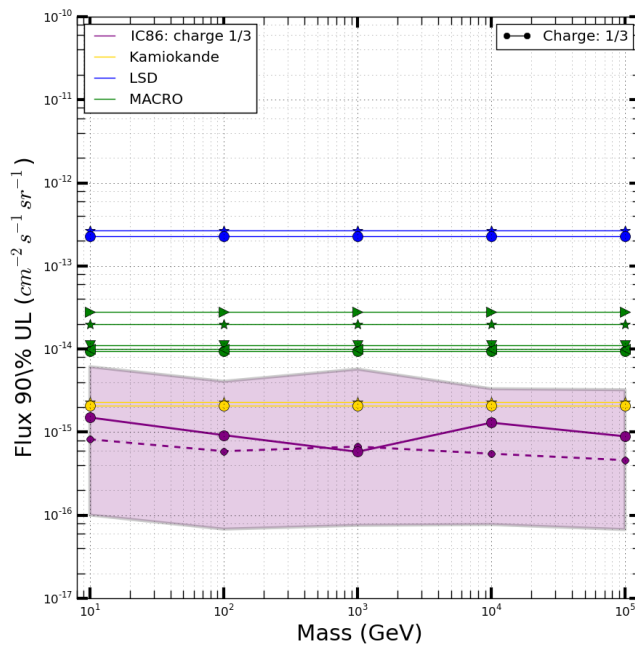


Figure 8.37: Comparison of other experiments to the upper limit obtained for SMPs with charge 1/3 including the systematic error bands. The observed limit is shown with a solid line and the expected limit is shown with a dashed line. Other experiments did not have a mass dependence in the analysis and are therefore shown as straight lines.

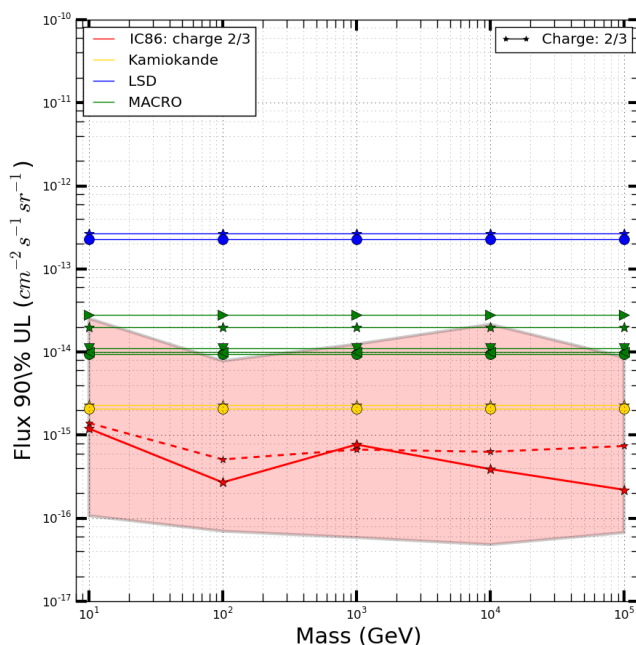


Figure 8.38: Comparison of other experiments to the upper limit obtained for SMPs with charge 2/3 including the systematic error bands. The observed limit is shown with a solid line and the expected limit is shown with a dashed line. Other experiments did not have a mass dependence in the analysis and are therefore shown as straight lines.



9. Summary and Conclusion

In this work a search for particles with an anomalous charge is obtained. These particles would have an electric charge lower than one, relative to the electron charge. The charges under investigation are $1/2$, $1/3$ and $2/3$, the masses assumed range from 10 GeV to 100 TeV, giving a total of 15 signal points. Due to the difference in charge, these particles produce less Cherenkov light as compared to muons.

Because these particles can have different signatures in the IceCube detector compared to known particles, it is possible to perform a search. Detecting these particles would provide a gateway to extensions of the Standard Model. There exists a plethora of possible models to include new physics, where the existence of particles with an anomalous charge would provide an indication of what model would be more feasible than others.

The particles were assumed to be isotropic in direction and follow an E^{-2} spectrum. The simulations were done by using the modules that are used to simulate muon interactions and changing the mass and charge in the cross-sections that are implemented in the code. Photon production, with the use of GPU intensive models, is scaled with the charge as predicted by the Frank-Tamm equation for Cherenkov photon production.

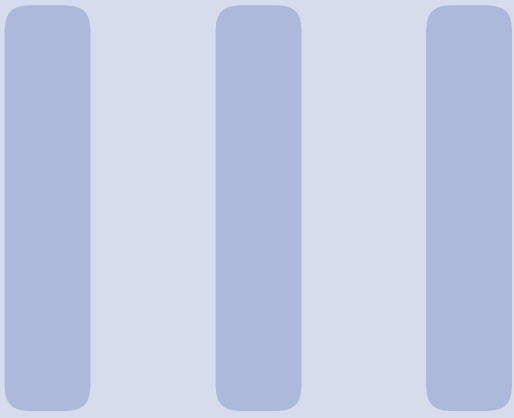
The analysis starts from data obtained from PnF from the IceCube detector that was gathered in the years 2011 to 2015 and include a total of 1723 days of livetime. The large amount of data is first sent through a series of quality cuts and cleaning algorithms. A resampling technique called pull-validation was used to handle the lack of statistics at the final level using a boosted decision tree.

We can conclude from this work that the number of data events is in agreement with the number of expected backgrounds, and therefore an upper limit on the flux of particles with an anomalous charge was determined. The observed limits are up to an order of magnitude more stringent than older experiments although a direct comparison is not well supported. All experiments set limits to a flux close to the detector, but do not include effects such as the shielding of rock or ice around the detector. Therefore, there is a need for better theoretical models that predict fluxes at the set detector locations.

Other possible improvements of the analysis should mainly focus on the triggering and filtering ef-

ficiencies of these very dim particles. Dedicated triggers and filters that do not exist for now could potentially make the limits an order of magnitude more stringent (or more), but are also expected to include more noise effects so that a proper estimate is not possible. In this analysis, boosted decision trees were used, but the last couple of years there have been many advances in other machine learning techniques, which could provide potential enhancements. Other possible improvements could come with the IceCube Upgrade and even IceCube-Gen2, but the former seems very small in instrumented volume to make use of the long tracks that are expected and the latter is even more coarsely spaced so that dim tracks will be almost indistinguishable from noise effects.

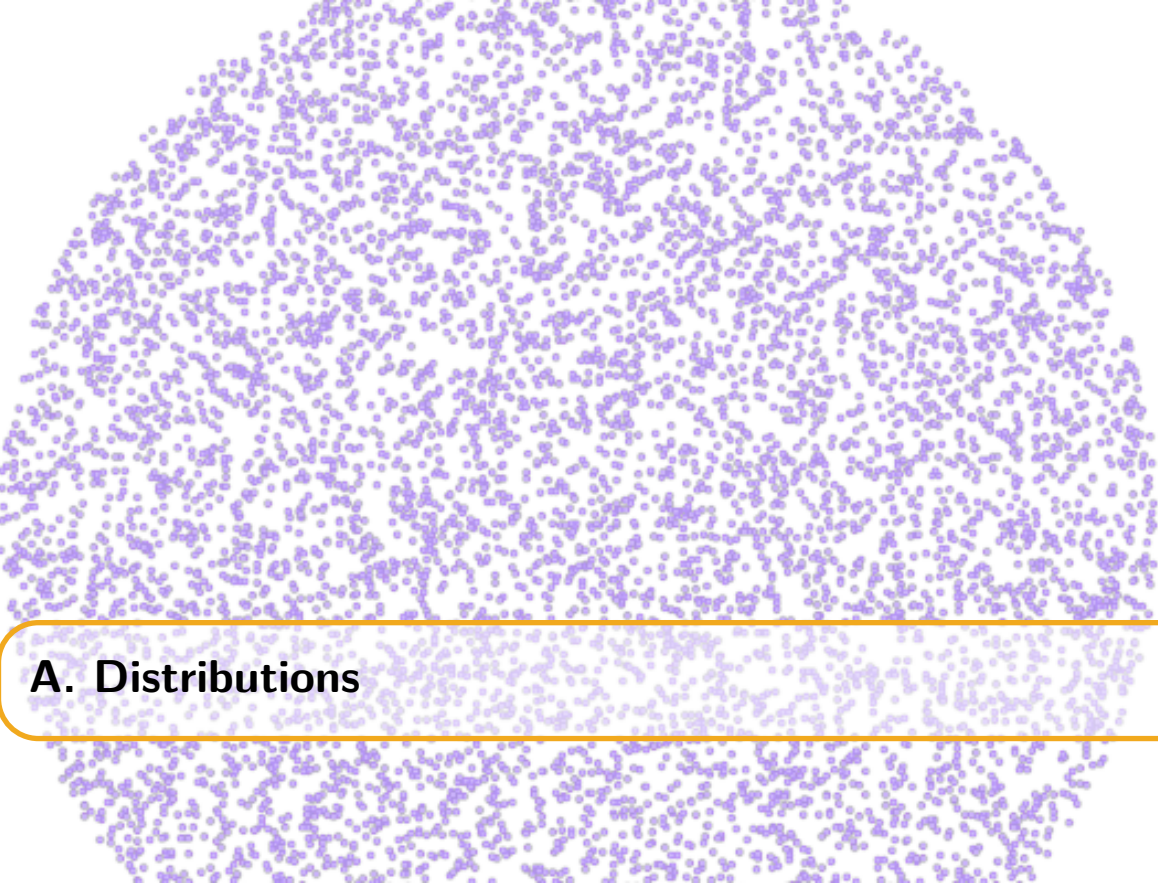
Anomalously charged particles remain undetected; the search for new physics is to be continued.



Additions

Appendices	161
A Distributions	163
A.1 Spherical random numbers	
A.2 Power law distributions	
A.3 Angular distributions	
A.4 Weighting	
B Boosted Decision Trees: examples	169
B.1 Decision Tree: simple example	
B.2 AdaBoost: simple example	
C Resampling Methods	173
C.1 Bootstrapping	
C.2 Cross-validation	
D Additional BDT Checks	175
E Data Events at Final Level	177
Bibliography	181

Appendices



A. Distributions

A.1 Spherical random numbers

Most random number generators provide uniform distributions between the range $[0, 1]$. Assume we want to make a uniform distribution along a sphere with angles ϕ and θ and radius r , in spherical coordinates. Random numbers between $[0, \pi]$, $[0, 2\pi]$ and $[0, R]$ (the ranges of the coordinates) would not give a uniform distribution as illustrated in Figure A.1 (left). The differential surface area, dA , is equal to $dA(d\phi, d\theta) = r^2 \sin(\phi) d\phi d\theta$. If we want the distribution $f(v)$ to be constant for a uniform distribution, then $f(v) = \frac{1}{4\pi}$ since $\int \int_S f(v) dA = 1$ and $\int \int_S dA = 4\pi$. We want the distribution in function of the angles, so

$$f(v)dA = \frac{1}{4\pi}dA = f(r)f(\phi, \theta)d\phi d\theta. \quad (\text{A.1})$$

Since we know the expression for dA , we find that

$$f(\phi, \theta) = \frac{1}{4\pi} \sin(\phi), \quad (\text{A.2})$$

and separating the angles:

$$f(\theta) = \int_0^\pi f(\phi, \theta) d\phi = \frac{1}{2\pi}, \quad (\text{A.3})$$

$$f(\phi) = \int_0^{2\pi} f(\phi, \theta) d\theta = \frac{\sin(\phi)}{2}, \quad (\text{A.4})$$

where it is clear that $f(\phi)$ scales with $\sin(\phi)$; there are more points needed at the equator (this makes sense, as the surface at the equator is much larger!).

The question is now how one can get a sample to follow the distribution of $f(\phi)$. For this, we use the *inverse transform sampling* method where one makes use of the cumulative distribution function, $F(\phi)$, which increases monotonically

$$F(\phi) = \int_0^\phi f(\phi') d\phi' = \frac{1}{2} (1 - \cos(\phi)). \quad (\text{A.5})$$

The method shows that if u is a random variable drawn from a uniform distribution, we have to find the inverse function of F ,

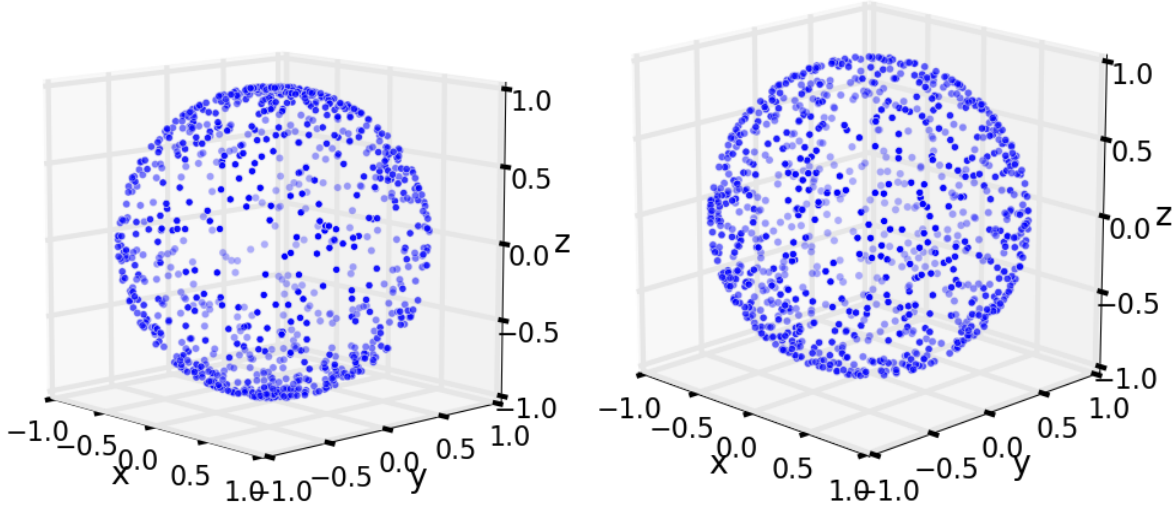


Figure A.1: *Left:* Illustration of a uniform sampling in angles ϕ and θ that doesn't give a uniform spherical distribution. *Right:* Illustration of a good spherical distribution.

$$F(F^{-1}(u)) = u \quad (\text{A.6})$$

$$\frac{1}{2} (1 - \cos(F^{-1}(u))) = u \quad (\text{A.7})$$

$$F^{-1}(u) = \arccos(1 - 2u). \quad (\text{A.8})$$

In other words: if u is a random variable drawn from a uniform distribution, then $\phi = \arccos(1 - 2u)$ follows a distribution necessary for a uniform spherical distribution. Similarly, $\theta = \frac{1}{2\pi}u$.

A.2 Power law distributions

Analogous to what was written in the previous section, one can produce a power law distribution from random numbers using the inverse transform sampling method:

$$\begin{aligned} f(E) &= A \cdot E^{-\gamma} \quad (\text{powerlaw}) \\ F(E) &= \int_{E_{min}}^E A \cdot E^{-\gamma} dE = u \quad (\text{inverse sampling, } u \text{ random number } [0,1]) \\ &= A \left[\frac{E^{-\gamma+1}}{-\gamma + 1} \right]_{E_{min}}^E \\ &= \frac{A}{-\gamma + 1} (E^{-\gamma+1} - E_{min}^{-\gamma+1}) \end{aligned} \quad (\text{A.9})$$

Because we know that $F(F^{-1}(u)) = u$, we can find an expression for $F^{-1}(u)$:

$$\begin{aligned} u &= \frac{A}{-\gamma + 1} \left((F^{-1}(u))^{-\gamma+1} - E_{min}^{-\gamma+1} \right) \\ &\Rightarrow \end{aligned} \quad (\text{A.10})$$

$$F^{-1}(u) = \left(\left(\frac{-\gamma + 1}{A} \cdot u \right) + E_{min}^{-\gamma+1} \right)^{1/(-\gamma+1)}$$

To find A , we use the property of a CDF:

$$F(E_{max}) = 1 \Rightarrow A = \frac{-\gamma + 1}{E_{max}^{-\gamma+1} - E_{min}^{-\gamma+1}}, \quad (\text{A.11})$$

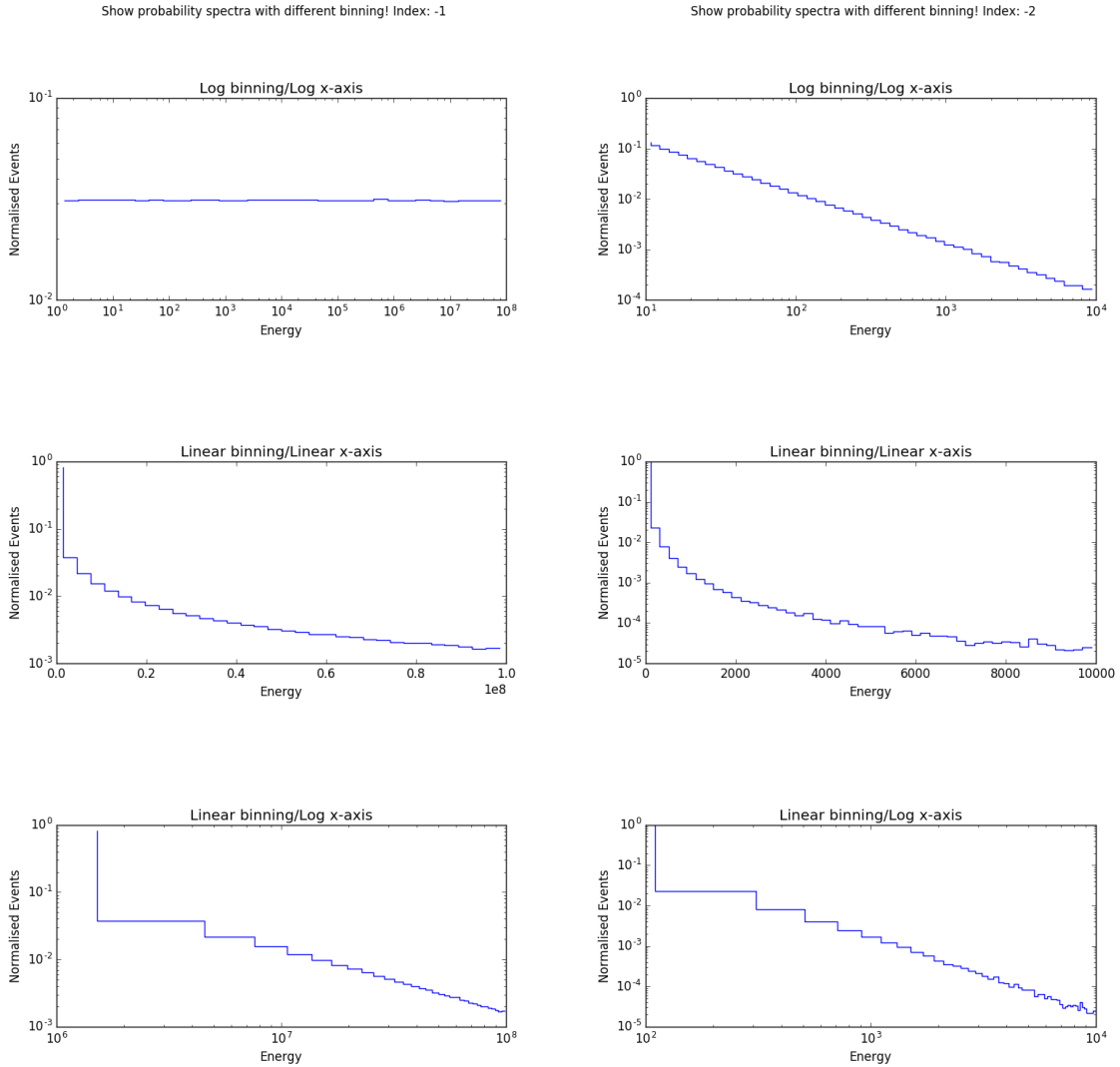


Figure A.2: *Left:* Histograms with different binnings showing the behavior of an energy spectrum with spectral index -1. *Right:* Histograms with different binnings showing the behavior of an energy spectrum with spectral index -2.

leading to

$$F^{-1}(u) = \left((1-u) \cdot E_{min}^{-\gamma+1} + u \cdot E_{max}^{-\gamma+1} \right)^{1/(-\gamma+1)}, \quad (\text{A.12})$$

which shows how one can draw a distribution in function of E following $f(E)$ with a uniform random number u .

For $\gamma = -1$, the computations are analogous and one can see that this will produce a uniform distribution in log space. This is shown in Figure A.2.

$$\begin{aligned} E &= E_{min} \cdot 10^{u \cdot \log \frac{E_{max}}{E_{min}}} \\ &= 10^{u[\log E_{min}, \log E_{max}]} \end{aligned} \quad (\text{A.13})$$

In Figure A.3 the signal reweighting is shown.

A.3 Angular distributions

As seen in Section A.1, the differential space angle $d\Omega$ is equal to

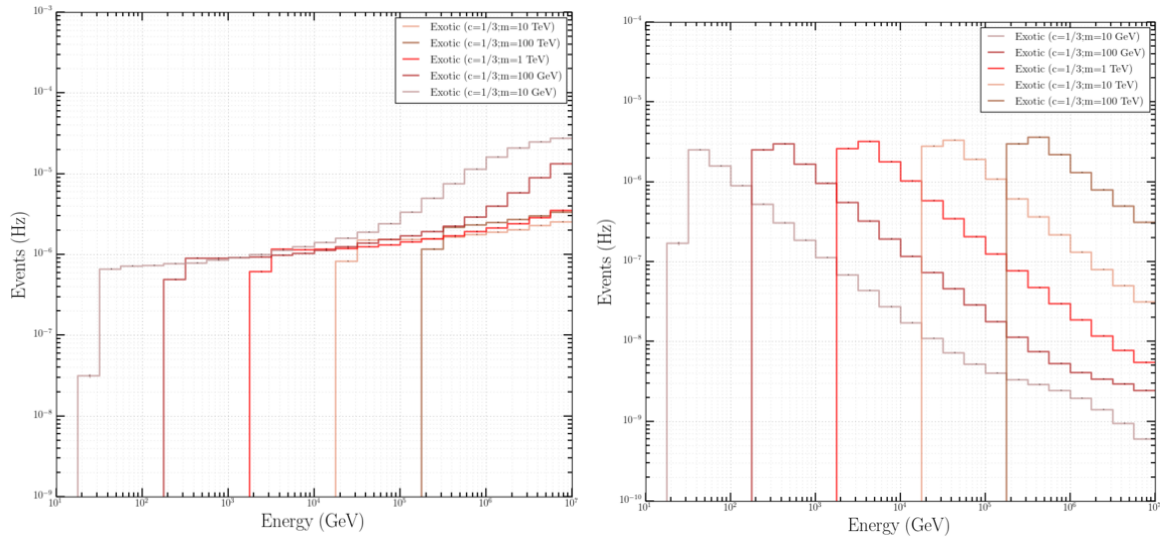


Figure A.3: *Left:* Spectrum of the signal before weighting following an E^{-1} spectrum. The rise in the rate in function of energy is due to the trigger efficiency that increases in function of energy. *Right:* Spectrum of the signal after reweighting to an energy spectrum of $E-2$.

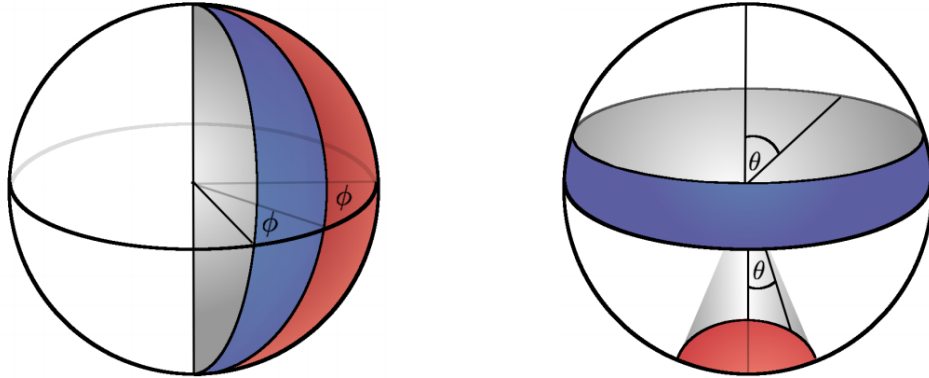


Figure A.4: Illustration of angle distributions in spherical coordinates. The blue and red surfaces are equal in size. The left figure clearly shows the surface to be proportional to the azimuth. The right figure shows how there is a non-trivial dependence on the zenith angle for equal partitions on the surface of a sphere.

$$d\Omega = \sin(\theta)d\theta d\phi. \quad (\text{A.14})$$

If one shows the distribution of ϕ and/or θ , then this is the same as showing partial integrations per bin. We find that

$$\Omega \propto \cos(\theta), \quad (\text{A.15})$$

or in other words: the space angle is proportional to the azimuth and the cosine of the zenith. An example is shown in Figure A.4.

A.4 Weighting

A method that is often used in simulations is *weighting*. The simulated and expected differential flux of particles is often not the same, mainly due to two reasons:

- The flux has no uniform power law behavior. As can be seen in Figure 3.2, there can be multiple “kinks” and changes in a spectrum. Instead of simulating the flux according to

one model, a general uniform flux is used and later reweighted to be able to fit to other models more easily.

- A steep power law indicates very few events at the highest energy bins. This means large CPU time would be necessary to simulate these events. As an example, let us assume two different fluxes

$$f_1 = A \cdot x^{-1}, \quad (\text{A.16})$$

$$f_2 = B \cdot x^{-2}, \quad (\text{A.17})$$

where $A = 10^3$ and $B = 10^4$, so the fluxes cross at a value of $x^{-1+2} = x = \frac{10^4}{10^3} = 10$. In the interval $x \in [10^3, 10^4]$, the number of events for f_1 is equal to 10^3 , whereas for f_2 this is equal to 9.

Simulating with harder spectra* leads to more statistics in high-energy bins.

The weights can be generally written down as

$$w = \frac{dN_{exp}}{dAd\Omega dEdt} \times \frac{dAd\Omega dE}{dN_{sim}}. \quad (\text{A.18})$$

A disadvantage of using weights is that certain events with a high weight are rare but can dominate or obscure the sample in the tails of certain distributions.

*Harder spectra equals to a lower gamma, since there will be more high-energy events.



B. Boosted Decision Trees: examples

B.1 Decision Tree: simple example

Let us assume we want to categorize 6 people if they are *healthy* or *unhealthy*. The decision tree training can be done if we have a sample set that labels people in these two categories and some other information about these persons is known. In this example, we know if the person is older than 30, if he eats a lot of pizza and if he exercises a lot. This is summarized in Table B.1.

As an example, we can show how the first child nodes are determined. The sample set has three variables and the variable selection that allows for the largest separation (see Eq. 7.23) will be chosen. The results from ΔS for the age, pizza and exercises selections are 0, -1.7 and -2.6 respectively. Therefore, it should be clear that the age selection should be chosen first in the decision tree as it gives the largest separation for the child nodes. Deeper child nodes are selected in a similar fashion.

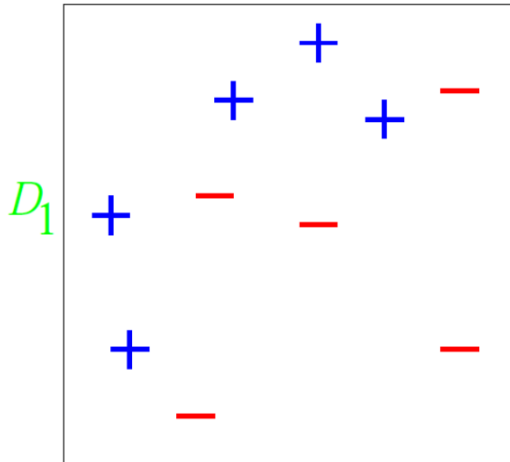
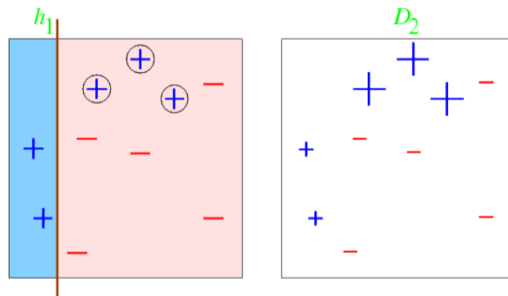
B.2 AdaBoost: simple example

Consider a binary decision tree classification with 10 training examples. The illustrations below are 2D variable distributions.

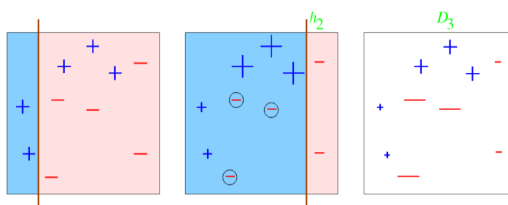
We give each event an equal weight, making the weight distribution D_1 uniform. For this simple example, each of our classifiers will be an axis-parallel linear classifier (simple cut in one of the two variables).

Table B.1: Summary of dataset used to train decision tree.

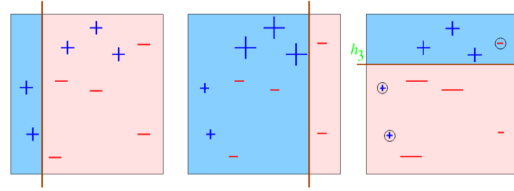
Person	Age <30	Eats lots of pizza	Exercises often	Healthy
A	1	1	1	0
B	1	0	1	1
C	1	0	0	1
D	0	0	0	0
E	0	0	1	1
F	0	0	1	1

Initial distribution**Round 1**

- Error rate of h_1 : $\epsilon_1 = 0.3$; weight of h_1 (see Eq. 7.25): $\alpha_1 = \frac{1}{2} \ln \left(\frac{1-\epsilon_1}{\epsilon_1} \right) = 0.42$
- An event that is misclassified gets a higher weight: weight multiplied with $\exp(\alpha_1)$
- An event that is correctly classified gets a lower weight: weight multiplied with $\exp(-\alpha_1)$

Round 2

- Error rate of h_1 : $\epsilon_1 = 0.21$; weight of h_2 (see Eq. 7.25): $\alpha_2 = \frac{1}{2} \ln \left(\frac{1-\epsilon_2}{\epsilon_2} \right) = 0.65$
- An event that is misclassified gets a higher weight: weight multiplied with $\exp(\alpha_2)$
- An event that is correctly classified gets a lower weight: weight multiplied with $\exp(-\alpha_2)$

Round 3

The error rate of h_1 : $\epsilon_1 = 0.21$; weight of h_2 (see Eq. 7.25): $\alpha_2 = \frac{1}{2} \ln \left(\frac{1-\epsilon_2}{\epsilon_2} \right) = 0.65$

Let us suppose to stop after this round, we now have a forest of 3 decision classifiers: h_1, h_2, h_3 .

Final step

The final classifier is a weighted linear combination of all the classifiers:

$$H_{\text{final}} = \text{sign} \left(0.42 \begin{array}{|c|} \hline \text{blue} \\ \hline \end{array} + 0.65 \begin{array}{|c|} \hline \text{blue} \\ \hline \end{array} + 0.92 \begin{array}{|c|} \hline \text{blue} \\ \hline \end{array} \right)$$

=

C. Resampling Methods

Resampling is a method used in statistical analyses and commonly refers to methods that extract information from a larger set by taking subsets and performing significance or validation tests. Two common examples are *bootstrapping* and *cross-validation* and are explained below.

C.1 Bootstrapping

The basic idea of bootstrapping is that we can draw conclusions from a certain sample in a larger, unknown, population by taking a subsample and performing inference about the sample from the subsample. The method assumes that the true probability distribution from a sample to a population can be reasonably estimated from an empirical probability distribution from a subsample to a sample.

Assume we have a total population P of size N_P and a measured sample N of size N_N , where

$$N_N < N_P \text{ and } N \subset P. \quad (\text{C.1})$$

From N , only one estimate of the mean can be computed. To get a sense of the variability one could assume a Gaussian or Poissonian probability, or what is done in this method: form a new subsample that is also of size N_N . This can only be done by *sampling with replacement* where the elements in the subsample can be repeated. If N_N is sufficiently large, this will almost certainly result in subsamples that are different from the original sample. The mean can be computed from the new subsample and this process is repeated a large number of times (typically of the order of 1,000). The distribution of the means then indicates our confidence in the sample mean where a large variability assumes large uncertainties.

C.2 Cross-validation

Another example of a resampling method is cross-validation, sometimes called *rotation estimation*, where one wants to estimate the predictive power of a model. From a sample, a subsample called the *training sample* is selected to train a model (e.g. a BDT). This model is then checked on another subsample called the *testing sample*. This allows to estimate how the model will generalize to other independent datasets. Training samples will often have a lower performance in parameter estimations from the testing sample than the training sample. In cross-validation

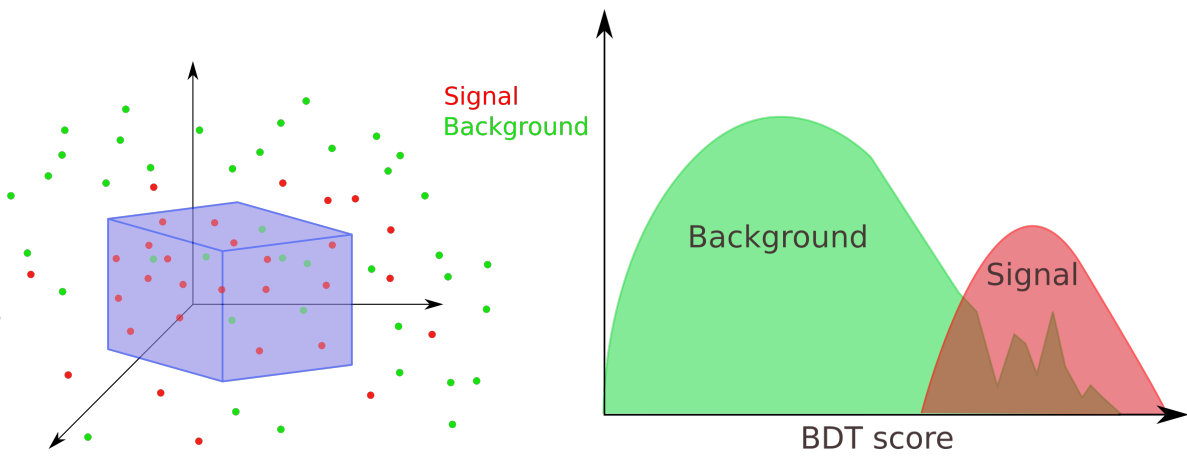


Figure C.1: Simplistic illustration of parameter space that originates from one branch in one BDT. The axes represent physical parameters that are used in the BDT. The blue box illustrates an example of cuts that are placed on the parameters. The BDT algorithm converts the survival probability of an event regarding these cuts into a score. Limited statistics for the background events are represented by a discontinuous tail.

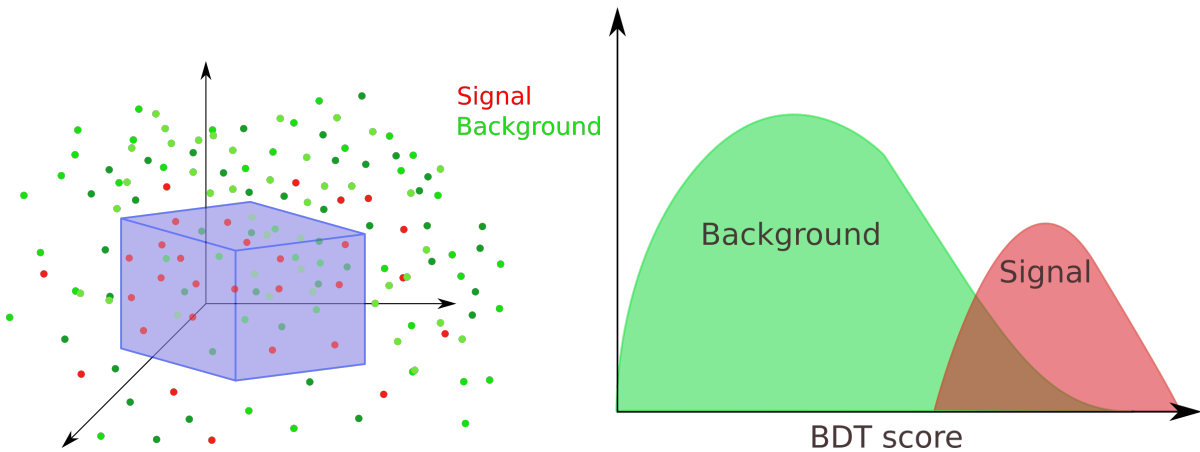


Figure C.2: Simplistic illustration of parameter space that originates from one branch in one BDT. Resampling the background (different green points) results in more statistics in the tail.

one tries to get an estimate for this effect. An often used cross-validation method is called *k-fold cross-validation*.

In this method, one iterates the procedure of selecting a training sample and a testing sample k times. If the total size of the sample set is N_N , the testing samples will have a size of N_N/k . As we have k iterations, the subsamples can be chosen without replacement and are unique each time. At each iteration, the training sample will have a size of $N_N - \frac{N_N}{k} = N_N \cdot \frac{k-1}{k}$. The k results can then be averaged to produce a single estimation.

Pull-validation is another example of a resampling method and is explained in more detail in Section 8.4.2. Illustratively, it can be visualized as in Figs. C.1 and C.2.

D. Additional BDT Checks

As explained in Section 7.7, it is important to perform some checks to see if a BDT is performing normally. A first check is done to see if the distribution of the training and testing samples show significant differences. This is shown in Figure D.1 and explained in more detail in Section 7.7.4.

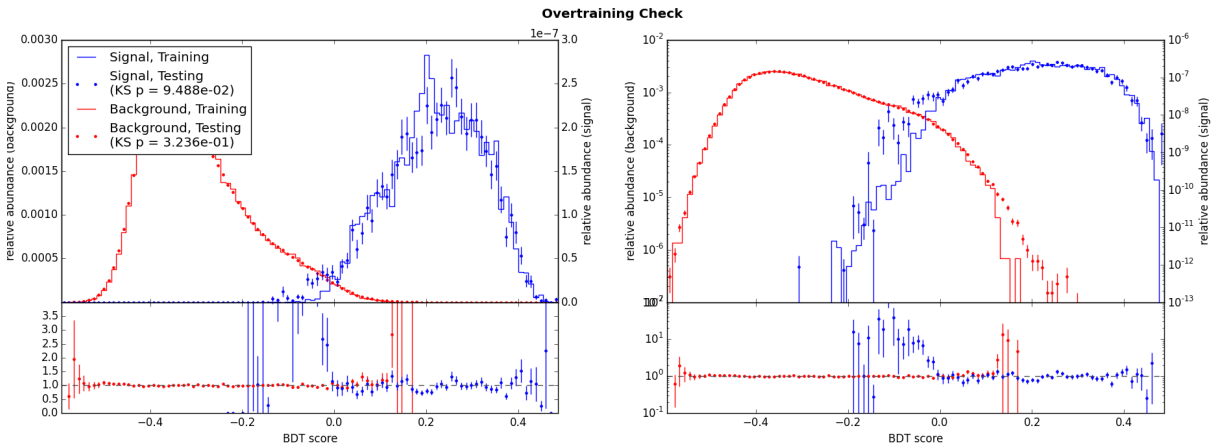


Figure D.1: No significant overtraining seems to be present in signal and background. The signal used here is an SMP of charge $\frac{1}{2}$ and mass 100 GeV.

The correlation between the 17 variables that were used in the BDT is shown in Figure D.2. These variables were selected with the mRMR feature, which shows an excellent performance since there are no significant correlations in both signal and background visible.

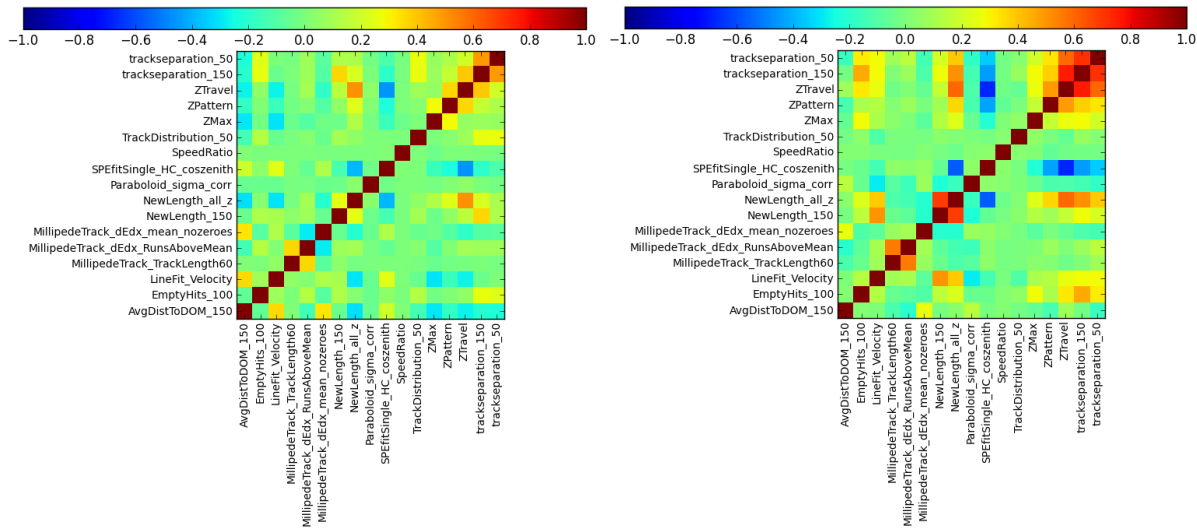


Figure D.2: Here we see the correlation between the variables that are used in the BDT. There is no significant correlation in *both* signal and background, making these variables appropriate to use.

E. Data Events at Final Level

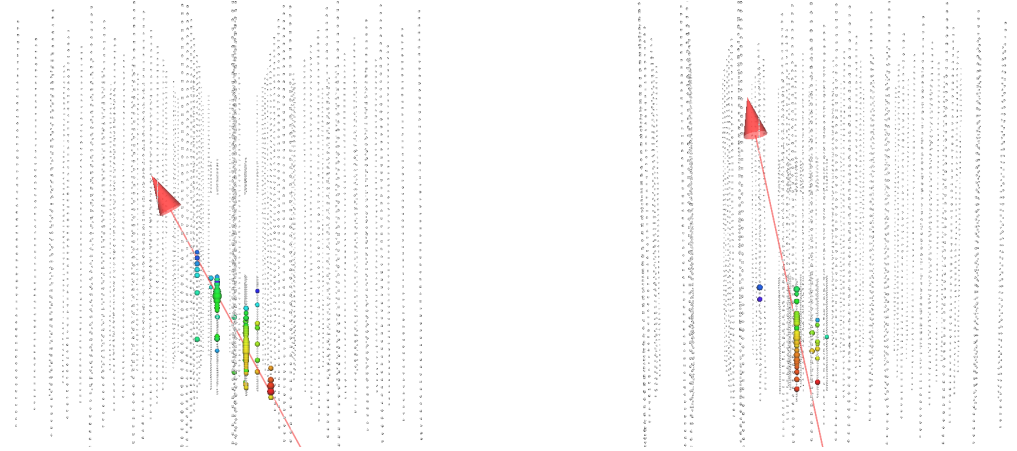


Figure E.1: Event viewers of an event that survive the SMP with mass 10 TeV and charge 1/2 selection. *Left (real data)*: Short and bright upgoing track corresponds to μ from an atmospheric ν_μ that stopped shortly after leaving DeepCore. *Right*: Simulated atmospheric ν_μ event that strongly resembles this data event.

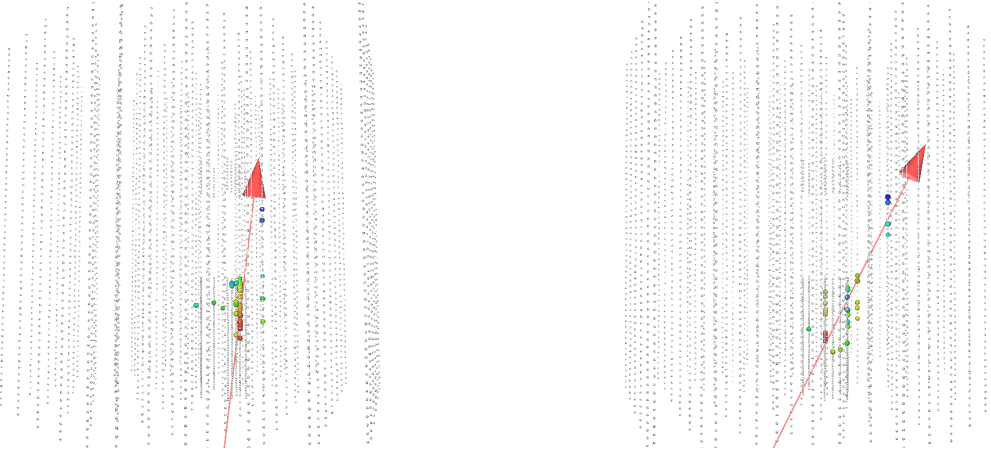


Figure E.2: Event viewers of an event that survive the SMP with mass 10 TeV and charge 1/2 selection. *Left (real data)*: Corresponds to an upgoing μ from atmospheric ν_μ that either starts or “corridors” in between strings and skims DeepCore along the side. After leaving DeepCore it only passes close to one string, giving the two hits. *Right*: Simulated atmospheric ν_μ event that strongly resembles this data event.

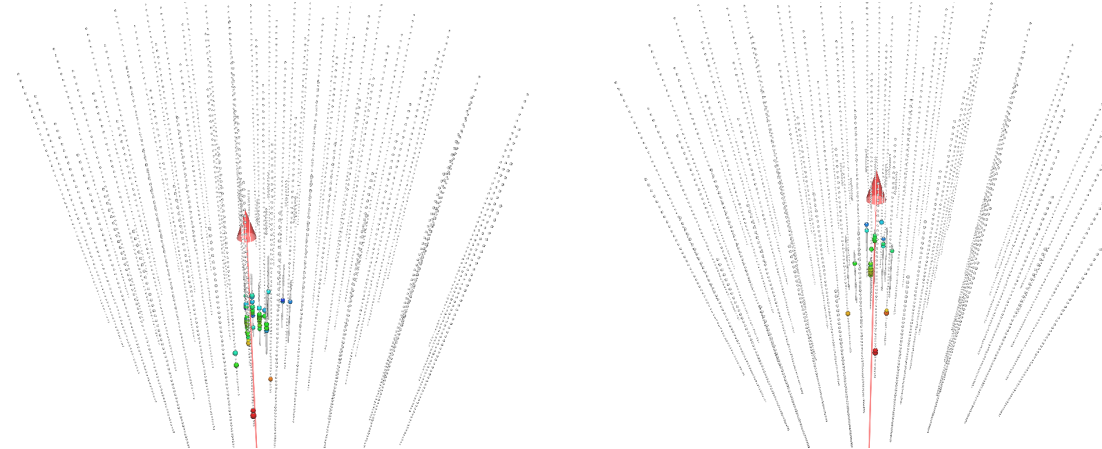


Figure E.3: Event viewers of an event that survive the SMP with mass 10 GeV and charge 1/3 selection. *Left (real data)*: Corresponds to a horizontal μ from atmospheric ν_μ that passes close to one string in IceCube and stops in DeepCore where more light is recorded. *Right*: Simulated atmospheric ν_μ event that strongly resembles this data event.

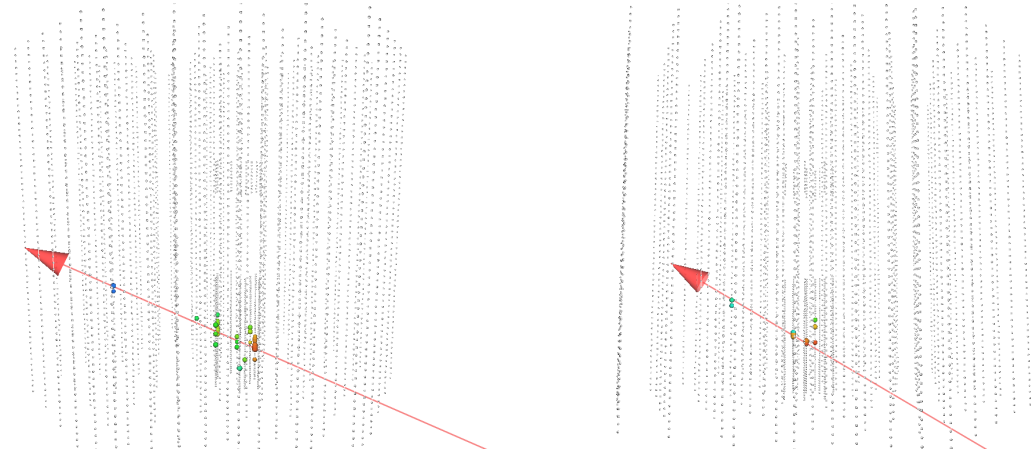


Figure E.4: *Left:* Typical simulated SMP of 100 GeV and charge 1/2 that survives the final selection. *Right:* Typical simulated SMP of 100 GeV and charge 1/3 that survives the final selection. Note that there is a lot less light produced compared to particles with higher charges.

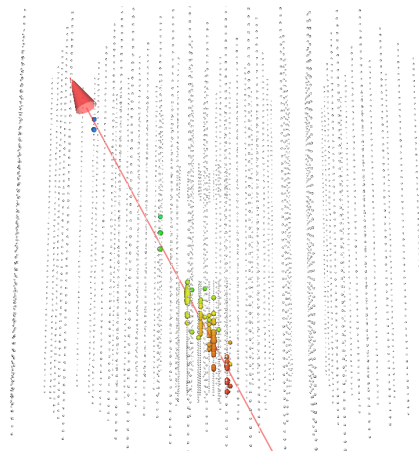
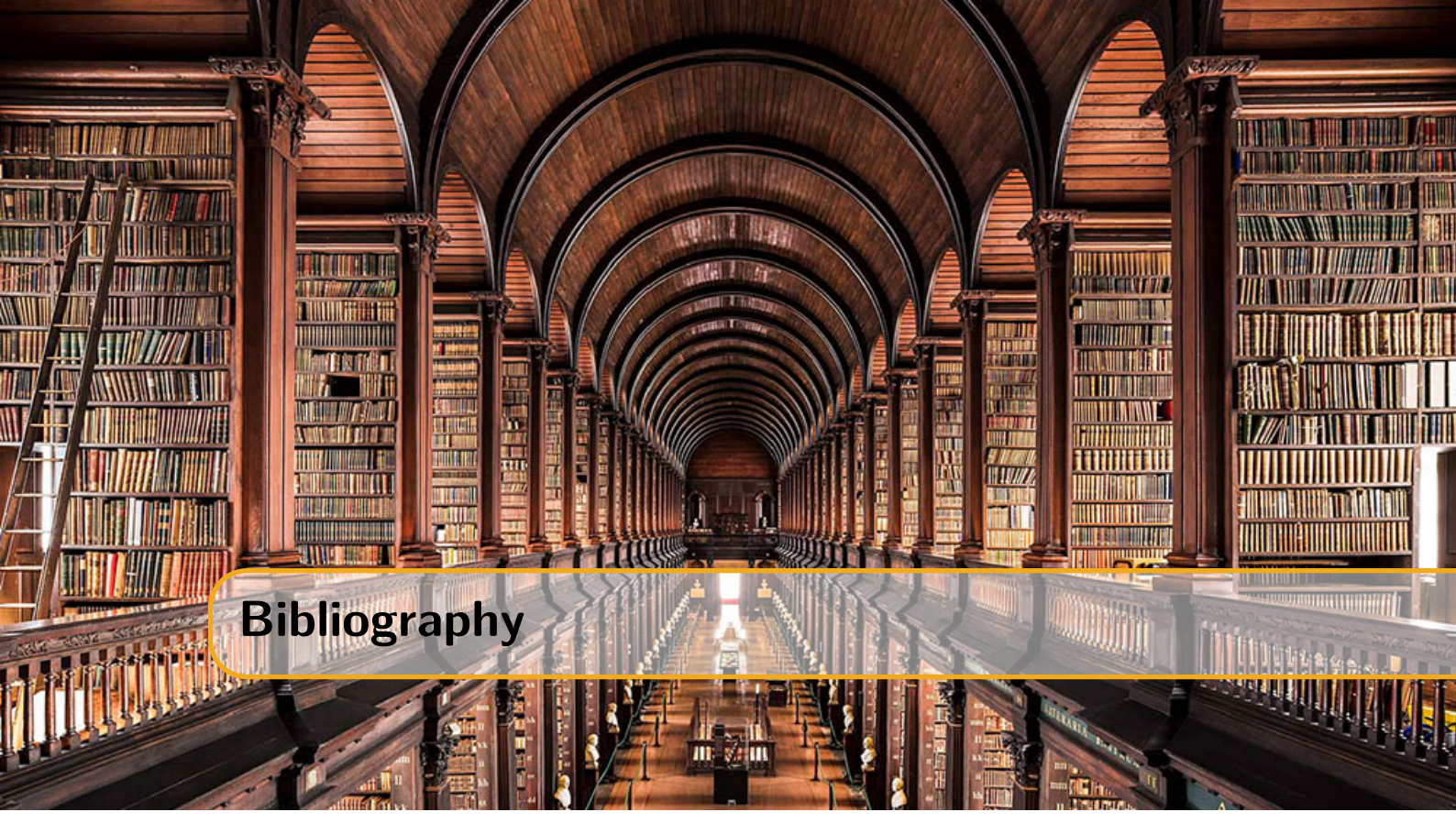


Figure E.5: Typical simulated SMP of 100 GeV and charge 1/3 that survives the final selection. Note that there is a lot more light produced compared to particles with lower charges.



Bibliography

- [1] B. Povh et al. *Particles and nuclei: An Introduction to the physical concepts*. 1995. DOI: 10.1007/3-540-36684-9 (cited on page 13).
- [2] Michael E. Peskin and Daniel V. Schroeder. *An Introduction to quantum field theory*. Reading, USA: Addison-Wesley, 1995. URL: <http://www.slac.stanford.edu/~mpeskin/QFT.html> (cited on page 13).
- [3] M. Tanabashi et al. “Review of Particle Physics”. In: *Phys. Rev. D* 98 (2018), page 030001 (cited on page 13).
- [4] Alessandro Bettini. *Introduction to elementary particle physics*. 2008. ISBN: 9780521880213. URL: <http://www.cambridge.org/catalogue/catalogue.asp?isbn=9780521880213> (cited on page 13).
- [5] CERN. URL: <https://home.cern/about/physics/standard-model> (cited on page 14).
- [6] Arthur B. McDonald. “Nobel Lecture: The Sudbury Neutrino Observatory: Observation of flavor change for solar neutrinos”. In: *Rev. Mod. Phys.* 88 (3 July 2016), page 030502. DOI: 10.1103/RevModPhys.88.030502. URL: <https://link.aps.org/doi/10.1103/RevModPhys.88.030502> (cited on page 15).
- [7] CMS. URL: <http://cms.web.cern.ch/news/jets-cms-and-determination-their-energy-scale> (cited on page 15).
- [8] URL: <http://hyperphysics.phy-astr.gsu.edu/hbase/Forces/couple.html#c1> (cited on page 16).
- [9] A. Kircher. *Athanassii Kircherii... Magnes, sive De arte magnetica opus tripartitum...* sumptibus H. Scheus, 1641. URL: <https://books.google.be/books?id=1aZ3FcTAYdUC> (cited on page 16).
- [10] G. Farmelo. *The Strangest Man: The Hidden Life of Paul Dirac, Mystic of the Atom*. Basic Books, 2009. ISBN: 9780465019922. URL: <https://books.google.be/books?id=qsodmIGDOfMC> (cited on page 17).
- [11] F. Mandl and G. Shaw. *Quantum Field Theory*. Wiley, 2013. ISBN: 9781118716656. URL: <https://books.google.be/books?id=jTBzQfctvHAC> (cited on page 18).
- [12] Flip Tanedo. URL: <https://www.quantumdiaries.org/2012/02/14/why-do-we-expect-a-higgs-boson-part-ii-unitarization-of-vector-boson-scattering/> (cited on page 21).

- [13] S. L. Glashow, J. Iliopoulos, and L. Maiani. “Weak Interactions with Lepton-Hadron Symmetry”. In: *Phys. Rev.* D2 (1970), pages 1285–1292. DOI: 10.1103/PhysRevD.2.1285 (cited on page 25).
- [14] J. H. Christenson et al. “Evidence for the 2π Decay of the K20 Meson”. In: *Physical Review Letters* 13 (July 1964), pages 138–140. DOI: 10.1103/PhysRevLett.13.138 (cited on page 25).
- [15] Ziro Maki, Masami Nakagawa, and Shoichi Sakata. “Remarks on the Unified Model of Elementary Particles”. In: *Progress of Theoretical Physics* 28.5 (1962), pages 870–880. DOI: 10.1143/PTP.28.870. eprint: /oup/backfile/content_public/journal/ptp/28/5/10.1143/ptp.28.870/2/28-5-870.pdf. URL: <http://dx.doi.org/10.1143/PTP.28.870> (cited on page 25).
- [16] Claudio Giganti, Stéphane Lavignac, and Marco Zito. “Neutrino oscillations: the rise of the PMNS paradigm”. In: *Prog. Part. Nucl. Phys.* 98 (2018), pages 1–54. DOI: 10.1016/j.ppnp.2017.10.001. arXiv: 1710.00715 [hep-ex] (cited on page 25).
- [17] C. D. Anderson. “The Positive Electron”. In: *Phys. Rev.* 43 (1933), pages 491–494. DOI: 10.1103/PhysRev.43.491 (cited on page 26).
- [18] Paul A. M. Dirac. “The quantum theory of the electron”. In: *Proc. Roy. Soc. Lond.* A117 (1928), pages 610–624. DOI: 10.1098/rspa.1928.0023 (cited on page 26).
- [19] S. H. Neddermeyer and C. D. Anderson. “Note on the Nature of Cosmic Ray Particles”. In: *Phys. Rev.* 51 (1937), pages 884–886. DOI: 10.1103/PhysRev.51.884 (cited on page 26).
- [20] C. M. G. Lattes et al. “PROCESSES INVOLVING CHARGED MESONS”. In: *Nature* 159 (1947). [,42(1947)], pages 694–697. DOI: 10.1038/159694a0 (cited on page 26).
- [21] F. J. Hasert et al. “Observation of Neutrino Like Interactions Without Muon Or Electron in the Gargamelle Neutrino Experiment”. In: *Phys. Lett.* B46 (1973). [,5.15(1973)], pages 138–140. DOI: 10.1016/0370-2693(73)90499-1 (cited on page 26).
- [22] G. Arnison et al. “Experimental Observation of Isolated Large Transverse Energy Electrons with Associated Missing Energy at $s^{**}(1/2) = 540\text{-GeV}$ ”. In: *Phys. Lett.* B122 (1983). [,611(1983)], pages 103–116. DOI: 10.1016/0370-2693(83)91177-2 (cited on page 26).
- [23] G. Arnison et al. “Experimental Observation of Lepton Pairs of Invariant Mass Around $95\text{-GeV}/c^{**2}$ at the CERN SPS Collider”. In: *Phys. Lett.* B126 (1983). [,7.55(1983)], pages 398–410. DOI: 10.1016/0370-2693(83)90188-0 (cited on page 26).
- [24] S. W. Herb et al. “Observation of a Dimuon Resonance at 9.5-GeV in 400-GeV Proton-Nucleus Collisions”. In: *Phys. Rev. Lett.* 39 (1977), pages 252–255. DOI: 10.1103/PhysRevLett.39.252 (cited on page 26).
- [25] F. Abe et al. “Observation of top quark production in $\bar{p}p$ collisions”. In: *Phys. Rev. Lett.* 74 (1995), pages 2626–2631. DOI: 10.1103/PhysRevLett.74.2626. arXiv: hep-ex/9503002 [hep-ex] (cited on page 26).
- [26] D. P. Barber et al. “Discovery of Three Jet Events and a Test of Quantum Chromodynamics at PETRA Energies”. In: *Phys. Rev. Lett.* 43 (1979), page 830. DOI: 10.1103/PhysRevLett.43.830 (cited on page 26).
- [27] S. Schael et al. “Precision electroweak measurements on the Z resonance”. In: *Phys. Rept.* 427 (2006), pages 257–454. DOI: 10.1016/j.physrep.2005.12.006. arXiv: hep-ex/0509008 [hep-ex] (cited on page 26).
- [28] Sabine Riemann. “Precision electroweak physics at high energies”. In: *Rept. Prog. Phys.* 73 (2010), page 126201. DOI: 10.1088/0034-4885/73/12/126201 (cited on page 26).
- [29] Kenji Abe et al. “A High precision measurement of the left-right Z boson cross-section asymmetry”. In: *Phys. Rev. Lett.* 84 (2000), pages 5945–5949. DOI: 10.1103/PhysRevLett.84.5945. arXiv: hep-ex/0004026 [hep-ex] (cited on page 26).

- [30] Koya Abe et al. “First direct measurement of the parity violating coupling of the Z0 to the s quark”. In: *Phys. Rev. Lett.* 85 (2000), pages 5059–5063. DOI: 10.1103/PhysRevLett.85.5059. arXiv: hep-ex/0006019 [hep-ex] (cited on page 26).
- [31] Koya Abe et al. “An Improved direct measurement of leptonic coupling asymmetries with polarized Z bosons”. In: *Phys. Rev. Lett.* 86 (2001), pages 1162–1166. DOI: 10.1103/PhysRevLett.86.1162. arXiv: hep-ex/0010015 [hep-ex] (cited on page 26).
- [32] K. Abe et al. “First measurement of the left-right charge asymmetry in hadronic Z boson decays and a new determination of $\sin^{**2} \theta(W)(\text{eff})$ ”. In: *Phys. Rev. Lett.* 78 (1997), pages 17–21. DOI: 10.1103/PhysRevLett.78.17. arXiv: hep-ex/9609019 [hep-ex] (cited on page 26).
- [33] Timo Antero Aaltonen et al. “Combination of CDF and D0 W-Boson Mass Measurements”. In: *Phys. Rev.* D88.5 (2013), page 052018. DOI: 10.1103/PhysRevD.88.052018. arXiv: 1307.7627 [hep-ex] (cited on page 26).
- [34] “Combination of CDF and D0 Results on the Width of the W boson”. In: (2010). arXiv: 1003.2826 [hep-ex] (cited on page 26).
- [35] Morad Aaboud et al. “Measurement of the W-boson mass in pp collisions at $\sqrt{s} = 7$ TeV with the ATLAS detector”. In: *Eur. Phys. J.* C78.2 (2018), page 110. DOI: 10.1140/epjc/s10052-017-5475-4. arXiv: 1701.07240 [hep-ex] (cited on page 26).
- [36] ATLAS. URL: cds.cern.ch/record/2285809/files/ATLAS-CONF-2017-071.pdf (cited on page 26).
- [37] CMS. URL: cds.cern.ch/record/2235162/files/TOP-15-012-pas.pdf (cited on page 26).
- [38] CMS. URL: cds.cern.ch/record/2284594/files/TOP-17-007-pas.pdf (cited on page 26).
- [39] NA62 collaboration. URL: <https://indico.cern.ch/event/714178/> (cited on page 26).
- [40] Cari Cesarotti et al. “Interpreting the Electron EDM Constraint”. In: (2018). arXiv: 1810.07736 [hep-ph] (cited on page 27).
- [41] M. G. Aartsen et al. “Measurement of the multi-TeV neutrino cross section with IceCube using Earth absorption”. In: *Nature* 551 (2017), pages 596–600. DOI: 10.1038/nature24459. arXiv: 1711.08119 [hep-ex] (cited on page 27).
- [42] Andrea Castro. “Recent Top Quark Mass Measurements from CMS”. In: *Proceedings, 10th International Workshop on Top Quark Physics (TOP2017): Braga, Portugal, September 17-22, 2017*. 2017. arXiv: 1712.01027 [hep-ex] (cited on page 27).
- [43] PDG. URL: <http://pdg.lbl.gov/2018/reviews/rpp2018-rev-standard-model.pdf> (cited on pages 27, 29, 44, 52, 59, 64).
- [44] P. A. R. Ade et al. “Planck 2015 results. XIII. Cosmological parameters”. In: *Astron. Astrophys.* 594 (2016), A13. DOI: 10.1051/0004-6361/201525830. arXiv: 1502.01589 [astro-ph.CO] (cited on page 28).
- [45] Evgige Corbelli and Paolo Salucci. “The Extended Rotation Curve and the Dark Matter Halo of M33”. In: *Mon. Not. Roy. Astron. Soc.* 311 (2000), pages 441–447. DOI: 10.1046/j.1365-8711.2000.03075.x. arXiv: astro-ph/9909252 [astro-ph] (cited on page 28).
- [46] S. M. Faber and R. E. Jackson. “Velocity dispersions and mass to light ratios for elliptical galaxies”. In: *Astrophys. J.* 204 (1976), page 668. DOI: 10.1086/154215 (cited on page 28).
- [47] Steven W. Allen, August E. Evrard, and Adam B. Mantz. “Cosmological Parameters from Observations of Galaxy Clusters”. In: *Ann. Rev. Astron. Astrophys.* 49 (2011), pages 409–470. DOI: 10.1146/annurev-astro-081710-102514. arXiv: 1103.4829 [astro-ph.CO] (cited on page 28).

- [48] Priyamvada Natarajan et al. “Mapping substructure in the HST Frontier Fields cluster lenses and in cosmological simulations”. In: *Mon. Not. Roy. Astron. Soc.* 468.2 (2017), pages 1962–1980. DOI: 10.1093/mnras/stw3385. arXiv: 1702.04348 [astro-ph.GA] (cited on page 28).
- [49] John F. Donoghue. “The effective field theory treatment of quantum gravity”. In: *AIP Conf. Proc.* 1483 (2012), pages 73–94. DOI: 10.1063/1.4756964. arXiv: 1209.3511 [gr-qc] (cited on page 28).
- [50] C. D. McCoy. “Does inflation solve the hot big bang model’s fine-tuning problems?” In: *Stud. Hist. Phil. Sci.* B51 (2015), pages 23–36. DOI: 10.1016/j.shpsb.2015.06.002 (cited on page 28).
- [51] R. D. Peccei. “The Strong CP problem and axions”. In: *Lect. Notes Phys.* 741 (2008). [,3(2006)], pages 3–17. DOI: 10.1007/978-3-540-73518-2_1. arXiv: hep-ph/0607268 [hep-ph] (cited on page 29).
- [52] C. Amsler et al. “Review of Particle Physics”. In: *Physics Letters B* 667.1 (2008). Review of Particle Physics, pages 1–6. ISSN: 0370-2693. DOI: <https://doi.org/10.1016/j.physletb.2008.07.018>. URL: <http://www.sciencedirect.com/science/article/pii/S0370269308008435> (cited on page 29).
- [53] Georges Aad et al. “Combined Measurement of the Higgs Boson Mass in pp Collisions at $\sqrt{s} = 7$ and 8 TeV with the ATLAS and CMS Experiments”. In: *Phys. Rev. Lett.* 114 (2015), page 191803. DOI: 10.1103/PhysRevLett.114.191803. arXiv: 1503.07589 [hep-ex] (cited on page 29).
- [54] Susanne Mertens. “Direct Neutrino Mass Experiments”. In: *J. Phys. Conf. Ser.* 718.2 (2016), page 022013. DOI: 10.1088/1742-6596/718/2/022013. arXiv: 1605.01579 [nucl-ex] (cited on page 29).
- [55] Ivan Esteban et al. “Updated fit to three neutrino mixing: exploring the accelerator-reactor complementarity”. In: *JHEP* 01 (2017), page 087. DOI: 10.1007/JHEP01(2017)087. arXiv: 1611.01514 [hep-ph] (cited on page 29).
- [56] NuFIT. URL: <http://www.nu-fit.org/?q=node/177> (cited on page 29).
- [57] nobel2004. URL: <https://www.nobelprize.org/prizes/physics/2004/popular-information/> (cited on page 30).
- [58] Xiao-Gang He, Girish C. Joshi, and B. H. McKellar. “The Quantization of the Electric Charge in Gauge Theories”. In: *Europhys. Lett.* 10 (1989), page 709. DOI: 10.1209/0295-5075/10/8/002 (cited on pages 30, 33).
- [59] Stefano Bertolini, Luca Di Luzio, and Michal Malinsky. “Intermediate mass scales in the non-supersymmetric SO(10) grand unification: A Reappraisal”. In: *Phys. Rev.* D80 (2009), page 015013. DOI: 10.1103/PhysRevD.80.015013. arXiv: 0903.4049 [hep-ph] (cited on page 30).
- [60] Hong-Wei Yu. “SU(8) GUT MODELS WITH STABLE PROTON, N ANTI-N OSCILLATIONS, FRACTIONAL CHARGES AND LOW MASS MONOPOLES”. In: *Phys. Lett.* 142B (1984), pages 42–46. DOI: 10.1016/0370-2693(84)91132-8 (cited on pages 30, 34).
- [61] Xiao-Gang Wen and Edward Witten. “Electric and Magnetic Charges in Superstring Models”. In: *Nucl. Phys.* B261 (1985), pages 651–677. DOI: 10.1016/0550-3213(85)90592-9 (cited on pages 31, 34).
- [62] Gregory G. Athanasiou et al. “Remarks on Wilson Lines, Modular Invariance and Possible String Relics in Calabi-yau Compactifications”. In: *Phys. Lett.* B214 (1988), pages 55–62. DOI: 10.1016/0370-2693(88)90451-0 (cited on pages 31, 34).
- [63] Stephen M. Barr, D. B. Reiss, and A. Zee. “Fractional Charges, Monopoles and Peculiar Photons”. In: *Phys. Rev. Lett.* 50 (1983), page 317. DOI: 10.1103/PhysRevLett.50.317 (cited on page 34).

- [64] P. H. Frampton and T. W. Kephart. “Fractionally Charged Particles as Evidence for Supersymmetry”. In: *Phys. Rev. Lett.* 49 (1982), page 1310. DOI: 10.1103/PhysRevLett.49.1310 (cited on page 34).
- [65] Katsuji Yamamoto. “Fractionally Charged Leptons in the SO(14) GUT”. In: *Phys. Lett.* 120B (1983), pages 157–160. DOI: 10.1016/0370-2693(83)90643-3 (cited on page 34).
- [66] Fang-xiao Dong et al. “Fractional Charges, Monopoles and Peculiar Photons in SO(18) GUT Models”. In: *Phys. Lett.* 129B (1983), pages 405–410. DOI: 10.1016/0370-2693(83)90129-6 (cited on page 34).
- [67] Xiang-Dong Jiang and Xian-Jian Zhou. “SO(10) X SO(8) MODEL WITH FRACTIONAL CHARGES, MONOPOLES AND PECULIAR PHOTONS. (IN CHINESE)”. In: *HEPNP* 9 (1985), pages 421–429 (cited on page 34).
- [68] K. Abe et al. “Search for proton decay via $p \rightarrow e^+ \pi^0$ and $p \rightarrow \mu^+ \pi^0$ in 0.31 megaton years exposure of the Super-Kamiokande water Cherenkov detector”. In: *Phys. Rev.* D95.1 (2017), page 012004. DOI: 10.1103/PhysRevD.95.012004. arXiv: 1610.03597 [hep-ex] (cited on page 34).
- [69] Ignatios Antoniadis and K. Benakli. “Fractionally charged particles and supersymmetry breaking in 4-D strings”. In: *Phys. Lett.* B295 (1992). [Erratum: *Phys. Lett.* B407,449(1997)], pages 219–224. DOI: 10.1016/S0370-2693(97)00755-7, 10.1016/0370-2693(92)91557-P. arXiv: hep-th/9209020 [hep-th] (cited on page 34).
- [70] Bob Holdom. “Two U(1)’s and Epsilon Charge Shifts”. In: *Phys. Lett.* 166B (1986), pages 196–198. DOI: 10.1016/0370-2693(86)91377-8 (cited on page 34).
- [71] Eder Izquierre and Itay Yavin. “New window to millicharged particles at the LHC”. In: *Phys. Rev.* D92.3 (2015), page 035014. DOI: 10.1103/PhysRevD.92.035014. arXiv: 1506.04760 [hep-ph] (cited on page 34).
- [72] David E. Brahm and Lawrence J. Hall. “U(1)-prime DARK MATTER”. In: *Phys. Rev.* D41 (1990), page 1067. DOI: 10.1103/PhysRevD.41.1067 (cited on page 34).
- [73] C. Boehm and Pierre Fayet. “Scalar dark matter candidates”. In: *Nucl. Phys.* B683 (2004), pages 219–263. DOI: 10.1016/j.nuclphysb.2004.01.015. arXiv: hep-ph/0305261 [hep-ph] (cited on page 34).
- [74] Maxim Pospelov, Adam Ritz, and Mikhail B. Voloshin. “Secluded WIMP Dark Matter”. In: *Phys. Lett.* B662 (2008), pages 53–61. DOI: 10.1016/j.physletb.2008.02.052. arXiv: 0711.4866 [hep-ph] (cited on page 34).
- [75] James D. Bjorken et al. “New Fixed-Target Experiments to Search for Dark Gauge Forces”. In: *Phys. Rev.* D80 (2009), page 075018. DOI: 10.1103/PhysRevD.80.075018. arXiv: 0906.0580 [hep-ph] (cited on page 34).
- [76] Gabriel Magill et al. “Millicharged particles in neutrino experiments”. In: (2018). arXiv: 1806.03310 [hep-ph] (cited on page 34).
- [77] R. Acciarri et al. “Long-Baseline Neutrino Facility (LBNF) and Deep Underground Neutrino Experiment (DUNE)”. In: (2015). arXiv: 1512.06148 [physics.ins-det] (cited on page 34).
- [78] M. Anelli et al. “A facility to Search for Hidden Particles (SHiP) at the CERN SPS”. In: (2015). arXiv: 1504.04956 [physics.ins-det] (cited on page 34).
- [79] Marco Battaglieri et al. “US Cosmic Visions: New Ideas in Dark Matter 2017: Community Report”. In: (2017). arXiv: 1707.04591 [hep-ph] (cited on page 34).
- [80] S. I. Alvis et al. “First Limit on the Direct Detection of Lightly Ionizing Particles for Electric Charge as Low as e/1000 with the Majorana Demonstrator”. In: *Phys. Rev. Lett.* 120.21 (2018), page 211804. DOI: 10.1103/PhysRevLett.120.211804. arXiv: 1801.10145 [hep-ex] (cited on page 34).

- [81] L. Lyons. “Quark Search Experiments at Accelerators and in Cosmic Rays”. In: *Phys. Rept.* 129 (1985), page 225. DOI: 10.1016/0370-1573(85)90011-0 (cited on page 35).
- [82] J. J. Aubert et al. “A Search for Free Quarks in Deep Inelastic Muon Scattering”. In: *Phys. Lett.* 133B (1983), page 461. DOI: 10.1016/0370-2693(83)90828-6 (cited on page 35).
- [83] A. E. Bondar et al. “SEARCH FOR LIGHT PARTICLES WITH CHARGE 2/3 IN e^+e^- ANNIHILATION”. In: *JETP Lett.* 40 (1984). [Pisma Zh. Eksp. Teor. Fiz. 40, 440 (1984)], pages 1265–1268 (cited on page 35).
- [84] H. Aihara et al. “Search for $q = 2/3e$ and $q = 1/3e$ particles produced in e^+e^- annihilations”. In: *Phys. Rev. Lett.* 52 (1984), page 2332. DOI: 10.1103/PhysRevLett.52.2332 (cited on page 35).
- [85] G. Abbiendi et al. “Search for stable and longlived massive charged particles in e^+e^- collisions at $s^{**}(1/2) = 130\text{-GeV}$ to 209-GeV ”. In: *Phys. Lett.* B572 (2003), pages 8–20. DOI: 10.1016/S0370-2693(03)00639-7. arXiv: hep-ex/0305031 [hep-ex] (cited on page 35).
- [86] P. Abreu et al. “Search for stable heavy charged particles in e^+e^- collisions at $s^{**}(1/2) = 130\text{-GeV}$ to 136-GeV , 161-GeV and 172-GeV ”. In: *Phys. Lett.* B396 (1997), pages 315–326. DOI: 10.1016/S0370-2693(97)00152-4 (cited on page 35).
- [87] R. Akers et al. “Search for heavy charged particles and for particles with anomalous charge in e^+e^- collisions at LEP”. In: *Z. Phys.* C67 (1995), pages 203–212. DOI: 10.1007/BF01571281 (cited on page 35).
- [88] D. Buskulic et al. “Search for particles with unexpected mass and charge in Z decays”. In: *Phys. Lett.* B303 (1993), pages 198–208. DOI: 10.1016/0370-2693(93)90066-Q (cited on page 35).
- [89] M. Banner et al. “A New Search for Relativistic Particles With Fractional Electric Charge at the CERN $p\bar{p}$ Collider”. In: *Phys. Lett.* 156B (1985), pages 129–133. DOI: 10.1016/0370-2693(85)91368-1 (cited on page 35).
- [90] F. Abe et al. “Limits on the production of massive stable charged particles”. In: *Phys. Rev.* D46 (1992), R1889–R1894. DOI: 10.1103/PhysRevD.46.R1889 (cited on page 35).
- [91] D. Acosta et al. “Search for long-lived charged massive particles in $\bar{p}p$ collisions at $\sqrt{s} = 1.8$ TeV”. In: *Phys. Rev. Lett.* 90 (2003), page 131801. DOI: 10.1103/PhysRevLett.90.131801. arXiv: hep-ex/0211064 [hep-ex] (cited on page 35).
- [92] Serguei Chatrchyan et al. “Search for fractionally charged particles in pp collisions at $\sqrt{s} = 7$ TeV”. In: *Phys. Rev.* D87.9 (2013), page 092008. DOI: 10.1103/PhysRevD.87.092008. arXiv: 1210.2311 [hep-ex] (cited on page 35).
- [93] M. Ambrosio et al. “Final search for lightly ionizing particles with the MACRO detector”. In: (2004). arXiv: hep-ex/0402006 [hep-ex] (cited on page 36).
- [94] M. Mori et al. “Search for fractionally charged particles in Kamiokande-II”. In: *Phys. Rev.* D43 (1991), pages 2843–2846. DOI: 10.1103/PhysRevD.43.2843 (cited on page 36).
- [95] G. Giacomelli and A. Margiotta. “The MACRO Experiment at Gran Sasso”. In: *Charles Peck Fest Pasadena, California, January 21, 2005*. 2007. arXiv: 0707.1691 [hep-ex] (cited on page 37).
- [96] Thomas K. Gaisser, Ralph Engel, and Elisa Resconi. *Cosmic Rays and Particle Physics*. Cambridge University Press, 2016. URL: <http://www.cambridge.org/de/academic/subjects/physics/cosmology-relativity-and-gravitation/cosmic-rays-and-particle-physics-2nd-edition?format=HB> (cited on pages 39, 42, 47, 50).
- [97] The Nobel Prize. URL: <https://www.nobelprize.org/prizes/physics/1936/ceremony-speech/> (cited on page 39).
- [98] J. Clay. *Penetrating radiation*. Volume 30. 1927, pages 1115–1127 (cited on page 40).

- [99] R. A. Millikan and G. H. Cameron. “The Origin of the Cosmic Rays”. In: *Phys. Rev.* 32 (4 Oct. 1928), pages 533–557. DOI: 10.1103/PhysRev.32.533. URL: <https://link.aps.org/doi/10.1103/PhysRev.32.533> (cited on page 40).
- [100] Thomas K. Gaisser and Todor Stanev. “High-energy cosmic rays”. In: *Nuclear Physics A* 777 (2006). Special Issue on Nuclear Astrophysics, pages 98–110. ISSN: 0375-9474. DOI: <https://doi.org/10.1016/j.nuclphysa.2005.01.024>. URL: <http://www.sciencedirect.com/science/article/pii/S0375947405000540> (cited on page 40).
- [101] Pasquale Blasi. “The Origin of Galactic Cosmic Rays”. In: *Astron. Astrophys. Rev.* 21 (2013), page 70. DOI: 10.1007/s00159-013-0070-7. arXiv: 1311.7346 [astro-ph.HE] (cited on page 41).
- [102] Thomas K. Gaisser, Todor Stanev, and Serap Tilav. “Cosmic Ray Energy Spectrum from Measurements of Air Showers”. In: *Front. Phys.(Beijing)* 8 (2013), pages 748–758. DOI: 10.1007/s11467-013-0319-7. arXiv: 1303.3565 [astro-ph.HE] (cited on pages 41–43, 92, 95, 150).
- [103] M A Malkov and L O’C Drury. “Nonlinear theory of diffusive acceleration of particles by shock waves”. In: *Reports on Progress in Physics* 64.4 (2001), page 429. URL: <http://stacks.iop.org/0034-4885/64/i=4/a=201> (cited on page 42).
- [104] “Detection of the Small Magellanic Cloud in gamma-rays with Fermi/LAT”. In: *Astron. Astrophys.* 523 (2010), A46. DOI: 10.1051/0004-6361/201014855. arXiv: 1008.2127 [astro-ph.HE] (cited on page 42).
- [105] M. Ackermann et al. “Detection of the Characteristic Pion-Decay Signature in Supernova Remnants”. In: *Science* 339 (2013), page 807. DOI: 10.1126/science.1231160. arXiv: 1302.3307 [astro-ph.HE] (cited on page 42).
- [106] W. D. Apel et al. “Kneelike structure in the spectrum of the heavy component of cosmic rays observed with KASCADE-Grande”. In: *Phys. Rev. Lett.* 107 (2011), page 171104. DOI: 10.1103/PhysRevLett.107.171104. arXiv: 1107.5885 [astro-ph.HE] (cited on page 43).
- [107] A. P. Garyaka et al. “All-particle primary energy spectrum in the 3-200 PeV energy range”. In: *J. Phys.* G35 (2008), page 115201. DOI: 10.1088/0954-3899/35/11/115201. arXiv: 0808.1421 [astro-ph] (cited on page 43).
- [108] Kenneth Greisen. “End to the cosmic ray spectrum?” In: *Phys. Rev. Lett.* 16 (1966), pages 748–750. DOI: 10.1103/PhysRevLett.16.748 (cited on page 43).
- [109] G. T. Zatsepin and V. A. Kuzmin. “Upper limit of the spectrum of cosmic rays”. In: *JETP Lett.* 4 (1966). [*Pisma Zh. Eksp. Teor. Fiz.* 4,114(1966)], pages 78–80 (cited on page 43).
- [110] J. Bellido et al. “Proceedings of Science”. In: *ICRC* 301 (506 2017) (cited on page 43).
- [111] D. Allard et al. “Implications of the cosmic ray spectrum for the mass composition at the highest energies”. In: *JCAP* 0810 (2008), page 033. DOI: 10.1088/1475-7516/2008/10/033. arXiv: 0805.4779 [astro-ph] (cited on page 44).
- [112] A. M. Hillas. “The Origin of Ultrahigh-Energy Cosmic Rays”. In: *Ann. Rev. Astron. Astrophys.* 22 (1984), pages 425–444. DOI: 10.1146/annurev.aa.22.090184.002233 (cited on page 44).
- [113] Pablo M. Bauleo and Julio Rodriguez Martino. “The dawn of the particle astronomy era in ultra-high-energy cosmic rays”. In: *Nature* 458N7240 (2009), pages 847–851. DOI: 10.1038/nature07948 (cited on page 45).
- [114] M. Nagano and Alan A. Watson. “Observations and implications of the ultrahigh-energy cosmic rays”. In: *Rev. Mod. Phys.* 72 (2000), pages 689–732. DOI: 10.1103/RevModPhys.72.689 (cited on page 44).

- [115] Alexander Aab et al. “Observation of a Large-scale Anisotropy in the Arrival Directions of Cosmic Rays above 8×10^{18} eV”. In: *Science* 357.6537 (2017), pages 1266–1270. DOI: 10.1126/science.aan4338. arXiv: 1709.07321 [astro-ph.HE] (cited on page 44).
- [116] E. Waxman. “IceCube’s Neutrinos: The beginning of extra-Galactic neutrino astrophysics?” In: *Proceedings, 9th Rencontres du Vietnam: Windows on the Universe: Quy Nhon, Vietnam, August 11-17, 2013.* 2013, pages 161–168. arXiv: 1312.0558 [astro-ph.HE] (cited on page 44).
- [117] P. O. Lagage and C. J. Cesarsky. “The maximum energy of cosmic rays accelerated by supernova shocks”. In: *Astron. Astrophys.* 125 (1983), pages 249–257 (cited on page 49).
- [118] T. Stanev. *High Energy Cosmic Rays*. Springer Praxis Books. Springer Berlin Heidelberg, 2010. ISBN: 9783540851486. URL: <https://books.google.be/books?id=1y9YEYHafBMC> (cited on page 49).
- [119] C. Megan Urry and Paolo Padovani. “Unified schemes for radio-loud active galactic nuclei”. In: *Publ. Astron. Soc. Pac.* 107 (1995), page 803. DOI: 10.1086/133630. arXiv: astro-ph/9506063 [astro-ph] (cited on page 49).
- [120] Robert Antonucci. “Unified models for active galactic nuclei and quasars”. In: *Ann. Rev. Astron. Astrophys.* 31 (1993), pages 473–521. DOI: 10.1146/annurev.aa.31.090193.002353 (cited on page 49).
- [121] Demosthenes Kazanas et al. “Toward a Unified AGN Structure”. In: (2012). arXiv: 1206.5022 [astro-ph.HE] (cited on page 49).
- [122] J. Abraham et al. “Correlation of the highest-energy cosmic rays with the positions of nearby active galactic nuclei”. In: *Astropart. Phys.* 29 (2008). [Erratum: *Astropart. Phys.* 30,45(2008)], pages 188–204. DOI: 10.1016/j.astropartphys.2008.06.004, 10.1016/j.astropartphys.2008.01.002. arXiv: 0712.2843 [astro-ph] (cited on page 49).
- [123] Ray W. Klebesadel, Ian B. Strong, and Roy A. Olson. “Observations of Gamma-Ray Bursts of Cosmic Origin”. In: *Astrophys. J.* 182 (1973), pages L85–L88. DOI: 10.1086/181225 (cited on page 50).
- [124] C. A. Meegan et al. “Spatial distribution of gamma-ray bursts observed by BATSE”. In: *Nature* 355 (1992), pages 143–145. DOI: 10.1038/355143a0 (cited on page 50).
- [125] B. P. Abbott et al. “GW170817: Observation of Gravitational Waves from a Binary Neutron Star Inspiral”. In: *Phys. Rev. Lett.* 119.16 (2017), page 161101. DOI: 10.1103/PhysRevLett.119.161101. arXiv: 1710.05832 [gr-qc] (cited on page 50).
- [126] B. P. Abbott et al. “GW170814: A Three-Detector Observation of Gravitational Waves from a Binary Black Hole Coalescence”. In: *Phys. Rev. Lett.* 119.14 (2017), page 141101. DOI: 10.1103/PhysRevLett.119.141101. arXiv: 1709.09660 [gr-qc] (cited on page 50).
- [127] B.. P.. Abbott et al. “GW170608: Observation of a 19-solar-mass Binary Black Hole Coalescence”. In: *Astrophys. J.* 851.2 (2017), page L35. DOI: 10.3847/2041-8213/aa9f0c. arXiv: 1711.05578 [astro-ph.HE] (cited on page 50).
- [128] Benjamin P. Abbott et al. “GW170104: Observation of a 50-Solar-Mass Binary Black Hole Coalescence at Redshift 0.2”. In: *Phys. Rev. Lett.* 118.22 (2017). [Erratum: *Phys. Rev. Lett.* 121,no.12,129901(2018)], page 221101. DOI: 10.1103/PhysRevLett.118.221101, 10.1103/PhysRevLett.121.129901. arXiv: 1706.01812 [gr-qc] (cited on page 50).
- [129] B. P. Abbott et al. “GW151226: Observation of Gravitational Waves from a 22-Solar-Mass Binary Black Hole Coalescence”. In: *Phys. Rev. Lett.* 116.24 (2016), page 241103. DOI: 10.1103/PhysRevLett.116.241103. arXiv: 1606.04855 [gr-qc] (cited on page 50).
- [130] F. Acero. “Detection of Gamma Rays From a Starburst Galaxy”. In: *Science* 326 (2009), page 1080. DOI: 10.1126/science.1178826. arXiv: 0909.4651 [astro-ph.HE] (cited on page 50).

- [131] Niklas Karlsson. “Discovery of VHE Gamma-ray Emission from the Starburst Galaxy M82”. In: (2009). arXiv: 0912.3807 [astro-ph.HE] (cited on page 50).
- [132] Kohta Murase, Susumu Inoue, and Shigehiro Nagataki. “Cosmic Rays above the Second Knee from Clusters of Galaxies and Associated High-Energy Neutrino Emission”. In: *The Astrophysical Journal Letters* 689.2 (2008), page L105. URL: <http://stacks.iop.org/1538-4357/689/i=2/a=L105> (cited on page 50).
- [133] C. Grupen. *Astroparticle physics*. 2005. ISBN: 9783540253129. URL: <http://www.springer.com/book/3-540-25312-2> (cited on pages 51, 52).
- [134] U. F. Katz and Ch. Spiering. “High-Energy Neutrino Astrophysics: Status and Perspectives”. In: *Prog. Part. Nucl. Phys.* 67 (2012), pages 651–704. DOI: 10.1016/j.ppnp.2011.12.001. arXiv: 1111.0507 [astro-ph.HE] (cited on page 53).
- [135] Morihiro Honda et al. “Calculation of atmospheric neutrino flux using the interaction model calibrated with atmospheric muon data”. In: *Phys. Rev. D* 75 (2007), page 043006. DOI: 10.1103/PhysRevD.75.043006. arXiv: astro-ph/0611418 [astro-ph] (cited on pages 54, 93–95, 150).
- [136] M. G. Aartsen et al. “The IceCube Neutrino Observatory - Contributions to ICRC 2017 Part II: Properties of the Atmospheric and Astrophysical Neutrino Flux”. In: (2017). arXiv: 1710.01191 [astro-ph.HE] (cited on page 55).
- [137] Kiyoshi Niu, Eiko Mikumo, and Yasuko Maeda. “A Possible Decay in Flight of a New Type Particle”. In: *Progress of Theoretical Physics* 46.5 (1971), pages 1644–1646. DOI: 10.1143/PTP.46.1644. eprint: /oup/backfile/content_public/journal/ptp/46/5/10.1143/ptp.46.1644/2/46-5-1644.pdf. URL: <http://dx.doi.org/10.1143/PTP.46.1644> (cited on page 54).
- [138] Rikard Enberg, Mary Hall Reno, and Ina Sarcevic. “Prompt neutrino fluxes from atmospheric charm”. In: *Phys. Rev. D* 78 (2008), page 043005. DOI: 10.1103/PhysRevD.78.043005. arXiv: 0806.0418 [hep-ph] (cited on pages 55, 93–95).
- [139] M. G. Aartsen et al. “Multimessenger observations of a flaring blazar coincident with high-energy neutrino IceCube-170922A”. In: *Science* 361.6398 (2018), eaat1378. DOI: 10.1126/science.aat1378. arXiv: 1807.08816 [astro-ph.HE] (cited on page 55).
- [140] Kate Scholberg. “Supernova Neutrino Detection”. In: *Ann. Rev. Nucl. Part. Sci.* 62 (2012), pages 81–103. DOI: 10.1146/annurev-nucl-102711-095006. arXiv: 1205.6003 [astro-ph.IM] (cited on page 55).
- [141] Lutz Kopke. “Supernova Neutrino Detection with IceCube”. In: *J. Phys. Conf. Ser.* 309 (2011), page 012029. DOI: 10.1088/1742-6596/309/1/012029. arXiv: 1106.6225 [astro-ph.HE] (cited on page 56).
- [142] Aya Ishihara. “Diffuse Neutrino Fluxes and GZK Neutrinos with IceCube”. In: *JPS Conf. Proc.* 15 (2017), page 011008. DOI: 10.7566/JPSCP.15.011008 (cited on page 56).
- [143] nobel1958. URL: <https://www.nobelprize.org/prizes/physics/1958/summary/> (cited on page 57).
- [144] M. G. Aartsen et al. “Measurements using the inelasticity distribution of multi-TeV neutrino interactions in IceCube”. In: (2018). arXiv: 1808.07629 [hep-ex] (cited on page 60).
- [145] “Design, Implementation and Test of a New Feature Extractor for the IceCube Neutrino Observatory”. In: (2010) (cited on page 60).
- [146] Paul H. Barrett et al. “Interpretation of Cosmic-Ray Measurements Far Underground”. In: *Rev. Mod. Phys.* 24.3 (1952), pages 133–178. DOI: 10.1103/RevModPhys.24.133 (cited on page 62).

- [147] Dmitry Chirkin and Wolfgang Rhode. “Muon Monte Carlo: A High-precision tool for muon propagation through matter”. In: (2004). arXiv: hep-ph/0407075 [hep-ph] (cited on pages 63–66).
- [148] Dmitry Chirkin. “Study of South Pole ice transparency with IceCube flashers”. In: *Proceedings, 32nd International Cosmic Ray Conference (ICRC 2011): Beijing, China, August 11-18, 2011*. Volume 4, page 161. DOI: 10.7529/ICRC2011/V04/0333 (cited on pages 63, 98).
- [149] S. R. Kelner, R. P. Kokoulin, and A. A. Petrukhin. “About cross-section for high-energy muon bremsstrahlung”. In: (1995) (cited on page 65).
- [150] AMANDA collaboration. URL: <http://amanda.uci.edu/> (cited on page 67).
- [151] E. Andres et al. “The AMANDA neutrino telescope: Principle of operation and first results”. In: *Astropart. Phys.* 13 (2000), pages 1–20. DOI: 10.1016/S0927-6505(99)00092-4. arXiv: astro-ph/9906203 [astro-ph] (cited on page 67).
- [152] J. Ahrens et al. “Observation of high-energy atmospheric neutrinos with the Antarctic Muon and Neutrino Detector Array”. In: *Phys. Rev.* D66 (2002), page 012005. DOI: 10.1103/PhysRevD.66.012005. arXiv: astro-ph/0205109 [astro-ph] (cited on page 67).
- [153] R. Abbasi et al. “The Design and Performance of IceCube DeepCore”. In: *Astropart. Phys.* 35 (2012), pages 615–624. DOI: 10.1016/j.astropartphys.2012.01.004. arXiv: 1109.6096 [astro-ph.IM] (cited on page 69).
- [154] Nicholas Choma et al. “Graph Neural Networks for IceCube Signal Classification”. In: (2018). arXiv: 1809.06166 [cs.LG] (cited on page 70).
- [155] M. G. Aartsen et al. “The IceCube Neutrino Observatory: Instrumentation and Online Systems”. In: *JINST* 12.03 (2017), P03012. DOI: 10.1088/1748-0221/12/03/P03012. arXiv: 1612.05093 [astro-ph.IM] (cited on pages 71, 73, 74).
- [156] R. Abbasi et al. “Calibration and Characterization of the IceCube Photomultiplier Tube”. In: *Nucl. Instrum. Meth.* A618 (2010), pages 139–152. DOI: 10.1016/j.nima.2010.03.102. arXiv: 1002.2442 [astro-ph.IM] (cited on pages 71, 98).
- [157] M. G. Aartsen et al. “Measurement of South Pole ice transparency with the IceCube LED calibration system”. In: *Nucl. Instrum. Meth.* A711 (2013), pages 73–89. DOI: 10.1016/j.nima.2013.01.054. arXiv: 1301.5361 [astro-ph.IM] (cited on pages 72, 79).
- [158] M. G. Aartsen et al. “The IceCube Realtime Alert System”. In: *Astropart. Phys.* 92 (2017), pages 30–41. DOI: 10.1016/j.astropartphys.2017.05.002. arXiv: 1612.06028 [astro-ph.HE] (cited on page 77).
- [159] Dariusz Góra. “High-Energy Gamma-Ray Follow-Up Program Using Neutrino Triggers from IceCube”. In: *Proceedings, 33rd International Cosmic Ray Conference (ICRC2013): Rio de Janeiro, Brazil, July 2-9, 2013*, page 0537. URL: <http://www.cbpf.br/%7Eicrc2013/papers/icrc2013-0537.pdf> (cited on page 77).
- [160] The IceCube Collaboration. URL: https://wiki.icecube.wisc.edu/index.php/Pass2_Re-Processing (cited on pages 78, 99).
- [161] The IceCube Collaboration. URL: https://docushare.icecube.wisc.edu/dsweb/Get/Document-56552/dst_proposal_2011.pdf (cited on page 78).
- [162] M. G. Aartsen et al. “Search for steady point-like sources in the astrophysical muon neutrino flux with 8 years of IceCube data”. In: (2018). arXiv: 1811.07979 [hep-ph] (cited on page 78).
- [163] The IceCube Collaboration. URL: https://icecube.wisc.edu/~kjero/Bootcamp/2015/Notebooks/Reconstruction_Introduction.html (cited on page 79).

- [164] M. Ackermann et al. “Optical properties of deep glacial ice at the South Pole”. In: *J. Geophys. Res. Atmos.* 111.D13 (2006), page D13203. doi: 10.1029/2005JD006687 (cited on pages 79, 80).
- [165] Dmitry Chirkin. “Evidence of optical anisotropy of the South Pole ice”. In: *Proceedings, 33rd International Cosmic Ray Conference (ICRC2013): Rio de Janeiro, Brazil, July 2-9, 2013*, page 0580. URL: <http://www.cbpf.br/%7Eicrc2013/papers/icrc2013-0580.pdf> (cited on pages 80, 81).
- [166] Samridha Kunwar et al. “The IceTop Scintillator Upgrade”. In: *PoS ICRC2017* (2018), page 401. doi: 10.22323/1.301.0401 (cited on page 81).
- [167] Jan Auffenberg. “IceAct: Imaging Air Cherenkov Telescopes with SiPMs at the South Pole for IceCube-Gen2”. In: *PoS ICRC2017* (2018), page 1055. doi: 10.22323/1.301.1055 (cited on page 81).
- [168] Satoshi Shimizu et al. “Overview and performance of the D-Egg optical sensor for IceCube-Gen2”. In: *PoS ICRC2017* (2018), page 1051. doi: 10.22323/1.301.1051 (cited on page 81).
- [169] Lew Classen et al. “The mDOM - A multi-PMT digital optical module for the IceCube-Gen2 neutrino telescope”. In: *PoS ICRC2017* (2018), page 1047. doi: 10.22323/1.301.1047 (cited on page 81).
- [170] M. Jeong and W. Kang. “A camera system for IceCube-Gen2”. In: *PoS ICRC2017* (2018), page 1040. doi: 10.22323/1.301.1040 (cited on page 81).
- [171] Elisa Resconi, Kai Krings, and Kai Krings Martin Rongen. “The Precision Optical CALibration Module for IceCube-Gen2: First Prototype”. In: *PoS ICRC2017* (2018), page 934. doi: 10.22323/1.301.0934 (cited on page 81).
- [172] Erik Blaufuss, C. Kopper, and C. Haack. “The IceCube-Gen2 High Energy Array”. In: *PoS ICRC2015* (2016), page 1146. doi: 10.22323/1.236.1146 (cited on page 82).
- [173] Markus Ahlers and Francis Halzen. “Pinpointing Extragalactic Neutrino Sources in Light of Recent IceCube Observations”. In: *Phys. Rev. D90.4* (2014), page 043005. doi: 10.1103/PhysRevD.90.043005. arXiv: 1406.2160 [astro-ph.HE] (cited on page 82).
- [174] Sebastian Euler, Javier Gonzalez, and Ben Roberts. “Simulation Studies for a Surface Veto Array to Identify Astrophysical Neutrinos at the South Pole”. In: *PoS ICRC2015* (2016), page 1070. doi: 10.22323/1.236.1070 (cited on page 83).
- [175] Frank G. Schröder. “Radio detection of Cosmic-Ray Air Showers and High-Energy Neutrinos”. In: *Prog. Part. Nucl. Phys.* 93 (2017), pages 1–68. doi: 10.1016/j.ppnp.2016.12.002. arXiv: 1607.08781 [astro-ph.IM] (cited on page 83).
- [176] P. Allison et al. “Performance of two Askaryan Radio Array stations and first results in the search for ultrahigh energy neutrinos”. In: *Phys. Rev. D93.8* (2016), page 082003. doi: 10.1103/PhysRevD.93.082003. arXiv: 1507.08991 [astro-ph.HE] (cited on page 83).
- [177] Christian Glaser. “ARIANNA: Measurement of cosmic rays with a radio neutrino detector in Antarctica”. In: *Acoustic and Radio EeV Neutrino Detection Activities (ARENA 2018) Catania, Italy, June 12-15, 2018*. 2018. arXiv: 1811.10661 [astro-ph.IM] (cited on page 83).
- [178] Don Colladay and V. Alan Kostelecky. “Lorentz violating extension of the standard model”. In: *Phys. Rev. D58* (1998), page 116002. doi: 10.1103/PhysRevD.58.116002. arXiv: hep-ph/9809521 [hep-ph] (cited on page 84).
- [179] M. G. Aartsen et al. “Neutrino Interferometry for High-Precision Tests of Lorentz Symmetry with IceCube”. In: *Nature Phys.* 14.9 (2018), pages 961–966. doi: 10.1038/s41567-018-0172-2. arXiv: 1709.03434 [hep-ex] (cited on page 84).

- [180] R. Abbasi et al. “Search for a Lorentz-violating sidereal signal with atmospheric neutrinos in IceCube”. In: *Phys. Rev.* D82 (2010), page 112003. DOI: 10.1103/PhysRevD.82.112003. arXiv: 1010.4096 [astro-ph.HE] (cited on page 84).
- [181] M. G. Aartsen et al. “Search for Neutrinos from Dark Matter Self-Anihilations in the center of the Milky Way with 3 years of IceCube/DeepCore”. In: *Eur. Phys. J.* C77.9 (2017), page 627. DOI: 10.1140/epjc/s10052-017-5213-y. arXiv: 1705.08103 [hep-ex] (cited on page 85).
- [182] M. G. Aartsen et al. “Search for annihilating dark matter in the Sun with 3 years of IceCube data”. In: *Eur. Phys. J.* C77.3 (2017), page 146. DOI: 10.1140/epjc/s10052-017-4689-9. arXiv: 1612.05949 [astro-ph.HE] (cited on page 85).
- [183] R. Abbasi et al. “Limits on a muon flux from Kaluza-Klein dark matter annihilations in the Sun from the IceCube 22-string detector”. In: *Phys. Rev.* D81 (2010), page 057101. DOI: 10.1103/PhysRevD.81.057101. arXiv: 0910.4480 [astro-ph.CO] (cited on page 85).
- [184] M. G. Aartsen et al. “First search for dark matter annihilations in the Earth with the IceCube Detector”. In: *Eur. Phys. J.* C77.2 (2017), page 82. DOI: 10.1140/epjc/s10052-016-4582-y. arXiv: 1609.01492 [astro-ph.HE] (cited on pages 85, 144, 146).
- [185] “Quantised singularities in the electromagnetic field,” in: *Proceedings of the Royal Society of London A: Mathematical, Physical and Engineering Sciences* 133.821 (1931), pages 60–72. ISSN: 0950-1207. DOI: 10.1098/rspa.1931.0130. eprint: <http://rspa.royalsocietypublishing.org/content/133/821/60.full.pdf>. URL: <http://rspa.royalsocietypublishing.org/content/133/821/60> (cited on page 85).
- [186] G.’t Hooft. “Magnetic monopoles in unified gauge theories”. In: *Nuclear Physics B* 79.2 (1974), pages 276–284. ISSN: 0550-3213. DOI: [https://doi.org/10.1016/0550-3213\(74\)90486-6](https://doi.org/10.1016/0550-3213(74)90486-6). URL: <http://www.sciencedirect.com/science/article/pii/0550321374904866> (cited on page 86).
- [187] Alexander M. Polyakov. “Particle Spectrum in the Quantum Field Theory”. In: *JETP Lett.* 20 (1974). [,300(1974)], pages 194–195 (cited on page 86).
- [188] M. G. Aartsen et al. “Search for non-relativistic Magnetic Monopoles with IceCube”. In: *Eur. Phys. J.* C74.7 (2014), page 2938. DOI: 10.1140/epjc/s10052-014-2938-8. arXiv: 1402.3460 [astro-ph.CO] (cited on page 86).
- [189] D Schultz. “IceProd 2: A Next Generation Data Analysis Framework for the IceCube Neutrino Observatory”. In: *Journal of Physics: Conference Series* 664.6 (2015), page 062056. URL: <http://stacks.iop.org/1742-6596/664/i=6/a=062056> (cited on page 91).
- [190] D. Heck et al. “CORSIKA: A Monte Carlo code to simulate extensive air showers”. In: (1998) (cited on page 91).
- [191] Ralph Engel et al. “Towards the next generation of CORSIKA: A framework for the simulation of particle cascades in astroparticle physics”. In: (2018). arXiv: 1808.08226 [astro-ph.IM] (cited on page 91).
- [192] Sergey Ostapchenko. “Monte Carlo treatment of hadronic interactions in enhanced Pomeron scheme: I. QGSJET-II model”. In: *Phys. Rev.* D83 (2011), page 014018. DOI: 10.1103/PhysRevD.83.014018. arXiv: 1010.1869 [hep-ph] (cited on page 92).
- [193] Felix Riehn et al. “The hadronic interaction model SIBYLL 2.3c and Feynman scaling”. In: *PoS ICRC2017* (2018). [35,301(2017)], page 301. DOI: 10.22323/1.301.0301. arXiv: 1709.07227 [hep-ph] (cited on page 92).
- [194] T. Pierog et al. “EPOS LHC: Test of collective hadronization with data measured at the CERN Large Hadron Collider”. In: *Phys. Rev.* C92.3 (2015), page 034906. DOI: 10.1103/PhysRevC.92.034906. arXiv: 1306.0121 [hep-ph] (cited on page 92).
- [195] Sam De Ridder. “Sensitivity of IceCube Cosmic Ray measurements for the hadronic interaction models”. PhD thesis. UGent, 2019 (cited on pages 92, 93).

- [196] Giuseppe Battistoni et al. “Overview of the FLUKA code”. In: *Annals Nucl. Energy* 82 (2015), pages 10–18. DOI: 10.1016/j.anucene.2014.11.007 (cited on page 92).
- [197] K. Rawlins. “Cosmic ray spectrum and composition from three years of IceTop and IceCube”. In: *J. Phys. Conf. Ser.* 718.5 (2016), page 052033. DOI: 10.1088/1742-6596/718/5/052033 (cited on page 93).
- [198] Alessio Porcelli. “Measurements of the first two moments of the depth of shower maximum over nearly three decades of energy, combining data from”. In: *PoS ICRC2015* (2016), page 420. DOI: 10.22323/1.236.0420 (cited on page 93).
- [199] John Belz. “Summary of UHECR composition measurements by the Telescope Array Experiment”. In: *PoS ICRC2015* (2016), page 351. DOI: 10.22323/1.236.0351 (cited on page 93).
- [200] H. P. Dembinski et al. “Report on Tests and Measurements of Hadronic Interaction Properties with Air Showers”. In: 2019. arXiv: 1902.08124 [astro-ph.HE] (cited on page 93).
- [201] Askhat Gazizov and Marek P. Kowalski. “ANIS: High energy neutrino generator for neutrino telescopes”. In: *Comput. Phys. Commun.* 172 (2005), pages 203–213. DOI: 10.1016/j.cpc.2005.03.113. arXiv: astro-ph/0406439 [astro-ph] (cited on page 93).
- [202] M. G. Aartsen et al. “Observation of High-Energy Astrophysical Neutrinos in Three Years of IceCube Data”. In: *Phys. Rev. Lett.* 113 (2014), page 101101. DOI: 10.1103/PhysRevLett.113.101101. arXiv: 1405.5303 [astro-ph.HE] (cited on pages 93–95).
- [203] C. Andreopoulos et al. “The GENIE Neutrino Monte Carlo Generator”. In: *Nucl. Instrum. Meth.* A614 (2010), pages 87–104. DOI: 10.1016/j.nima.2009.12.009. arXiv: 0905.2517 [hep-ph] (cited on page 94).
- [204] Costas Andreopoulos et al. “The GENIE Neutrino Monte Carlo Generator: Physics and User Manual”. In: (2015). arXiv: 1510.05494 [hep-ph] (cited on page 94).
- [205] M. Honda et al. “Atmospheric neutrino flux calculation using the NRLMSISE-00 atmospheric model”. In: *Phys. Rev.* D92.2 (2015), page 023004. DOI: 10.1103/PhysRevD.92.023004. arXiv: 1502.03916 [astro-ph.HE] (cited on pages 94, 95).
- [206] Mario Dunsch et al. “Recent Improvements for the Lepton Propagator PROPOSAL”. In: (2018). arXiv: 1809.07740 [hep-ph] (cited on pages 96, 97).
- [207] Johan Lundberg et al. “Light tracking for glaciers and oceans: Scattering and absorption in heterogeneous media with Photonics”. In: *Nucl. Instrum. Meth.* A581 (2007), pages 619–631. DOI: 10.1016/j.nima.2007.07.143. arXiv: astro-ph/0702108 [ASTRO-PH] (cited on page 98).
- [208] K. J. Ma et al. “Time and Amplitude of Afterpulse Measured with a Large Size Photomultiplier Tube”. In: *Nucl. Instrum. Meth.* A629 (2011), pages 93–100. DOI: 10.1016/j.nima.2010.11.095. arXiv: 0911.5336 [physics.ins-det] (cited on page 98).
- [209] J. Ahrens et al. “Muon track reconstruction and data selection techniques in AMANDA”. In: *Nucl. Instrum. Meth.* A524 (2004), pages 169–194. DOI: 10.1016/j.nima.2004.01.065. arXiv: astro-ph/0407044 [astro-ph] (cited on pages 102–105).
- [210] M. G. Aartsen et al. “Improvement in Fast Particle Track Reconstruction with Robust Statistics”. In: *Nucl. Instrum. Meth.* A736 (2014), pages 143–149. DOI: 10.1016/j.nima.2013.10.074. arXiv: 1308.5501 [astro-ph.IM] (cited on page 103).
- [211] Till Neunhoffer. “Estimating the angular resolution of tracks in neutrino telescopes based on a likelihood analysis”. In: *Astropart. Phys.* 25 (2006), pages 220–225. DOI: 10.1016/j.astropartphys.2006.01.002. arXiv: astro-ph/0403367 [astro-ph] (cited on page 107).
- [212] The IceCube Collaboration. URL: https://internal-apps.icecube.wisc.edu/reports/data/icecube/2014/04/001/icecube_201404001_v1.pdf (cited on page 107).

- [213] M. G. Aartsen et al. “Energy Reconstruction Methods in the IceCube Neutrino Telescope”. In: *JINST* 9 (2014), P03009. DOI: 10.1088/1748-0221/9/03/P03009. arXiv: 1311.4767 [physics.ins-det] (cited on page 107).
- [214] D. Góra et al. *Studies on millipede, IceCube Internal Report: icecube/201404001*. (Cited on page 108).
- [215] Stef Verpoest. URL: https://lib.ugent.be/fulltxt/RUG01/002/479/620/RUG01-002479620_2018_0001_AC.pdf (cited on page 108).
- [216] URL: https://wiki.icecube.wisc.edu/index.php/SLC_hit_cleaning (cited on page 109).
- [217] URL: <https://www.dissertations.se/dissertation/fef1f8e4ba/> (cited on pages 110–112).
- [218] Hanchuan Peng, Fuhui Long, and C. Ding. “Feature selection based on mutual information criteria of max-dependency, max-relevance, and min-redundancy”. In: *IEEE Transactions on Pattern Analysis and Machine Intelligence* 27.8 (Aug. 2005), pages 1226–1238. ISSN: 0162-8828. DOI: 10.1109/TPAMI.2005.159 (cited on page 113).
- [219] Yoav Freund and Robert E Schapire. “A Decision-Theoretic Generalization of On-Line Learning and an Application to Boosting”. In: *Journal of Computer and System Sciences* 51.1 (1997), pages 119–139. ISSN: 0022-0000. DOI: <https://doi.org/10.1006/jcss.1997.1504>. URL: <http://www.sciencedirect.com/science/article/pii/S002200009791504X> (cited on page 115).
- [220] S. Fink C. Böser and S. Röcker. *Introduction to boosted decision trees: A multivariate approach to clasification problems*. Presented at the KSETA Doctoral Workshop, Berlin, Germany. July 2014 (cited on page 117).
- [221] The IceCube Collaboration. URL: <https://docushare.icecube.wisc.edu/dsweb/Get/Document-56551/VEFproposal.pdf> (cited on page 121).
- [222] The IceCube Collaboration. URL: https://docushare.icecube.wisc.edu/dsweb/Get/Document-59303/lowup_2012_proposal.pdf (cited on page 121).
- [223] The IceCube Collaboration. URL: https://docushare.icecube.wisc.edu/dsweb/Get/Document-59906/MuonFilter2012_v3_with_addendum.pdf (cited on page 121).
- [224] The IceCube Collaboration. URL: <https://docushare.icecube.wisc.edu/dsweb/Get/Document-59728/onlinel2proposal2012.pdf> (cited on page 121).
- [225] The IceCube Collaboration. URL: <https://docushare.icecube.wisc.edu/dsweb/Get/Document-59397/DeepCoreFilterProposal.pdf> (cited on page 123).
- [226] The IceCube Collaboration. URL: https://wiki.icecube.wisc.edu/index.php/Effects_of_DOM_Mainboard_Release_443 (cited on page 123).
- [227] Peter Nießen. “Search for relativistic magnetic monopoles with the AMANDA detector”. PhD thesis. Humboldt-Universität zu Berlin, Mathematisch-Naturwissenschaftliche Fakultät I, 2001. DOI: <http://dx.doi.org/10.18452/14579> (cited on page 130).
- [228] S. Verpoest. “Search for particles with fractional charges in IceCube based on anomalous energy loss”. Master’s thesis. UGent, 2018 (cited on page 134).
- [229] J. Künnen. “A Search for Dark Matter in the Center of the Earth with the IceCube Neutrino Detector”. Master’s thesis. VUB, 2015 (cited on page 138).
- [230] The IceCube Collaboration. URL: <http://software.icecube.wisc.edu/documentation/projects/pybdt/> (cited on page 141).
- [231] R. J. Britto, B. S. Acharya, and G. C. Anupama. “Data analysis method for the search of point sources of gamma rays with the HAGAR telescope array”. In: *Proceedings, 32nd International Cosmic Ray Conference (ICRC 2011): Beijing, China, August 11-18, 2011*. Volume 9, page 142. DOI: 10.7529/ICRC2011/V09/0943 (cited on page 144).

-
- [232] M. G. Aartsen et al. “Searches for Relativistic Magnetic Monopoles in IceCube”. In: *Eur. Phys. J.* C76.3 (2016), page 133. DOI: 10.1140/epjc/s10052-016-3953-8. arXiv: 1511.01350 [astro-ph.HE] (cited on pages 144, 146).
 - [233] F. Scheriau. “Data-Mining in der Astroteilchenphysik”. Master’s thesis. University of Dortmund, 2014 (cited on page 144).
 - [234] Gary J. Feldman and Robert D. Cousins. “A Unified approach to the classical statistical analysis of small signals”. In: *Phys. Rev.* D57 (1998), pages 3873–3889. DOI: 10.1103/PhysRevD.57.3873. arXiv: physics/9711021 [physics.data-an] (cited on page 146).
 - [235] Gary C. Hill and Katherine Rawlins. “Unbiased cut selection for optimal upper limits in neutrino detectors: The Model rejection potential technique”. In: *Astropart. Phys.* 19 (2003), pages 393–402. DOI: 10.1016/S0927-6505(02)00240-2. arXiv: astro-ph/0209350 [astro-ph] (cited on page 147).
 - [236] Thomas K. Gaisser. “Spectrum of cosmic-ray nucleons, kaon production, and the atmospheric muon charge ratio”. In: *Astropart. Phys.* 35 (2012), pages 801–806. DOI: 10.1016/j.astropartphys.2012.02.010. arXiv: 1111.6675 [astro-ph.HE] (cited on page 150).
 - [237] G. D. Barr et al. “Three-dimensional calculation of atmospheric neutrinos”. In: *Phys. Rev. D* 70 (2 July 2004), page 023006. DOI: 10.1103/PhysRevD.70.023006. URL: <https://link.aps.org/doi/10.1103/PhysRevD.70.023006> (cited on page 150).
 - [238] Joerg R. Hoerandel. “On the knee in the energy spectrum of cosmic rays”. In: *Astropart. Phys.* 19 (2003), pages 193–220. DOI: 10.1016/S0927-6505(02)00198-6. arXiv: astro-ph/0210453 [astro-ph] (cited on page 150).
 - [239] Aaron Roodman. “Blind analysis in particle physics”. In: *eConf* C030908 (2003). [,166(2003)], TUIT001. arXiv: physics/0312102 [physics.data-an] (cited on page 153).